Atomistic Calculations of Magnetic Properties of Rare-Earth Transition-Metal Permanent Magnets

Samuel Chaiyar Westmoreland

PhD

University of York

Physics

October 2018

Abstract

Rare-earth permanent magnets are becoming increasingly important with increasing emphasis placed on the replacement of fossil fuels in transportation and energy generation. Due to its large $(BH)_{\max}$, $Nd_2Fe_{14}B$ has been the permanent magnet material of choice for a wide range of applications since its discovery 40 years ago, including in electric motors and wind turbines. Its excellent magnetic properties come from a combination of high saturation magnetisation and high coercivity. In bulk $Nd_2Fe_{14}B$-sintered magnets however, the coercivity is $< 20\%$ of the theoretical Stoner-Wohlfarth limit. In the work presented in this thesis we investigate the possibility of coupling rare-earth permanent magnets with a magnetically soft phase to improve thermal stability and $(BH)_{\max}$ using a generic atomistic spin model. We then develop a fully parameterised atomistic spin model for $Nd_2Fe_{14}B$ and $NdFe_{12}$ parameterised from experimental and *ab initio* data. We use this model to explore more complex magnetic features and materials. The effects of grain boundary interfaces on the local anisotropy are investigated using a $Nd_2Fe_{14}B/\alpha$-Fe interface structure relaxed using molecular dynamics, and the spin dynamics at these interfaces calculated. These reveal Barkhausen-type jumps of domain walls propagating across the interface. Substitution of stabilising elements Ti and Zr into RFe_{12}-type materials and their effects on the inter-sublattice coupling are studied. In addition, the micromagnetic cell size and temperature scaling of the saturation magnetisation and anisotropy are calculated using the atomistic model in an effort to link the models across a multiscale approach to permanent magnet modelling.

Contents

List of Tables

List of Figures

Acknowledgements

I would like to thank my supervisors, Professor Roy Chantrell and Dr Richard Evans, for their continual support and guidance over the course of this PhD. I am also much indebted to my collaborators at the University of Exeter for their valuable collaboration and fruitful discussion. Finally I wish to express my immense gratitude to my family and friends for all of their patience and unwavering support over the last four years.

This work is based on results obtained from the future pioneering program "Development of magnetic material technology for high-efficiency motors" commissioned by the New Energy and Industrial Technology Development Organisation (NEDO).

Declaration

The author hereby declares that the work presented in this thesis is his own work, except for previously acknowledged contributions. This work has not previously been presented for an award at this, or any other, University. All sources are acknowledged as References.

The molecular dynamics calculations, namely in the work on grain boundary interfaces and Ti substitution, were carried out by Gino Hrkac and Connor Skelland at the University of Exeter, UK. The atomistic spin dynamics software package VAMPIRE is maintained and was chiefly implemented by my supervisor Dr Richard Evans. The calculations were performed by the author and are presented here.

Many of the results in this thesis have been presented at national and international conferences by the author, and the following publications have so far come out of this research:

- Westmoreland, S. C. et al. Multiscale model approaches to the design of advanced permanent magnets. Scr. Mater. 148, 56–62 (2018).
- Skelland, C. et al. Probability Distribution of Substituted Titanium in RT_{12} (R = Nd and Sm; T = Fe and Co) Structures. IEEE Trans. Magn. 54, 1–5 (2018).

Samuel Westmoreland

October 2018

In memory of Floyd.

Chapter 1

Introduction

The scientific study of magnetic materials has a long history dating back to William Gilbert's *De Magnete* published in 1600 [1]. Since then, our understanding of the properties of magnets has taken enormous strides. Oersted's observation in 1819 that a compass needle is deflected by a current-carrying wire revealed the fundamental connection between electricity and magnetism [2]. Almost one hundred years later, in 1907, Pierre Weiss took another giant step towards a modern theory of magnetism with his hypothesis that magnetic dipoles interact with one another via a 'molecular field' [3]. By 1927, we had arrived at a fully quantum mechanical explanation for ferromagnetism when, almost simultaneously, Dirac and Heisenberg proposed the so-called *exchange* interaction, an effect arising due to a combination of the Pauli exclusion principle and the physical overlap of electron wave functions [4].

Since then, significant headway has been made through experimental and theoretical studies of magnetic materials, granting the scientific community access to a host of new materials and technological breakthroughs. Some current active areas of research in the field include magnon spintronics [5–7], spin caloritronics [8–10], heat-assisted magnetic recording [11–13], the use of magnetic nanoparticles in bio-

medicine [14–16], as well as rare-earth permanent magnet materials [17–20], to name but a few.

1.1 Permanent magnets

A permanent magnet is named so because the origin of its magnetism comes from the intrinsic structure of the magnet itself. This is in contrast with an electromagnet, the magnetic properties of which come from coiling a current-carrying wire around a solenoid, generating a magnetic field. The progress of permanent magnets over the course of the last hundred years or so is best appraised by looking at how the value of the largest achievable maximum energy product ($(BH)_{\max}$) has grown, shown in Fig. 1.1. The $(BH)_{\max}$ value of a material is the usual criterion by which its utility is assessed, and indicates the maximum amount of energy which can be stored in the magnet. It is given by the maximum product between the magnetic induction B and applied field H, or in other words, the maximum square area that can be contained inside the second quadrant of a $B(H)$ hysteresis loop.

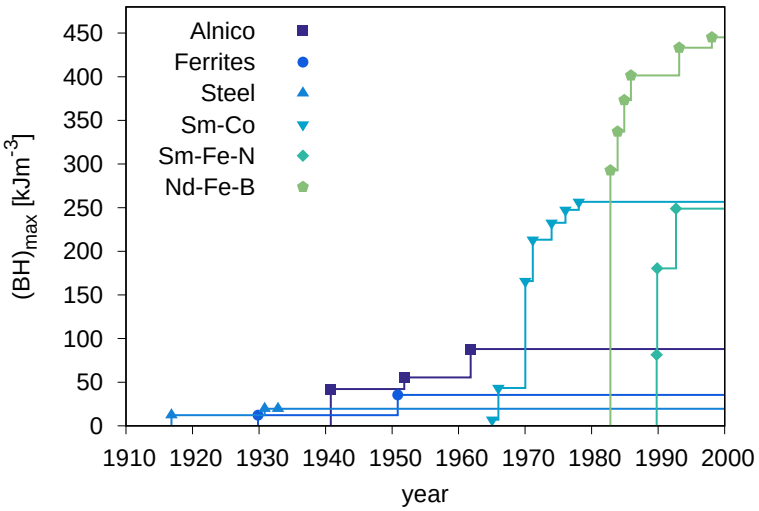

Figure 1.1: The evolution of the maximum achievable $(BH)_{\max}$ over the course of the 20th century, with each curve showing a different family of materials. Adapted from Ref. [21]

In the early part of the 20th century, cobalt steel based permanent magnets were replaced by the alnico class of materials (alloys formed of aluminium, nickel, and cobalt), pushing the limits of the day in terms of the $(BH)_{\max}$ that could be achieved. Over the years various new families of materials were discovered and synthesised, resulting in a series of jumps over time in the maximum achievable values of $(BH)_{\max}$. In the 1960s, Sm-Co magnets began to appear, the first of the rare-earth-transition-metal (R-TM) based permanent magnets. In this family of materials the rare-earth constituents provide the strong magnetocrystalline anisotropy (essential for large $(BH)_{\max}$), while the TM sublattice provides the majority of the magnetisation. This was an exciting time in the field of permanent magnets, however problems began to arise surrounding the availability of the requisite materials. Samarium is one of the least abundant rare-earth elements, while cobalt supplies were beset by the 1978 civil war which tore through what is now the Democratic Republic of Congo, where the majority of the world's cobalt supply was located [22]. The shortage of supply accelerated the on-going search for new permanent magnet materials, and in 1983 a new family of materials, the class of $R_2Fe_{14}B$ compounds, was announced at the 29th Magnetism and Magnetic Materials Conference in Pittsburgh [19, 20, 23–26].

With this new class of compounds, $(BH)_{\max}$ values were achieved that were far larger than any measured for any other material up until then. Sagawa et al. [23] measured a $(BH)_{\max}$ of $\sim$300 kJm^{-3}. Since this time, there has been considerable interest in the $R_2Fe_{14}B$ compounds, industrially of course, but also from the point of view of fundamental scientific inquiry. In the last fifteen years the maximum achieved $(BH)_{\max}$ in $Nd_2Fe_{14}B$ has increased to $\sim$450 kJm^{-3} [27]. Since their discovery $R_2Fe_{14}B$ magnets have revolutionised the design of motors, generators, and actuators [28]. Their enormous $(BH)_{\max}$ has allowed the downsizing of devices many times over.

Recently, interest in rare-earth based permanent magnets has been spurred anew as the potential consequences of human induced climate change have come to the fore. As we have become increasingly aware of the acute dangers of non-renewable energy sources to the environment, a greater emphasis has been placed on improving the transmission of electricity as well as replacing fossil fuel-based combustion engines with electric motors. There has also been a large increase in the global uptake of wind turbines, in which rare-earth permanent magnets play a key role, with global wind power capacity reportedly increasing 11% between 2016 and 2017 [29]. The development of functional magnetic materials has played and will continue to play a large part in this transition to cleaner generation and consumption of energy. In particular, the development of rare-earth intermetallic compounds is essential as there is a need for large energy densities at a range of operating temperatures across a range of devices [27].

One drawback of $Nd_2Fe_{14}B$ is that at the operating temperature of high-performance electric motors ($\sim$ 450 K) the coercivity drops off to an unacceptably low level. For this reason, currently electric motor manufacturers partially substitute the Nd with Dy, increasing the coercivity sufficiently for high temperature operation. The downside of this approach is that Dy is a particularly rare metal and can cost up to eight times as much as Nd. Thus there is an incentive to research and produce Dy-free compounds that are able to operate at the required temperatures.

There are a number of approaches to solving this problem that have emerged. One approach is that of exchange-coupled 'nanocomposite' magnets [30]. By combining soft, high-magnetisation phases with a hard, high-coercivity magnetic phase, the magnetic properties and energy density of the composite material can potentially be enhanced as a result of the exchange coupling between the phases [31]. The inclusion of a magnetically soft phase can have the added benefit of reducing the overall cost of the material for two reasons. The first, magnetically soft phases tend to be cheaper,

and second, by replacing a portion of the hard magnetic phase with the soft, the rare-earth content of the composite material can be reduced. Nanoscale particles were successfully produced via surfactant-assisted ball milling by Wang et al. [32] which could be aligned in a magnetic field to produce anisotropic bulk magnets. Rong et al. [33] demonstrated the formation of hard/soft nanocomposites using a process of severe plastic deformation and warm compaction to produce a $SmCo_5$/Fe(Co) bulk nanocomposite. For a $SmCo_5$ + 25 wt% $Fe_{65}Co_{35}$ nanocomposite it was measured that the maximum energy product increased to 152.8 kJm^{-3}, compared with 71.6 kJm^{-3} for the single-phase $SmCo_5$.

Another approach is to investigate and understand in detail the coercivity mechanisms at work in rare-earth transition-metal compounds. Investigations by Hrkac et al. [34] showed that the grain boundary phases and their distribution in the microstructure of $Nd_2Fe_{14}B$ are pivotal factors in determining the coercivity. Currently the coercive field only reaches 20–30% of the theoretical maximum (the anisotropy field). This is known as Brown's paradox [35]. It is theorised that the anisotropy at the grain boundaries is locally suppressed as a result of defects and roughness. If the effects of these can be properly understood, engineering of rare-earth permanent magnets at the nano-scale to fine-tune the properties may be a solution in the future.

A third approach is the discovery of new compounds that can eventually replace $Nd_2Fe_{14}B$. RFe_{12} compounds are one family of materials that are expected to have very high saturation magnetisation because the ratio of the transition-metal to rare-earth content is higher than in $R_2Fe_{14}B$. In general the RFe_{12} compounds are unstable as binary compounds, and require a third element M to stabilise the phase. The effects of the stabilising element are an ongoing area of research, however in general they are thought to be detrimental to the energy density as their presence comes at the cost of losing part of either the Fe or rare-earth sublattices, which both play vital roles in maximising the energy density as discussed already. Very recently however, Hirayama

et al. [36, 37] generated interest in this area by synthesising a $NdFe_{12}N_x$ crystal phase without the need for a third stabilising element. The nitrogen is inserted into the unit cell by nitriding in an N_2 gas atmosphere, and sits at interstitial sites within the unit cell. The magnetic properties were measured at room temperature as follows: saturation magnetisation $\mu_0 M_s \approx 1.66$ T, the anisotropy field $\mu_0 H_a \approx 8$ T and the Curie temperature $T_c \approx 823$ K. These initial measurements compare very favourably to $Nd_2Fe_{14}B$ which has $\mu_0 M_s \approx 1.6$ T, $\mu_0 H_a \approx 7.5$ T and $T_c = 585$ K. While research into this material is in its very early stages, the data are very promising and could lead to exciting developments in the field of rare-earth permanent magnets.

There are of course, a number of different approaches towards modelling magnetic systems. In the following, the main approaches will be introduced, along with their respective strengths and weaknesses.

1.2 Methods for modelling magnetic systems

The three primary categories of methods for simulating magnetic systems are micromagnetics, *ab initio* methods, and atomistic methods. The essential distinction between the three is the length and time scales that they are able to model. This is important as often the behaviour of a magnetic system varies significantly depending on the scale upon which the system is considered.

1.2.1 Ab initio methods

As indicated in the schematic in Fig. 1.2, *ab initio* methods are able to resolve systems on the scale of electrons (on the order of a few angstroms). These are fully quantum mechanical models. Common examples include the density functional theory (DFT) and linear muffin-tin orbital (LMTO) methods.

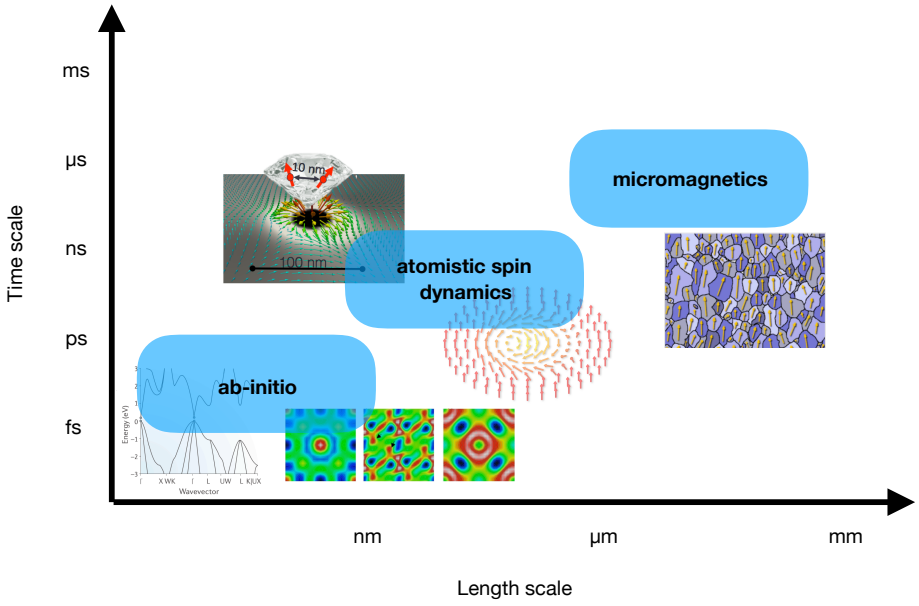

Figure 1.2: Approximate spatial and temporal scale regimes of the various methods for modelling magnetic systems.

In general the objective of an electronic structure method in this context is to determine the wave function and energy associated with a many-body system in a stationary state [38]. Solution of the Schrödinger equation for a given potential $v(\boldsymbol{r})$ (which is a system-dependent quantity) gives the many-body wave function $\Psi(\boldsymbol{r}_1, \boldsymbol{r}_2, \ldots, \boldsymbol{r}_n)$ of the system. From this, one is able to then calculate the expectation values of the observables of the system, e.g. of the eigenvalues or the particle density $n(\boldsymbol{r})$ [39]. The problem is that solution of the many-particle Schrödinger equation is intractable [40]. The idea behind DFT is to circumvent this problem by mapping the many-body problem, which has the potential operator $\hat{U} = \sum_{i<j} U(\boldsymbol{r}_i, \boldsymbol{r}_j)$, onto a single-body problem, which does not require $\hat{U}$. Rather than beginning from the system potential $v(\boldsymbol{r})$, the ground-state particle density $n_0(\boldsymbol{r})$ is used as a starting point, from which it is possible, in theory, to determine the associated ground-state wave function $\Psi_0(\boldsymbol{r}_1, \boldsymbol{r}_2, \ldots, \boldsymbol{r}_n)$. The idea, then, is that if Ψ_0 can be calculated from $n_0(\boldsymbol{r})$ and vice versa, then both must contain the same information. Thus all ground-

state observables are functionals of n_0 as well as Ψ_0, and the problem is reduced from depending on N variables, $\boldsymbol{r}_1, \boldsymbol{r}_2, \ldots, \boldsymbol{r}_n$, to depending only on one variable, $\boldsymbol{r}$ [39]. This is known as the Hohenberg-Kohn theorem [41].

These methods are advantageous in that they provide a way of understanding magnetic phenomena from first principles, and are formally exact [39]. In practice, approximations must be used (e.g. for the particle density functions) if simulating systems containing more than a few atoms, with the accuracy of the model dependent on the quality of the assumption. Nevertheless, modern *ab initio* methods are remarkably accurate and show a high degree of consistency across different implementations, as was demonstrated by Lejaeghere et al. [40]. The primary impediment to the use of *ab initio* methods for modelling of magnetic materials is their prohibitively large computational cost. This is large for equilibrium calculations, and larger still for simulations involving spin dynamics. Models of spin dynamics from first principles, which have only in recent years become viable, are able to simulate systems only on the order of 10 atoms [42–44].

DFT is a useful method of calculating magnetic parameters for input into larger scale spin dynamics simulations, particularly magnetocrystalline anisotropy values, but is a difficult and specialised area [45]. Presently it is limited in its ability to accurately model localised $4f$ electron states. The two most common electron density approximations: the local density approximation (LDA) and the generalised gradient approximation (GGA) are insufficient to describe the $4f$ electrons, as the energy levels that come out of these are too shallow and the wave functions too extended, a result of the self-interactions in LDA and GGA. Consequently the hybridisation between the f states and other states is too strong, skewing the total energy calculations [46]. This inability to accurately describe the $4f$ electrons can be considered a missing link in the multiscale pathway of modelling rare-earth permanent magnets [45].

1.2.2 Micromagnetics

At the larger end of the scale sits the micromagnetics method, first pioneered by Brown in 1963 [47]. It is categorised as a continuum method because the considered length scales are sufficiently large that the atomic structure of the crystal may be ignored, and it is assumed that due to the exchange interaction, the atomic spins contained within some finite volume are collinear [48]. The desired output of a micromagnetics model is the spatial (and temporal in the case of dynamic micromagnetics) dependence of the magnetisation, which is found via minimisation of the Gibb's free energy with respect to the magnetisation, where the important contributions to the energy are the exchange, magnetostatic and anisotropy energies [49, 50].

The use of the micromagnetics method is particularly suited to system sizes of the order of the magnetic domain size of the system and above, and in particular for coarse calculations of magnetisation reversal and hysteresis effects. For example, micromagnetics calculations have been used to show the potential advantages of complex designs such as the 'Battenburg' structure, where a number of different magnetic phases were coupled together to achieve a maximum energy product exceeding 400 kJm^{-3} while simultaneously reducing rare-earth content [51]. However the models lack access to the effects of the detailed interface structure at the atomic level and, importantly, their effects on the macroscopic magnetic properties. Another drawback is that temperature effects must be treated in a somewhat artificial manner, via temperature scaling of the saturation polarisation, exchange constants and magnetocrystalline anisotropy constants. Moreover, at temperatures approaching the Curie temperature, the assumption of collinear alignment begins to breakdown due to atomic scale spin disorder [52]. A further difficulty is the scaling of magnetic properties with cell size, first investigated by Dobrovitski et al. [53] and Grinstein and Koch [54]. The coarse-graining of the micromagnetic variables tend to lead to

an overestimation of the Curie temperature, which is shown to be removed by a re-normalisation approach [54].

1.2.3 Atomistic spin dynamics

Finally, we arrive at the method of atomistic spin dynamics, which is the method used throughout this thesis. In terms of length scale, the atomistic method serves as a useful bridge between the micromagnetics formalism and *ab initio* simulation. The atomistic model is based on the physical assumption that the electrons in the unfilled shell of an atom are all localised to the atomic site, and thus a magnetic moment can be associated with that site whose magnitude is proportional to the vector sum of the the orbital and spin angular momenta of the unpaired electrons [55].

This is certainly true in the case of an isolated atom; the assumption made in the atomistic spin model is that the magnetic properties in condensed matter can be treated as a perturbation of the magnetic properties of the individual atoms. This turns out to be a very good assumption in the 4f series, as the 4f electrons interact weakly with one another and thus can be considered highly localised [55]. Whether or not the same assumption holds for 3d metals was for much of the 20th century a topic for debate. The question was whether the d electrons, from where the magnetic properties stem in the transition metals, are localised to the ionic sites, or itinerant, moving from atom to atom around the crystal [56]. It is now accepted that d electrons in transition metals are strongly interacting itinerant electrons, however band-structure calculations of the spin density in Fe-Co alloys by Schwarz et al. [57] showed that despite this, the spin density is strongly localised to the atomic sites [48]. This suggests that the bonding electrons have only a small net spin, and the remaining d electrons form an effective localised moment around the nucleus [48].

At a basic level, simple spin models are an extension of finite difference micromagnetics to atomic scale resolution [52]. While these are useful for describing atomic

scale magnetism and thermal effects, no particular insight is gained into the complex effects of the interplay between the crystal structure, electronic properties, and magnetism [52]. To create a more compelling model of the magnetic behaviour of a specific material, inclusion of the exact crystal structure and a realistic picture of the magnetic interactions is required, which has only been a possibility in the last 20 years or so [52]. Some examples of such models can be found in Refs. [58–60]. The work presented in chapters 5, 6, and 7 are examples of the atomistic spin model being applied together with a full treatment of the atomic crystal structure.

In section 1.1, three approaches to finding more efficient permanent magnets were outlined. In each of the three approaches it is clear that atomic scale effects are at work and play an important role in the determination of the macroscale magnetic properties. Therefore in this thesis, each one will be investigated using an atomistic spin dynamics model. In chapter 2, the theoretical background of the model will be discussed in detail. Chapter 3 will outline the implementation of the model in the VAMPIRE software package [48], as well discuss the cell size dependence of some important parameters and the method used to determine this dependence. In chapter 4, the magnetic properties of α-Fe/$Nd_2Fe_{14}B$ core/shell nanoparticles will be investigated using a generic spin model. In chapter 5, the procedure for parameterising the full atomistic spin model for $Nd_2Fe_{14}B$ and $NdFe_{12}$ will be discussed. Chapter 6 contains an investigation into the reversal mechanisms of a system containing a grain boundary interface between $Nd_2Fe_{14}B$ and α-Fe phases to determine the role played by the interface. Finally, the effects of substituting Ti and Zr into the RFe_{12} phase will be explored in chapter 7.

The aim of the work in this thesis is to develop a working and fully parameterised atomistic spin model of rare-earth transition-metal compounds, in particular $Nd_2Fe_{14}B$ and $NdFe_{12}$, and then apply this model to a diverse array of magnetic structures to investigate the approaches discussed above for finding more efficient

materials, and to ascertain which of the approaches, if any, show potential as ways to make progress in the on-going pursuit of ever more powerful and efficient permanent magnets.

Chapter 2

Theoretical background

2.1 Atomistic spin dynamics model

In recent years, atomistic modelling of magnetic materials has emerged as an essential tool in trying to understand the underlying physical processes that drive the complicated behaviour observed in magnetic materials. All modern atomistic methods are based on the founding principles of Ernst Ising, which date back to 1925 [61]. The so-called Ising model was the first statistics-based theoretical model of ferromagnetism. In the model, atoms are treated as discrete variables which are represented by a vector, where physically the vector represents a magnetic dipole moment of atomic spin associated with the atom. Each atom assigned vector is allowed to be in either a spin-up $(+1)$ state or a spin-down (-1) state. Still today the Ising model is a very useful tool which continues to be used for computationally non-intensive simulations of simplistic materials. Whilst the method shows remarkable success in the determination of phase transitions in very simple magnetic systems, it is limited in its capability to describe more complex magnetic materials.

The Ising model was later improved upon in the form of the classical 3D Heisenberg spin model, in which each atomic spin vector is treated as a classical unit vector such

that

$$|\vec{s}_i| = 1 \tag{2.1}$$

and each spin is allowed to point in any direction in space [62]. This kind of treatment, despite neglecting quantum mechanical effects in its usual form, allows accurate calculation of phase transitions, surface effects and finite size effects in simple systems. Not until relatively recently however, have atomistic models become sufficiently detailed and computers sufficiently powerful to model complicated magnetisation dynamics at finite temperatures [63, 64].

As a result of this, the use of atomistic methods in the modelling of magnetic materials and devices has been slowly gaining traction, where traditionally the method of micromagnetics had taken precedence. The majority of recent advances in computational magnetism have come in the form of improved computational and mathematical techniques, as opposed to improvements in the underlying physics [64]. Perhaps the most important improvement made to these computational models has been the introduction of thermal activation. The micromagnetics formalism is intrinsically athermal, and thus magnetisation reversal processes take place at 0 K, although this can be rectified via parameterisation using finite temperature parameters (discussed in chapter 5). Drawing on the work of Brown [47], the technique used is to treat the thermal perturbations upon the spin system by a random field, following the methods put forward by Langevin [65].

The context of the atomistic spin model is depicted schematically in Fig. 2.1. The arrows indicate the interactions between the various computational and analytical techniques, as well as the informational pathways between the models. Here, $M_s(T, L)$, $K(T, L)$, and $A(T, L)$ denote the saturation magnetisation, the magnetocrystalline anisotropy constant, and the exchange stiffness respectively, each of which are functions of temperature T, and cell size L (for instances where they are passed to a micromagnetics model).

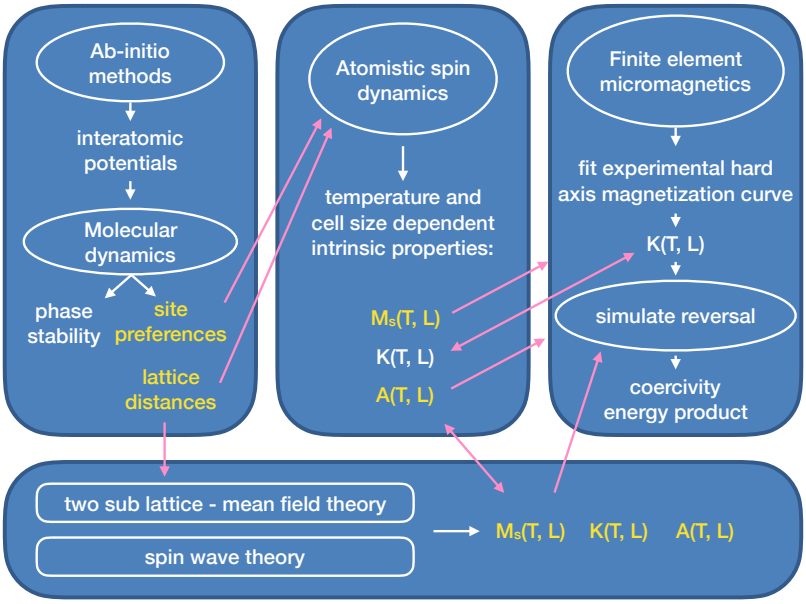

Figure 2.1: Schematic of the multiscale process for magnetic materials. The arrows indicate the interactions between the various computational and analytical methods and show the paths taken for the exchange of information between the model length-scales.

In a fully multiscale and self-consistent approach, the atomistic model would be purely parameterised by first principles calculations, and the micromagnetic approach would be parameterised fully by atomistic and first principles calculations, theoretically allowing modelling across many orders of magnitudes of space and time. In this picture, the atomistic model serves a useful function as providing input into larger scale simulations, however it is important to note that atomistic approaches are important in their own right, essentially merging the quantum mechanical and thermodynamic regimes, leading to important insights into thermally activated magnetic behaviour.

In the next section the fundamental principles and mechanics of the atomistic spin model will be discussed in a general way. The specifics of the implementation will be presented in chapter 3, while the specifics of the parameterisation of rare-earth intermetallic compounds will be discussed in chapter 5.

2.1.1 Atomistic spin magnetic moments

The atomistic spin model is principally a canonical ensemble of classical spin vectors coupled to one another via the Heisenberg exchange interaction. Each vector represents an atomic magnetic dipole moment. Numerically solving the equation of motion for each vector in an effective field allows the solution of finite temperature statistical systems.

The total dipole moment associated with a classical atomic spin vector is fundamentally a result of two phenomena: the intrinsic spin associated with each electron, and the orbital motion of the electrons about the nucleus. Each of these can be thought of as 'charges in motion', which induce a magnetic moment. The total magnetic moment of the atom is then a result of these two moments. The intrinsic spin of each electron contributes a magnetic dipole moment

$$\boldsymbol{m}_{\text{spin}} = g\mu_B[s(s+1)]^{1/2} \tag{2.2}$$

where $\mu_B = e\hbar/2m_e = 9.274 \times 10^{-24}$ JT^{-1} denotes the Bohr magneton, and s is the spin quantum number; and the orbital motion of the electrons about the nucleus contribute a total moment

$$\boldsymbol{m}_{\text{orbital}} = \mu_B[l(l+1)]^{1/2} \tag{2.3}$$

where g is the free electron g-value and l the orbital quantum number. The orbital and spin moments are coupled and can thus be summed in a specific way. Summing the individual electron spin quantum numbers to give a total spin quantum number S, and doing the same with the individual orbital spin quantum numbers l, gives many-electron quantum numbers L and S, which are in turn combined to give the total angular momentum quantum number J. J is then used to determine the magnetic

moment of the atom via the expression

$$\boldsymbol{m}_{\text{atom}} = g_J \mu_B [J(J+1)]^{1/2} \tag{2.4}$$

where g_J is the Landé g factor, which is a function of J, L, and S [66]. In many bulk magnetic materials the larger contribution to the magnetic moment comes from the spin moment of the electrons, as strong delocalisation of the electrons (as in metals) and strong crystal field splitting as a result of electrostatic interactions with the surrounding lattice result in a breaking of the symmetry and quenching of the orbital moment [67].

In the atomistic model the atomic magnetic moments are coupled to the lattice such that each spin has a magnetic moment μ_i and a fixed position $\boldsymbol{r}_i$.

2.1.2 The exchange interaction

The exchange interaction is the strongest of the energetic contributions to the classical spin Hamiltonian and gives rise to spontaneous magnetic ordering in magnetic materials, even in the absence of an externally applied magnetic field. The exchange energy was discovered simultaneously and independently by Dirac and Heisenberg in 1926 [68]. The description of the quantum mechanical origin of the exchange interaction is standard, and here we will follow the explanations of Morrish [69] and Blundell [70]. The description presented in this section serves purely as an illustration of the mechanism, and is not the method of solution in the atomistic spin dynamics model, in the case of which there are far too many interactions to solve for in this manner. Indeed, the necessary calculation would require unfathomable computing and memory resources. Rather, exact solution of this form is the domain of *ab initio* theorists.

We begin by considering a system of two electrons with spatial coordinates $\boldsymbol{r}_1$ and $\boldsymbol{r}_2$. The total wave function of the two electron system $\Psi(\boldsymbol{r}_1, \boldsymbol{r}_2)$ will be some linear combination of the individual electron wave functions $\psi(\boldsymbol{r}_1)$ and $\psi(\boldsymbol{r}_2)$ and must be a solution of the Schrödinger equation:

$$\Big[-\frac{\hbar^2}{2m}\nabla_1^2 - \frac{\hbar^2}{2m}\nabla_2^2 + V(\boldsymbol{r}_1) + V(\boldsymbol{r}_2)\Big]\Psi = E\Psi \tag{2.5}$$

where the subscripts 1 and 2 correspond to the two electrons. It can be seen by substitution that possible solutions are

$$\psi_{\mathrm{a}}(\boldsymbol{r}_1)\psi_{\mathrm{b}}(\boldsymbol{r}_2) \quad \text{and} \quad \psi_{\mathrm{a}}(\boldsymbol{r}_2)\psi_{\mathrm{b}}(\boldsymbol{r}_1)\ , \tag{2.6}$$

where $\psi_{\mathrm{a}}(\boldsymbol{r}_1)$ denotes the wave function of electron 1 located on atom a and $\psi_{\mathrm{b}}(\boldsymbol{r}_2)$ the wave function of electron 2 located on atom b and so on. In both examples in (2.6), $E = E_a + E_b$. However, because electrons are indistinguishable, there is the requirement that

$$|\Psi(\boldsymbol{r}_1, \boldsymbol{r}_2)|^2 d\boldsymbol{r}_1 d\boldsymbol{r}_2 = |\Psi(\boldsymbol{r}_2, \boldsymbol{r}_1)|^2 d\boldsymbol{r}_1 d\boldsymbol{r}_2\,. \tag{2.7}$$

That is to say, under interchanging of the electrons, the observable properties of the system should not change. Hence, it is required of the two electron wave function that either

$$\Psi(\boldsymbol{r}_1, \boldsymbol{r}_2) = \Psi(\boldsymbol{r}_2, \boldsymbol{r}_1) \tag{2.8}$$

or

$$\Psi(\boldsymbol{r}_1, \boldsymbol{r}_2) = -\Psi(\boldsymbol{r}_2, \boldsymbol{r}_1)\,. \tag{2.9}$$

These are the properties of symmetry (in the case of (2.8)) and antisymmetry (in the case of (2.9)). Neither wave function in (2.6) has either of these properties and so

both are unacceptable. However, the linear combinations

$$\begin{aligned}\Psi_{\text{sym}}(\boldsymbol{r}_1, \boldsymbol{r}_2) &= \frac{1}{\sqrt{2}}[\psi_a(\boldsymbol{r}_1)\psi_b(\boldsymbol{r}_2) + \psi_a(\boldsymbol{r}_2)\psi_b(\boldsymbol{r}_1)] \\ \Psi_{\text{anti}}(\boldsymbol{r}_1, \boldsymbol{r}_2) &= \frac{1}{\sqrt{2}}[\psi_a(\boldsymbol{r}_1)\psi_b(\boldsymbol{r}_2) - \psi_a(\boldsymbol{r}_2)\psi_b(\boldsymbol{r}_1)]\end{aligned} \tag{2.10}$$

do satisfy (2.8) and (2.9) and happen to be the *only* wave functions that do. The factors $1/\sqrt{2}$ are normalising factors, if the single electron wave functions are assumed already normalised. For electrons, there is a further requirement that the electrons remain distinct, as the Pauli exclusion principle prohibits two electrons from being found in an identical state; that is, having the same set of quantum numbers. This requires, then, that the total wave function be antisymmetric, eliminating the symmetric wave function in (2.10) as a possibility.

Given the antisymmetric two electron wave function from (2.10), in the Heitler-London approximation [71] the system energy is given by evaluating the integral

$$E = \iint \Psi^*(\boldsymbol{r}_1, \boldsymbol{r}_2)\langle H\rangle\Psi(\boldsymbol{r}_1, \boldsymbol{r}_2)d\boldsymbol{r}_1 d\boldsymbol{r}_2 \tag{2.11}$$

where the Hamiltonian $\langle H\rangle$ contains the individual electron Hamiltonians $\langle H_1\rangle$ and $\langle H_2\rangle$ as well as a third, interaction Hamiltonian $\langle H_{1,2}\rangle$. Thus the total energy of the system is given by

$$E_{\text{tot}} = \iint \Psi^*(\boldsymbol{r}_1, \boldsymbol{r}_2)\langle H_1 + H_2 + H_{1,2}\rangle\Psi(\boldsymbol{r}_1, \boldsymbol{r}_2)d\boldsymbol{r}_1 d\boldsymbol{r}_2\,. \tag{2.12}$$

Evaluating the integral, one finds that the operator H_1 gives rise to energy terms dependent only on electron a on atom 1, and the operator H_2 gives rise to energy terms dependent only on electron b on atom 2. The $H_{1,2}$ operator gives rise to the

interaction energy term

$$E_{1,2} = \iint \Psi^*(\boldsymbol{r}_1, \boldsymbol{r}_2)\langle H_{1,2}\rangle \Psi(\boldsymbol{r}_1, \boldsymbol{r}_2) d\boldsymbol{r}_1 d\boldsymbol{r}_2 = E_{\text{int}} \iint \Psi^*(\boldsymbol{r}_1, \boldsymbol{r}_2)\Psi(\boldsymbol{r}_1, \boldsymbol{r}_2) d\boldsymbol{r}_1 d\boldsymbol{r}_2 \tag{2.13}$$

which has two components: a Coulomb interaction term between the electrons on their respective atoms, and an 'exchange' energy that arises solely as a result of exchanging of the electrons. These are expressed as

$$\begin{aligned} E_{\text{coulomb}} &= \iint \left\{\psi_a^*(\boldsymbol{r}_1)\psi_b^*(\boldsymbol{r}_2)\right\} \langle H_{1,2}\rangle \left\{\psi_a(\boldsymbol{r}_1)\psi_b(\boldsymbol{r}_2)\right\} d\boldsymbol{r}_1 d\boldsymbol{r}_2 \\ E_{\text{exchange}} &= \iint \left\{\psi_a^*(\boldsymbol{r}_1)\psi_b^*(\boldsymbol{r}_2)\right\} \langle H_{1,2}\rangle \left\{\psi_a(\boldsymbol{r}_2)\psi_b(\boldsymbol{r}_1)\right\} d\boldsymbol{r}_1 d\boldsymbol{r}_2 \,. \end{aligned} \tag{2.14}$$

The exchange component is a purely quantum mechanical phenomenon because in the classical picture, interchanging of the electrons gives no difference in energy.

Now we have that

$$E_{\text{tot}} = E_1 + E_2 + E_{1,2} \,, \tag{2.15}$$

where the first two terms on the right-hand side represent the energy of the two electrons on their respective atoms, in the absence of any interaction; and a third term, which is the sum of the Coulomb and exchange interactions, both of which result from the interaction between the electrons. The above treatment demonstrates the existence of the exchange energy, but so far the spin quantum numbers of the electrons have been ignored. Now it must be shown that the correlation of the electron spins arises from this exchange interaction.

Let the spin part of the total wave function be denoted by χ_{S} for the antisymmetric singlet state and χ_{T} for the symmetric triplet state. The total wave function of the system, including both the spatial and spin parts, is then given by

$$\Psi_{\text{tot}} = \Psi(\boldsymbol{r}_1, \boldsymbol{r}_2)\chi(s_1, s_2) \,. \tag{2.16}$$

As already discussed, the total wave function must be antisymmetric under interchange of the electrons in accordance with the Pauli exclusion principle. Thus, if the spin part of the total two electron wave function is symmetric, the spatial part must be antisymmetric, and vice versa, in order to keep the total wave function $\Psi_{\rm tot}$ antisymmetric. Thus there are two possibilities for the total wave function:

$$\begin{aligned}\Psi_{\rm S} &= \frac{1}{\sqrt{2}}[\phi_a(\boldsymbol{r}_1)\phi_b(\boldsymbol{r}_2) + \phi_a(\boldsymbol{r}_2)\phi_b(\boldsymbol{r}_1)]\chi_{\rm S} \\ \Psi_{\rm T} &= \frac{1}{\sqrt{2}}[\phi_a(\boldsymbol{r}_1)\phi_b(\boldsymbol{r}_2) - \phi_a(\boldsymbol{r}_2)\phi_b(\boldsymbol{r}_1)]\chi_{\rm T}\ .\end{aligned} \tag{2.17}$$

The energies of these states are given by

$$\begin{aligned}E_{\rm S} &= \int \Psi_{\rm S}^*\langle H\rangle\Psi_{\rm S} d\boldsymbol{r}_1 d\boldsymbol{r}_2 \\ E_{\rm T} &= \int \Psi_{\rm T}^*\langle H\rangle\Psi_{\rm T} d\boldsymbol{r}_1 d\boldsymbol{r}_2\ .\end{aligned} \tag{2.18}$$

Taking the difference between the two gives

$$E_{\rm S} - E_{\rm T} = 2\int \phi_a^*(\boldsymbol{r}_1)\phi_b^*(\boldsymbol{r}_2)\langle H\rangle\phi_a(\boldsymbol{r}_2)\phi_b(\boldsymbol{r}_1) d\boldsymbol{r}_1 d\boldsymbol{r}_2\ . \tag{2.19}$$

For the singlet case, $\boldsymbol{S}_1 \cdot \boldsymbol{S}_2 = -\frac{3}{4}$, whereas for the triplet case, $\boldsymbol{S}_1 \cdot \boldsymbol{S}_2 = \frac{1}{4}$. Hence, the effective Hamiltonian can be written

$$\langle H\rangle = \frac{1}{4}(E_{\rm S} + 3E_{\rm T}) - (E_{\rm S} - E_{\rm T})\boldsymbol{S}_1 \cdot \boldsymbol{S}_2\,, \tag{2.20}$$

which is the sum between a constant term, and a term which depends on the electron spins. Absorbing the constant term into other constants, we are left with the so-called *exchange integral*, which can be expressed as:

$$J = \frac{E_{\rm S} - E_{\rm T}}{2} = \int \phi_a^*(\boldsymbol{r}_1)\phi_b^*(\boldsymbol{r}_2)\langle H\rangle\phi_a(\boldsymbol{r}_2)\phi_b(\boldsymbol{r}_1) d\boldsymbol{r}_1 d\boldsymbol{r}_2\,. \tag{2.21}$$

Thus the term in the effective Hamiltonian which depends on the spins can be rewritten as

$$\langle H \rangle^{\text{spin}} = -2J\boldsymbol{S}_1 \cdot \boldsymbol{S}_2 \,. \tag{2.22}$$

The sign of the exchange constant J is significant, with $J > 0$ corresponding to parallel spin alignment and $J < 0$ to antiparallel alignment (depicted schematically in Figure. 2.2). In a solid, the exchange energy should be summed over all electrons, such that

$$\langle H \rangle^{\text{spin}} = -2 \sum \sum J_{ij} \boldsymbol{s}_i \cdot \boldsymbol{s}_j \,, \tag{2.23}$$

though often it is sufficient to sum over only nearest-neighbour contributions to the exchange integral.

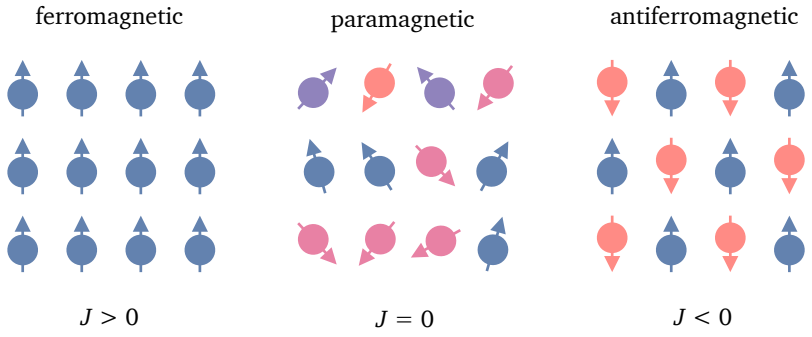

Figure 2.2: The effect of the exchange parameter on the magnetic ordering of the system. In general, positive, zero, and negative J will result in ferromagnetic, paramagnetic, and antiferromagnetic states respectively.

In general it is sufficient to assume that the exchange interaction is isotropic between a spin $\boldsymbol{S}_i$ and its neighbours, meaning that the exchange energy between two spins depends only on their respective orientations. However the Heisenberg form of the exchange is easily generalisable to cases where this is not so. In such materials

the exchange interaction forms a tensor with components

$$\boldsymbol{J}_{ij} = \begin{bmatrix} J_{xx} & J_{xy} & J_{xz} \\ J_{yx} & J_{yy} & J_{yz} \\ J_{zx} & J_{zy} & J_{zz} \end{bmatrix} \tag{2.24}$$

enabling a description of anisotropic exchange interactions such as two-ion anisotropy [58] and the Dzyaloshinskii-Moriya interaction, with off-diagonal components of the exchange tensor. In the case of tensorial exchange, the exchange energy is found by the tensor product between two spins:

$$\hat{\mathcal{H}} = -\sum_{ij} \boldsymbol{S}_i \boldsymbol{J}_{ij} \boldsymbol{S}_j. \tag{2.25}$$

An inherent strength of the atomistic model over its micromagnetic counterpart lies in its treatment of the exchange interaction. Using the Heisenberg form of the exchange, discretised at the atomic length scale, it is possible to simulate directly how the spin correlation varies atomistically, leading to more natural description of interesting macroscopic phenomena such as magnetic phase transitions.

2.1.3 Magnetocrystalline anisotropy

The magnetocrytalline anisotropy is an effect of the coupling of the magnetic moment to the crystal lattice via the electrostatic spin-orbit coupling. If more energy is required to magnetise a material or spin in one crystallographic direction than in another it is said to be anisotropic. The direction in which the magnetic crystal energy is lowest is commonly referred to as the easy axis, while the direction in which the energy of the crystal is highest is called the hard axis, and because the energy of the crystal depends on the spin orientation in this way, one can refer to the anisotropy as the magnetocrystalline anisotropy energy [72]. For BCC Fe, the energy required

to force the magnetisation away from the easy axis $\langle 001 \rangle$ onto the hard axis $\langle 111 \rangle$ is 0.05 MJm^{-3}. The equivalent energy in $\mathrm{Nd_2Fe_{14}B}$ on the other hand, is 4.9 MJm^{-3}. While these energies are small in comparison to, for example, exchange energies or cohesive energies, they are extremely important in the assessment of the utility and performance of a magnetic material in numerous applications. Hard magnets, among which rare-earth based permanent magnets are categorised, are characterised by large anisotropy energies, making them ideal for applications such as generators and electric motors.

The angular dependence of the magnetocrystalline anisotropy energy in uniaxial materials is formally described by

$$E_{\mathrm{MAE}} = K_1 \sin^2 \theta + K_2 \sin^4 \theta + \dots . \tag{2.26}$$

θ here denotes the angle between the magnetisation vector and the easy axis, and K_1 and K_2 are second and fourth order uniaxial anisotropy constants. In the atomistic spin model the uniaxial contribution of the magnetocrystalline anisotropy energy to the spin Hamiltonian is given by

$$\mathcal{H}_{\mathrm{anis}} = -\sum_i k_u (\boldsymbol{S}_i \cdot \hat{\boldsymbol{e}}_u)^2 \tag{2.27}$$

where k_u is the atomistic uniaxial anisotropy constant, and $\hat{\boldsymbol{e}}_u$ is a unit vector pointing in the direction of the easy axis. In the usual nomenclature, $k_u > 0$ denotes an easy axis orientation out of the plane, normally along the $\langle 001 \rangle$ direction, while $k_u < 0$ denotes an easy-plane anisotropy where the spin prefers to lie in the xy plane. In the case of positive anisotropy constant K_u, the magnetocrystalline anisotropy energy can be thought of as an energy barrier between parallel alignment with the easy axis and anti-parallel alignment, where the energy barrier has height $K_u V$, where V is

the volume of the system under consideration. This is illustrated schematically in Fig. 2.3.

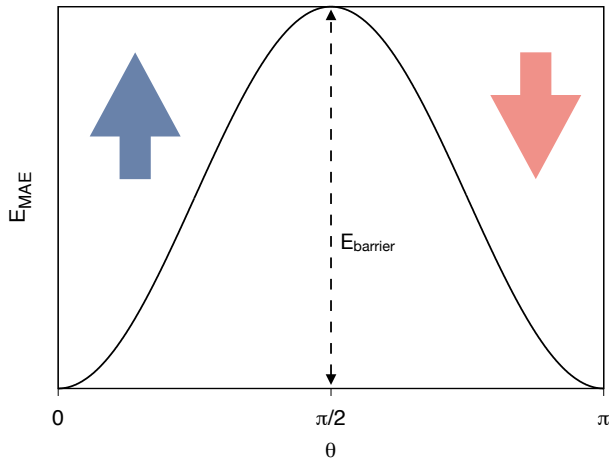

Figure 2.3: Schematic showing the magnetocrystalline anisotropy energy as a function of the angle between the spin vector and the easy axis in a uniaxial system. The height of the energy barrier gives the energy required to switch the spin from parallel alignment with the easy axis to anti-parallel alignment.

2.1.4 Zeeman interaction

We must also include in the spin Hamiltonian an interaction between the magnetic system and an externally applied magnetic field, called the Zeeman interaction. The system couples to the magnetic field such that the contribution to the Hamiltonian is described by

$$\mathcal{H}_{Zeeman} = -\mu_s \sum_i \boldsymbol{S}_i \cdot \boldsymbol{H}_{\text{app}} \tag{2.28}$$

where μ_s is the spin magnetic moment, $\boldsymbol{S}_i$ is the spin vector on site i and H_{app} applied field vector. This will give a minimum energy when the spin is aligned with the applied field. The strength of the coupling is proportional to the magnitude of the magnetic moment μ_s, thus at finite temperatures, the implementation of which is discussed in

section 2.1.6, when the magnetisation is reduced, coupling to the external field will be weakened.

2.1.5 The spin Hamiltonian

We look now at the classical spin model Hamiltonian, which approximates the energetics of a system of interacting spins including exchange, anisotropy and Zeeman contributions. By encapsulating the essential physics of a magnetic system the spin Hamiltonian enables us to model magnetic systems at the atomic level. The total system Hamiltonian is a summation of these energy contributions, integrating over all spins $\boldsymbol{S}_i$. The Hamiltonian thus takes the form

$$\mathcal{H} = \mathcal{H}_{\text{exch}} + \mathcal{H}_{\text{anis}} + \mathcal{H}_{\text{Zeeman}} \tag{2.29}$$

where the terms on the right hand side denote the exchange, anisotropy, and Zeeman energies respectively. Expanding each term out to first order we have

$$\mathcal{H} = -\sum_{i=1}^{N}\sum_{j=1}^{N} J_{ij}\boldsymbol{S}_i \cdot \boldsymbol{S}_j - \sum_{i=1}^{N} k_u(\boldsymbol{S}_i \cdot \hat{\boldsymbol{e}}_u)^2 - \sum_{i=1}^{N} \mu_i \boldsymbol{S}_i \cdot \boldsymbol{H}_{\text{app}}. \tag{2.30}$$

The largest contribution comes from the isotropic exchange interaction $\mathcal{H}_{\text{exch}}$. In principle this involves a double summation over the entire system, first through all spins $\boldsymbol{S}_i$ and then all of the neighbours $\boldsymbol{S}_j$, though in practice a truncation of the interaction range is normally implemented in order to reduce computational load. The next contribution comes from the uniaxial anisotropy. Note that here the k_u has been brought inside the sum in order to account for systems with multiple sublattices, which is a common theme in this thesis. Following the same principle, the magnetic moment μ_i is brought inside the sum in the Zeeman term to account for different sublattices coupling to the external field with different strengths.

2.1.6 The Landau-Lifshitz-Gilbert equation

In order to predict the dynamics of a magnetic system, we utilise the derivative of the spin Hamiltonian to calculate the precession of each atomic moment over a series of time steps. This is done by treating each moment as interacting with an *effective* field, denoted by $\boldsymbol{H}^i_{\text{eff}}$, where i indicates the spin with which the field is interacting. The effective field is described by

$$\boldsymbol{H}^i_{\text{eff}} = -\frac{1}{\mu_s}\frac{\partial \mathcal{H}}{\partial \boldsymbol{S}_i}. \tag{2.31}$$

Thus the effective field is given by the negative first derivative of the spin Hamiltonian given in (2.30) with respect to the atomic spin vector. The local spin moment μ_s is included within the effective field in order to simplify the units. In this way, given a Hamiltonian in Joules, the field is expressed in units of Tesla [48].

Using this effective field term, one is able to model various aspects of the system including its time evolution, ground states, and thermal fluctuations, via integration of the Landau-Lifshitz-Gilbert (LLG) equation.

In its original form, first derived by Landau and Lifshitz in 1935 [73], the Landau-Lifshitz equation as it is called, is given by

$$\frac{\partial \boldsymbol{m}}{\partial t} = -\gamma[\boldsymbol{m} \times \boldsymbol{H} + \alpha \boldsymbol{m} \times (\boldsymbol{m} \times \boldsymbol{H})] \tag{2.32}$$

where $\boldsymbol{m}$ is a unit vector representing the direction of the system magnetisation, $\boldsymbol{H}$ is the externally applied field, γ is the gyromagnetic ratio, and α is a material-dependent phenomenological damping constant. Here the damping constant α is representative of a coupling between the magnetisation of the sample and a heat bath. In the form given in (2.32), the rate of relaxation of the magnetisation to the field vector is a linear function of the damping parameter. This was shown later

to produce unphysical behaviour in materials with high α by Gilbert [74]. Gilbert introduced a modified damping term to rectify this, which behaves as a damping 'force' analogous to the classical friction force which acts on a particle in motion in a viscous fluid and is proportional to the velocity of the particle [74]. The alteration to the original equation resulted in what is now called the Landau-Lifshitz-Gilbert equation. While originally the LLG equation was derived as a way of modelling the macroscopic magnetisation of a magnetic sample, it applies well as a description of the dynamics of the magnetisation of small magnetic volume elements, and has come to be used as the standard master equation in numerical micromagnetics [48].

The LLG equation can be extended further to the atomistic scale, and is the standard equation of motion also in the atomistic spin dynamics model, describing the precession of the atomistic spin vector with time around an effective field [48]. In the atomistic formalism, it is given by

$$\frac{\partial \boldsymbol{m}}{\partial t} = -\frac{\gamma}{(1+\lambda^2)}[\boldsymbol{S}_i \times \boldsymbol{H}^i_{\text{eff}} + \lambda \boldsymbol{S}_i \times (\boldsymbol{S}_i \times \boldsymbol{H}^i_{\text{eff}})] \tag{2.33}$$

where $\boldsymbol{S}_i$ a unit vector representing the magnetic spin moment at site i, $\boldsymbol{H}^i_{\text{eff}}$ is the effective field at each atomic site i, $\gamma = 1.76 \times 10^{11}$ rad $\cdot$ s^{-1}T^{-1} is the electron gyromagnetic ratio which governs the frequency of precession, and λ is the microscopic damping parameter. The first term of (2.33) describes the precessional motion of the atomic spin vector about the effective field vector $\boldsymbol{H}^i_{\text{eff}}$; from the cross product the torque on the magnetic moment is orthogonal to $\boldsymbol{S}_i$ and $\boldsymbol{H}^i_{\text{eff}}$. This can be derived from first principles as the quantum mechanical interaction between the atomic spin and the magnetic part of the effective Kohn-Sham potential [72].

The second term in (2.33) is the damping term, which allows for a transfer of energy between the spin system and the environmental heat bath, aligning the magnetic moment along the effective field direction with a coupling strength given by

the constant λ. The use of the microscopic damping parameter λ is an important difference between the application of the LLG equation in the micromagnetics formalism and the application in the atomistic case. In micromagnetics, the damping parameter encapsulates effects from both intrinsic (e.g. spin-lattice and spin-electron interactions) and extrinsic factors (e.g. demagnetisation fields, shape effects, structural defects, doping), while in the atomistic LLG, only intrinsic contributions are absorbed into the damping constant. The exclusion of extrinsic contributions allows explicit descriptions of these effects in the model, for example elemental substitution as discussed in chapter 7.

Temperature effects

The equation of motion governing the dynamics of the atomic spins as given in (2.33), as yet includes no description of any thermodynamic effects, an important aspect of the atomistic spin dynamics model. In order to approximate the effects of thermal fluctuations in the system a stochastic term is augmented to the LLG equation. This is the Langevin dynamics approach. Using this approach it is possible, for example, to effectively model the dependence of the system magnetisation on temperature. In this scenario, the introduction of temperature fluctuations results in fluctuations of the atomic spin moment $\boldsymbol{S}_i$. While the magnitude of the moment remains constant, the induced stochasticity results in a statistical disordering of the spin ensemble, reducing the total system magnetisation. While this picture is a simple one, the model is able to reproduce experimental temperature effects to a high degree of accuracy, as shall be shown later.

The stochastic term is added to the effective field such that the effective field is now given by

$$\boldsymbol{H}^i_{\text{eff}} = -\frac{1}{\mu_s}\frac{\partial \mathcal{H}}{\partial \boldsymbol{S}_i} + \boldsymbol{H}^i_{\text{th}} \tag{2.34}$$

where $\boldsymbol{H}_{\text{th}}^{i}$ is the thermal field acting on the spin. The formalism of the thermal field is based on the Brownian approach, wherein the assumption is made that the correlation times of the random thermal forces is much shorter than the response times of the system [47]. The thermal noise is said in this case to lie within the 'white' limit [47], and hence the thermal noise term can be simplified to a pseudo-random number, generated from a Gaussian distribution of width

$$\sigma = \sqrt{\frac{2\lambda k_B T}{\gamma \mu_s \Delta t}} \tag{2.35}$$

where γ and λ retain their meanings from before, k_B is the Boltzmann constant, T the simulation temperature, μ_s is the magnitude of the spin magnetic moment, and Δt is the integration time step. With the inclusion of the Langevin term in the effective field and in turn in the LLG equation, the equation of motion is sometimes referred to as the stochastic LLG (sLLG) or the Landau-Lifshitz-Gilbert-Langevin (LLGL) equation.

A stochastic perturbation of this type is in general referred to as a Wiener process [75]. A Wiener process scales with the time step as $\sqrt{\Delta t}$, however in this case it is important that the factor $\sqrt{\Delta t}$ be placed in the denominator, because the integration step (discussed later) introduces an extra factor Δt, which multiplies the noise term in (2.33). Thus, in the end the Δt and $1/\sqrt{\Delta t}$ cancel and the spin is updated with factor $\sqrt{\Delta t}$.

2.2 Experimental techniques for probing magnetic properties

There are a wide array of advanced experimental techniques for probing the macroscopic and microscopic properties of magnetic materials. Data from experiment are

used widely throughout this thesis as an important tool for parameterising the atomistic spin model.

Crystal structure is most commonly probed by means of an x-ray or neutron diffractometer [76–78]. These usually contain some source of radiation, a monochromator, and slits to control the shape of the beam [79]. An advantage of using neutron diffraction is that the neutrons possess an intrinsic mangetic moment which can interact with magnetic moments within the sample, giving information about the orientations and sizes of moments in the sample.

A very common piece of apparatus used for measuring the magnetisation of a sample is the vibrating-sample magnetometer (VSM) [80–82]. The VSM works by sinusoidally vibrating a magnetised sample, and measuring the induced voltage in a pickup coil. The induced voltage is proportional to the magnetisation of the sample, but does not depend on the amplitude of the applied magnetic field [83]. It is also commonly used to measure hysteresis properties of a sample by sweeping a magnetic field, or the Curie temperature by exposing the sample to a range of temperatures. Another commonly used piece of equipment is a superconducting quantum interference device (SQUID), which is a particularly sensitive magnetometer useful for measuring very subtle magnetic fields [84].

Chapter 3

Methods

The atomistic spin dynamics calculations in this thesis were performed using the VAMPIRE software package [48]. VAMPIRE is a general purpose atomistic spin dynamics code that is open-source and freely available from http://vampire.york.ac.uk. The code was first written and is curretly maintained by Dr. Richard Evans, though has expanded a great deal over the course of its approximately 11 year lifetime, with input from a number of contributors. This chapter will detail the implementation of the theoretical ideas presented in the previous chapter.

3.1 Solving the stochastic LLG equation

The stochastic LLG equation describes the precession of the atomistic spin moments in a non-deterministic way. To extract the magnetisation, one must solve the equation to get $\boldsymbol{S}_i$. With the inclusion of the stochastic term, the LLG becomes intractable analytically, thus it must be solved numerically.

In general there are a wide range of methods available for the numerical solution of stochastic differential equations, and the choice of solver usually involves a trade-off between accuracy and efficiency. Due to the large number of interactions in an

atomistic spin simulation and, in the case of equilibrium calculations, long simulation times on the order of nanoseconds, a stable and very fast solver is required.

A number of semi-implicit and implicit solvers have been used to integrate the sLLG equation [85–87]. These have the advantage of conserving the spin length, a requirement of the LLG equation. In our model the chosen integration scheme is known as the improved Euler method or *Heun* method; an explicit, predictor-corrector method which has the advantage of being relatively straightforward to implement. It should be noted that the Heun method does not intrinsically conserve the length of the spin, however a simple re-normalisation of the spin length after each of the predictor and corrector steps circumvents this problem, and ensures stability and convergence to the Stratonovich solution [48]. While this re-normalisation step would ordinarily have implications for the conservation of energy in the system, this is not a concern here as the LLG equation is effectively coupled to a thermal bath by the noise term in (2.34).

The Heun method is essentially equivalent to the second order Runge-Kutta method [88]. It makes use of a forward Euler step as a predictor, and then corrects the prediction using the trapezoidal method. Thus each integration step involves two partial steps, shown schematically in Fig. 3.1. The essential idea is that given, for example, a concave-up curve, the Euler method will underestimate the gradient at all points between t and $t + \Delta t$. If the gradient of the tangent at the other end of the interval is taken, it will have the opposite problem. Heun's method thus takes the average of the underestimating and the overestimating gradients to give an improved solution. The method has a local discretisation error of third order in Δt, and a global discretisation error of second order in $\Delta = \max_t \Delta t$ [89].

The new spin direction $\boldsymbol{S}_i'$ as calculated using the Euler scheme for a given effective field $\boldsymbol{H}_{\text{eff}}^i$ is given by

$$\boldsymbol{S}_i' = \boldsymbol{S}_i + \Delta \boldsymbol{S} \Delta t \tag{3.1}$$

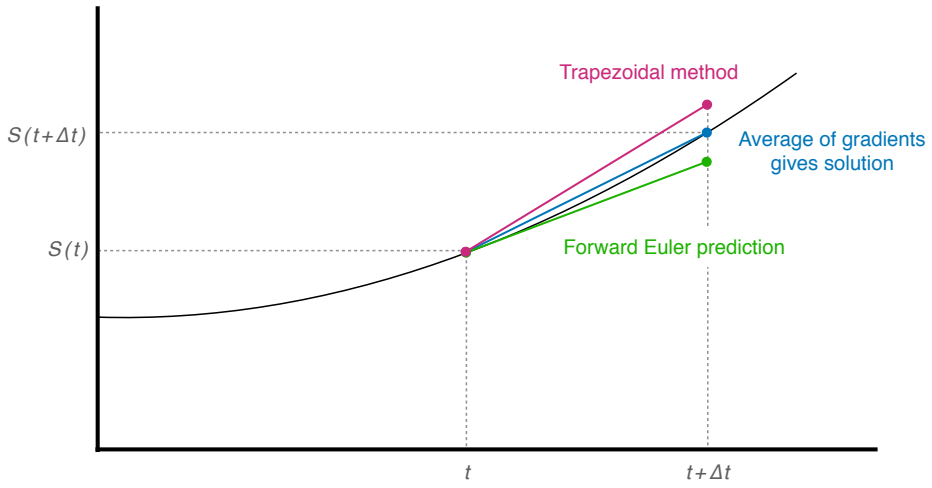

Figure 3.1: Integration using the Heun predictor-corrector algorithm. First, a prediction is made using the gradient at time t (an Euler step). Second, another estimation is made based on the gradient at the point predicted by the Euler step. This acts as a 'corrector' to the initial estimation and an average is taken of the two gradients to give the Heun step.

where

$$\Delta \boldsymbol{S} = -\frac{\gamma}{(1+\lambda)^2}[\boldsymbol{S}_i \times \boldsymbol{H}_i + \lambda \boldsymbol{S}_i \times (\boldsymbol{S}_i \times \boldsymbol{H}_i)]. \tag{3.2}$$

At this point the spin vector is renormalised to unity. After this predictor step, the effective fields are re-evaluated given the new spin directions, though the thermal fluctuations do not change at this time. The second partial integration step then uses the predicted step and the re-calculated effective field vector to correct the initial step, giving the direction of $\boldsymbol{S}$ at time $t + \Delta t$. Thus we have

$$\boldsymbol{S}_i^{t+\Delta t} = \boldsymbol{S}_i + \frac{1}{2}[\Delta \boldsymbol{S} + \Delta \boldsymbol{S}']\Delta t \tag{3.3}$$

as the final solution, where

$$\Delta \boldsymbol{S}' = -\frac{\gamma}{(1+\lambda)^2}[\boldsymbol{S}_i' \times \boldsymbol{H}_i' + \lambda \boldsymbol{S}_i' \times (\boldsymbol{S}_i' \times \boldsymbol{H}_i')]. \tag{3.4}$$

3.2 Metropolis Monte Carlo algorithm

The stochastic LLG equation is a useful way of modelling the dynamical properties of a magnetic system, for example reversal processes. However in cases where we wish to look for the equilibrium properties of a system, the Monte Carlo integration method can often be more useful. One reason for this is that, while the sLLG method is ergodic, that is, explorative of the whole phase space, the timescale of the exploration is often impractically long. Therefore when rapid convergence to the equilibrium configuration is desired, it can be more computationally efficient to use the Monte Carlo algorithm, which is characterised by its ergodicity. In particular it is the Metropolis Monte Carlo algorithm [90] which is useful for exploring the phase space of a magnetic ensemble. The reason for this is that the Metropolis algorithm is what is known as an importance sampling method; that is to say, the important points in the phase space are sampled preferentially, important meaning those regions of the phase space where the equilibrium state is likely to reside [91]. This is achieved via a Markov chain of states $\boldsymbol{X}_n \rightarrow \boldsymbol{X}_{n+1} \rightarrow \boldsymbol{X}_{n+2} \rightarrow \ldots$, which are generated recursively one after another depending probabilistically on, and only on, the state that came before. Therefore, implementation of the Metropolis method requires careful selection of spin configurations, such that the phase space is explored in a way that ensures ergodicity, but also in a way that is efficient.

The procedure of the Metropolis Monte Carlo algorithm is as follows:

1. A random spin i from the ensemble is selected

2. Its initial spin direction $\boldsymbol{S}_i$ is changed to a new trial direction $\boldsymbol{S}_i'$

3. The change in energy between the new and old spins is calculated such that $\Delta E = E(\boldsymbol{S}_i') - E(\boldsymbol{S}_i)$

4. $\boldsymbol{S}_i'$ is then accepted or rejected based on an acceptance probability $P = \exp(-\Delta E/k_B T)$ by comparison with a random number generated between 0 and 1

5. If $\Delta E < 0$, the energy of the configuration has been lowered by the new spin, the probability $P > 1$ and the spin is automatically accepted

6. Steps 1-5 are repeated N times where N is the size of the sample, with N moves constituting a single Monte Carlo step

There are certain statistical requirements of a Monte Carlo algorithm. One is ergodicity as mentioned above, another is reversibility. The reversibility condition requires that the probability of reaching one state from another is equal to the probability of a change of state in the opposite direction; that is to say, $P(\boldsymbol{S}_i \rightarrow \boldsymbol{S}_i') = P(\boldsymbol{S}_i' \rightarrow \boldsymbol{S}_i)$ [91]. Ergodicity is easily achieved by allowing the trial spin $\boldsymbol{S}_i'$ to point in any direction. This has the drawback of a very high rate of rejection due to the fact that with the exchange energy term in the system Hamiltonian, the energy cost of pointing a spin far away from the direction of its neighbour is very high resulting in a large number of steps being required to reach an equilibrium state. An acceptance rate of approximately 50% is desirable for efficient equilibration [48]. A very efficient method for sampling the phase space was proposed by Hinzke and Nowak [92], whereby a combination of different types of trial move is employed: uniform random, spin flip, and a small angle move. These are illustrated schematically in Fig. 3.2. Formally these three trial moves can be described by

$$\begin{aligned} \boldsymbol{S}_i' &= \frac{(u,v,w)}{\sqrt{(u^2+v^2+w^2)}} && \text{uniform random} \\ \boldsymbol{S}_i' &= \frac{\boldsymbol{S}_i + \delta}{|\boldsymbol{S}_i + \delta|} && \text{small step} \\ \boldsymbol{S}_i' &= -\boldsymbol{S}_i && \text{spin flip} \end{aligned} \tag{3.5}$$

where u, v, and w are random numbers, and δ is some small deviation from $\boldsymbol{S}_i$.

Each type of trial move is effective in certain scenarios. The small angle trial move has to overcome the anisotropy energy barrier in order for a switching event to take place (see Fig. 2.3) which requires high energy, however it can efficiently simulate coherent rotation. The uniform random type trial move is able to take larger steps, and thus is able to simulate nucleation type switching, and no single spin is required to overcome the energy barrier as the spin can switch through the barrier by finding a trial move on the other side. The spin flip type moves can efficiently simulate nucleation even in the limit of large anisotropy, but has the drawback of not sampling the full phase space. Rather, it is akin to an Ising type model. Thus each type has advantages and disadvantages, and used in combination such that one type of trial move is used for each Monte Carlo step, gives the most efficient sampling [92].

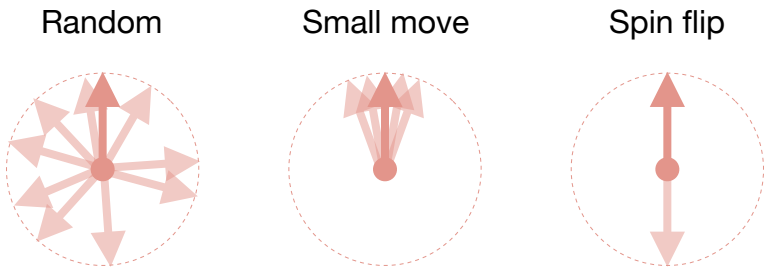

Figure 3.2: Schematic showing three types of Monte Carlo trial moves used in the atomistic model. The combination of these three types allows for more efficient movement through the phase space.

3.3 Néel anisotropy model

The origins of the magnetocrystalline anisotropy energy can give important insights into the effects of microstructural features and grain interfaces on nucleation processes which may be a primary cause of the weakened coercivity seen in manufactured $Nd_2Fe_{14}B$-based sintered magnets [34]. It is known that in rare-earth transition-

metal based compounds, at the grain-boundary interfaces there is a breakdown in the local symmetry with measurable strain on the crystal lattice, an idea explored in more detail in chapter 6. It has been suggested that this loss of crystal symmetry could result in a reduction in the local anisotropy [93]. In an ideal scenario one would use *ab initio* methods to probe the local effects on the anisotropy constants in these regions. Unfortunately, using current methods and with limitations on computational power the complexity and size of these grain boundary features prohibits the use of *ab initio* calculations. Instead we look to the famous Néel pair-interaction anisotropy model, first conceived of by Néel in 1954 [94]. The model has been commonly applied to nanoparticles in order to quantify the anisotropy due to loss of coordination at the surfaces [95, 96], however in this thesis we apply the Néel model to the bulk to probe the local variations in anisotropy in low symmetry regions.

As suggested by Néel, the leading contribution to the anisotropy due to pairs of atoms can be expressed as

$$\mathcal{H}_A = \frac{1}{2} \sum_{i,j} L_{ij} (\boldsymbol{S}_i \cdot \boldsymbol{e}_{ij})^2 + \dots . \tag{3.6}$$

where the vector $\boldsymbol{S}_i$ represents the spin on site i and the vector $\boldsymbol{e}_{ij}$ points from site i to each of its neighbouring spins j within some cut-off radius r_{cut}. Both vectors are normalised to unity. L_{ij} represents the strength of the pairwise coupling. Here the coupling strength is made to be dependent on the atomic separation between neighbours, such that $L_{ij} = L_{ij}(r)$. Its magnitude is determined by fitting to the magnetocrystalline anisotropy energy found by experiment. As a first approximation L_{ij} is set to drop off exponentially with the atomic separation r, and is written as

$$L_{ij}(r) = L_0 + L_r \exp(-r/r_0) \tag{3.7}$$

where r is the separation between neighbours, r_0 is a characteristic distance, and L_0 and L_r are fitting constants. L_0 is simply included as an extra phenomenological degree of freedom to ensure optimal fitting to experimentally measured magnetocrystalline anisotropy values. Used in this way, the L_{ij} factor is weighted such that nearer neighbours have a stronger effect than those further away, therefore the atomic spin is dependent on changes to the local crystal environment, and the anisotropy will change accordingly. In this formalism, the neighbouring charges are treated as point charges as a first approximation.

One shortcoming encountered in the implementation of this method is its computational cost. As written in (3.6), a loop over all atomic sites as well as all neighbours is required, thus the computation time is proportional to N^2 where N is the number of atoms. In order to circumvent this problem we reformulate (3.6) into a tensor form. We note that given a crystal lattice, whether it be relaxed via molecular dynamics simulation or generated using a primitive cell, once input into the atomistic spin model there is complete translational invariance of the atomic coordinates. Therefore, the vector $\boldsymbol{e}_{ij}$ is a constant quantity and need not be included in the integration over neighbours. The same reasoning can be applied to the quantity L_{ij}, which is invariant once the crystal structure is set up. Both the vector $\boldsymbol{e}_{ij}$ and L_{ij} are removed from the sum and we have the tensor

$$L_{ij}(\boldsymbol{r}) \begin{pmatrix} e_x e_x & e_x e_y & e_x e_z \\ e_y e_x & e_y e_y & e_y e_z \\ e_z e_x & e_z e_y & e_z e_z \end{pmatrix} \tag{3.8}$$

where $L_{ij}(r)$ is now a pre-factor. $\boldsymbol{e}_{ij}$ of course must be vectorially summed over all neighbours before being removed from the integral. The advantage of this reformulation is that the integral need only be carried out once rather than at every time step. Once calculated, there are N tensors, which can be stored before the simulation

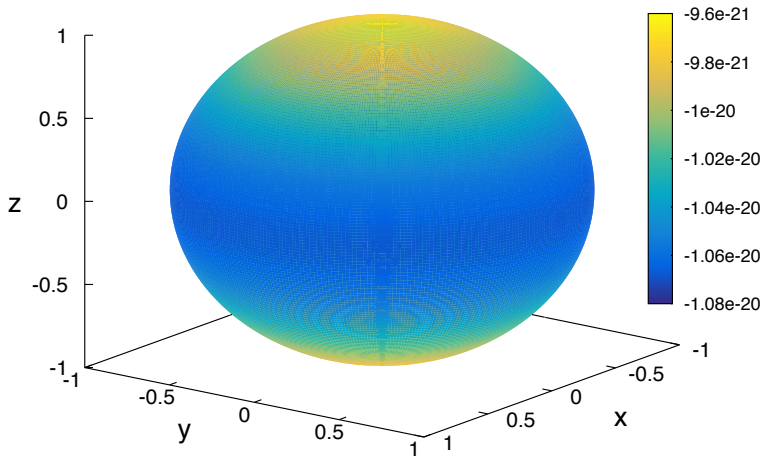

Figure 3.3: Energy surface generated by applying the Néel anisotropy model to the Fe sublattice of the $Nd_2Fe_{14}B$ unit cell projected onto a unit sphere. The scale is given in Joules, and the colour indicates the energy associated with all spins of the Fe sublattice being oriented in a given direction. The calculated surface shows that there is a preferential alignment for the sublattice in the $+z$-direction, corresponding to the c crystallographic axis in the unit cell.

begins. During the simulation, the anisotropy energy is found by integrating over the spin directions $\boldsymbol{S}_i$. The site-resolved anisotropy energy is given by

$$\mathcal{H}_A^i = \langle \boldsymbol{S}_i | \boldsymbol{e}_{ij} | \boldsymbol{S}_i \rangle \tag{3.9}$$

where $L_{ij}(r)$ has been absorbed into the tensor as a weighting constant. As a straightforward validation of the model we apply the calculation to the Fe sublattice of the $Nd_2Fe_{14}B$ unit cell. It is well known that the Fe sublattice selects the c-axis as the easy axis of magnetisation [22].

From Fig. 3.3 it can be seen that the Néel model applied to the $Nd_2Fe_{14}B$ unit cell successfully reproduces the result that the Fe sublattice prefers to align along the c axis, showing a classic uniaxial energy dependence on the angle. In this simulation a cut-off radius of 5 Å was selected and an angular discretisation of 1° was used. The result comes naturally out of the Néel model and is a direct consequence of the crystal structure of the Fe sublattice.

3.4 Cell size scaling of micromagnetic parameters

As discussed earlier, one difficulty faced by micromagnetics modelling is the scaling of the magnetic properties with cell size. This was first investigated by Dobrovitski et al. [53] and Grinstein and Koch [54]. The coarse meshing of the micromagnetic variables leads in general to an overestimation of the Curie temperature. Essentially this means that the saturation magnetisation, magnetocrystalline anisotropy and the exchange stiffness must be treated as dependent on cell size (L), i.e. $K = K(L,T)$, $M_{\mathrm{s}} = M_{\mathrm{s}}(L,T)$, and $A = A(L,T)$. In chapter 5, the atomistic model will be used to calculate the exact variations, linking the atomistic and micromagnetic models in a multiscale approach. The method by which this is done will be outlined here.

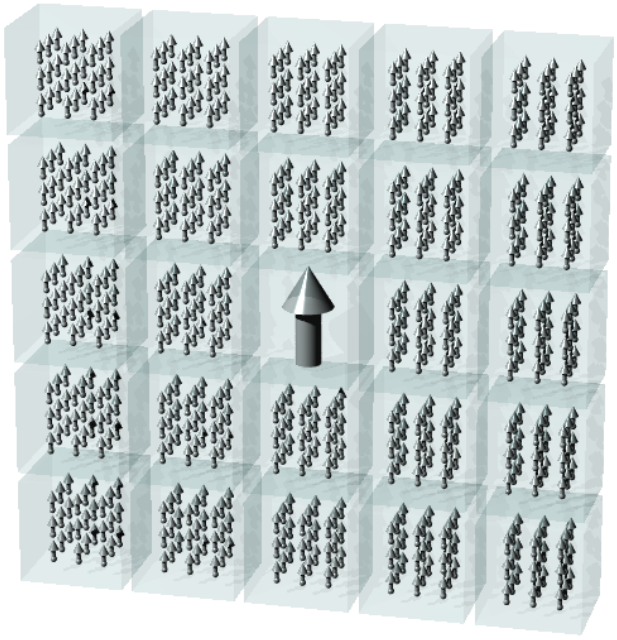

Figure 3.4: Schematic showing the method used to determine the cell-size and temperature scaling behaviour in $Nd_2Fe_{14}B$ and a generic BCC system. The magnetisation is averaged over a central cell in the system, approximating the micromagnetics method, and compared with the total system properties.

The procedure for determining the cell size scaling of the magnetisation is as follows. First the unit cell of the material is generated and parameterised using the

methods discussed in section 2.1. A large cell is then simulated with dimensions 10 x 10 x 10 nm, with periodic boundary conditions to mitigate any finite size effects and to ensure a good approximation to bulk properties. Within the large system the properties are averaged over a smaller cell in order to evaluate the cell-size and temperature dependent properties relevant for micromagnetic models. A schematic of the averaging cell is shown in Fig. 3.4.

The determination of the cell size dependence of the magnetocrystalline anisotropy, K, requires a slightly different approach. In general, with atomistic models the best approach for extracting the temperature dependence of K is via the constrained Monte-Carlo method [97], an extension of the Metropolis algorithm discussed in section 2.1.

The Metropolis algorithm works on a basis of generating trial moves for N random spins in the system, where N is the total number of spins. The trial move is then accepted or rejected based on the ratio of the Boltzmann probability densities of the initial and final states, given by $\exp(-\beta\mathcal{H})$, where $\beta = 1/kT$. In the constrained Monte-Carlo method, the total magnetisation vector of the system $\hat{\boldsymbol{M}}$ is constrained to a single direction which can be chosen arbitrarily. At each step, *two* trial moves on two individual spins in the system are generated, and these must be chosen such that the direction of $\hat{\boldsymbol{M}}$ is conserved. This is done by first selecting a single spin $\hat{\boldsymbol{S}}_i$ at random, displacing the spin by some amount to obtain a new spin $\hat{\boldsymbol{S}}_i'$, and then choosing a compensation spin $\hat{\boldsymbol{S}}_j$ and displacing that by an amount such that $\hat{\boldsymbol{M}}$ is conserved. The total energy difference $\Delta\mathcal{H} = \mathcal{H}' - \mathcal{H}$ is then calculated and the two moves are accepted according to the acceptance function as in the case of the normal method. Running the simulation for some number of time steps, we are then able to calculate the restoring torque on the system as a function of the constraining angle of the magnetisation.

As a validation of the method, the temperature dependence of the restoring torque for a generic BCC system is shown in Fig. 3.5a. The restoring torque is defined by

$$\boldsymbol{\tau} = \boldsymbol{M} \times \boldsymbol{H} \tag{3.10}$$

where $\boldsymbol{H}$ is the effective field and $\boldsymbol{M}$ is the direction in which the system magnetisation is constrained.

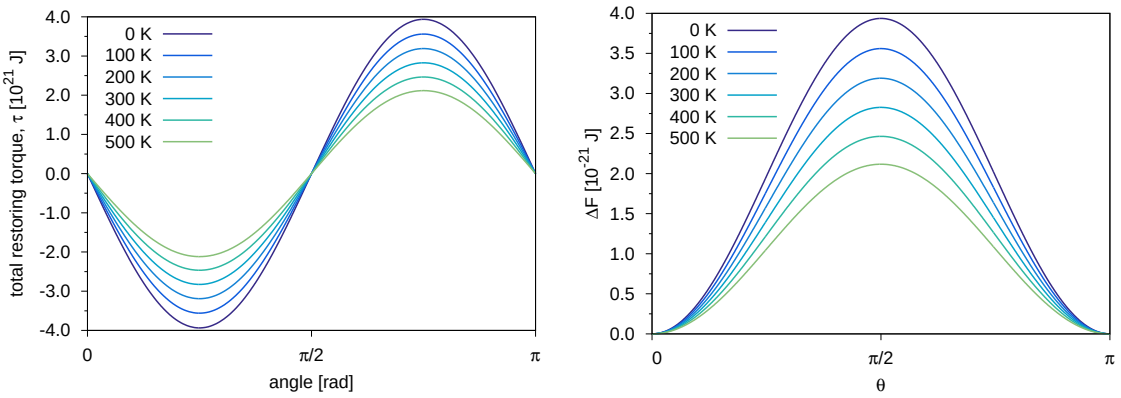

(a) (b)

Figure 3.5: (a) Angular variation of the y-component of the restoring torque as a function of temperature for a generic BCC system with $T_c \approx 1000$ K. (b) Integration of τ with respect to θ from 0 to π gives the change in the free energy.

Each curve has a $\sin(2\theta)$ form, characteristic of uniaxial anisotropy. At 500 K, approximately half of the T_c, there is a 50% reduction in the restoring torque, which is similar to results given by Asselin et al. [97]. From here the change in the free energy $\Delta\mathcal{F}$ is determined via an integration over the angle, such that

$$\mathcal{F}(\theta) = \int_0^{\pi} \tau_y \cdot d\theta \tag{3.11}$$

where the proportionality constant K gives the magnitude of the effective uniaxial magnetocrystalline anisotropy constant K_u^{eff}. The angular dependence of $\Delta\mathcal{F}$ is shown in Fig. 3.5b. The energy is a maximum when the magnetisation is in-plane and has

minimum energy when the magnetisation is aligned along the anisotropy axis, as expected for a uniaxial system.

The results obtained using these methods for the cell size scaling of the magnetic parameters will be presented in chapter 5.

Chapter 4

Core/shell $Nd_2Fe_{14}B/\alpha$-Fe nanoparticles

Recent advancements in nanoscale fabrication techniques have opened the way for a new class of materials that combine hard and soft magnetic materials to produce so-called exchange coupled nanocomposites, or *exchange spring* magnets [31, 98, 99], with large anisotropy provided by the hard phase and high saturation magnetisation provided by the soft phase. In addition to having better overall magnetic properties than either constituent material, exchange spring magnets have the advantage of reducing the overall material cost by reducing the proportion of the expensive hard phase in favour of more cost-effective and readily-available soft materials such as Fe or Co. Since first suggested by Kneller and Hawig in 1991 [100], various theoretical predictions have suggested that their maximum energy product could be in the region of 950 kJm^{-3}, which is remarkable when compared to what one could hope to achieve using only permanent magnets, however this has not so far been realised experimentally.

The term exchange spring magnet refers in general to any structure in which there is a magnetically hard phase exchange coupled to a magnetically soft phase.

These might include a simple multilayer system, such as that investigated by Skomski and Coey [101], or more complicated structure with numerous phases such as the 'Battenburg' magnet described by Bance et al. [51]. Initially proposed for permanent magnet applications [102], they have since gained interest in numerous other areas including magnetic recording media [103, 104] and biomagnetism [105, 106].

Core/shell magnetic nanoparticles are an advanced form of exchange spring magnet, which have only become possible to fabricate in the last 10–15 years due to advances in synthetic chemistry allowing exceptional control over growth parameters [107]. The idea behind core/shell nanoparticles is to have an increased area across which the hard and soft phases are coupled, thus multiplying the benefits that come with exchange spring magnets.

Skomski and Coey [101] predicted theoretically that in a bi-magnetic multilayer system comprised of $Sm_2Fe_{17}N_3$ as the hard phase and $Fe_{65}Co_{35}$ as the soft phase, a $(BH)_{\max}$ of 1 MJm^{-3} could be achieved. Despite the great potential for improving $(BH)_{\max}$ using bi-component ferromagnetic materials, the majority of research has focused on FM/AFM or AFM/FM core/shell nanostructures [107]. Recently however, Liu et al. reported values of 360-440 kJm^{-3} for bi-component ferromagnetic FeCo and Fe coated $Nd_2Fe_{14}B$ particles [30]. It has been suggested that the reason for the disparity between experimental and predicted values might be that experiments have been carried out on randomly-oriented particles rather than magnetically aligned systems [107].

There are a number of methods used in the literature to treat exchange-spring magnets computationally. Currently the most common [108–111] is based on the micromagnetics formalism, which approximates the magnetisation of the system as a spatially-continuous vector field (for details see section 1.2).

Here will be presented a systematic investigation of the magnetic properties and performance of idealised core/shell nanostructures with soft/hard morphology, using

$Nd_2Fe_{14}B$ for the hard phase and α-Fe for the soft phase. The systems are modelled across a range of temperatures using an atomistic spin dynamics (ASD) model. The ASD approach is the most appropriate way to deal with interface effects and also the effects of elevated temperatures, which form an important part of the analysis.

First, the system setup is described. Then calculations of the temperature dependence of the magnetisation will be shown, which demonstrate an important enhancement of the magnetisation of the hard phase with increased α-Fe content. This is followed by a systematic investigation of the temperature dependence of the coercive field and energy product, demonstrating enhancement of the properties of nanoscale systems due to the magnetisation enhancement effect brought about by the α-Fe phase.

4.1 Temperature re-scaling

Before proceeding with the parameterisation of the core/shell system, we note briefly the method used to correctly reproduce the temperature dependent effects. In the classical atomistic model, all directions are permitted for each spin vector. This gives an incorrect temperature dependence for the system magnetisation at low temperatures. One method of correcting this is to use the phenomenological spin temperature rescaling (STR) method suggested by Evans et al. [112], which has the effect of reducing the spin fluctuations in agreement with experiment. The approach uses an interpolation between low-temperature Bloch behaviour and critical behaviour, such that the magnetisation can be described by

$$m(\tau) = (1 - \tau^{\alpha})^{\beta}, \tag{4.1}$$

where $\tau = T/T_{\mathrm{c}}$, α is a phenomenological constant and β is the critical exponent. β is assumed to be the same for the classical simulation and experiment. Setting $\alpha = 1$

(giving the classical Heisenberg dependence of the magnetisation), we can determine both β and T_c, which are constants. With these, we are able to perform a secondary fit to experimental data to determine α. Using this method gives re-scaling constants $\alpha_{Fe} = 2.876$ and $\alpha_{Nd} = 1.756$, which we apply to the α-Fe and $Nd_2Fe_{14}B$ sublattices respectively, allowing the temperature dependence of the saturation magnetisation and energy product of the composite system to be compared to experiment.

4.2 Parameterisation

A schematic of the modelled core/shell system is shown in Fig. 4.1. For this system we use a generic spin model for the $Nd_2Fe_{14}B$ shell with BCC crystal structure. In this way each atomistic spin in the system is representative of a single $Nd_2Fe_{14}B$ unit cell containing 68 atoms: 54 Fe atoms, 8 Nd atoms, and 4 B atoms. The parameters used for each material are given in Table 4.1. A nearest-neighbour Heisenberg exchange approximation was used.

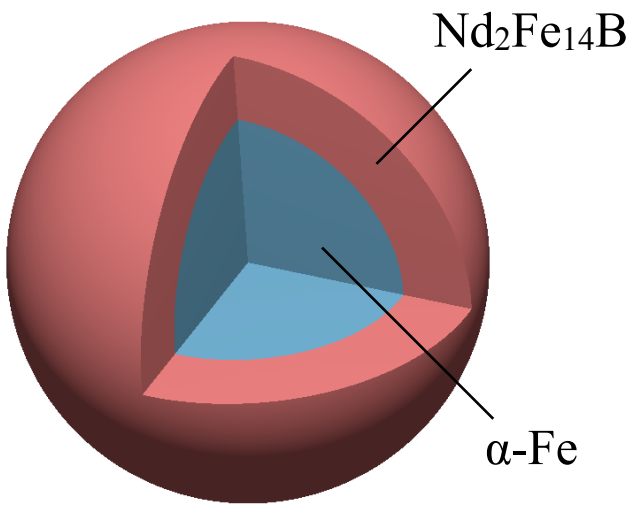

Figure 4.1: Schematic showing the modelled core/shell nanoparticle. The structure has a soft, high saturation magnetisation α-Fe core and a hard, large anisotropy $Nd_2Fe_{14}B$ shell.

	$Nd_2Fe_{14}B$	α-Fe
μ_s [μ_B]	1.88	2.2
k_u [J/atom]	1.482×10^{-22}	4.01×10^{-25}
J_{ij} [J/link]	4.04×10^{-21}	7.20×10^{-21}
λ	1.0	1.0
α	1.756	2.876

Table 4.1: Summary table of model parameters and their units. μ_s is the atomic spin moment, k_u the on-site magnetocrystalline anisotropy constant, λ is the microscopic damping parameter, α the temperature rescaling exponent, and J_{ij} the intra-phase exchange coupling strength. Between phases an average value of 5.0×10^{-21} J/link was used.

We have carried out a systematic investigation of the properties of core/shell $Nd_2Fe_{14}B/\alpha$-Fe nanoparticles. We first establish that the parameters for the isolated phases produce behaviour consistent with experiment. Following this we consider the effect of varying the relative proportions of the phases in the core/shell configuration on the temperature dependent magnetisation of the nanoparticle, followed by an investigation of the hysteresis behaviour of nanoscale systems.

4.3 Static magnetic properties and proximity effect

The temperature dependence of the magnetisation of the two isolated phases was calculated (Fig. 4.2). After re-scaling via the STR method, the simulated data follows the experimental data closely across the whole temperature regime for both the $Nd_2Fe_{14}B$ and α-Fe phases. Fitting using the Curie-Bloch equation (given by (5.9)) gives values for T_c of 584.3 K and 1040.0 K for $Nd_2Fe_{14}B$ and α-Fe respectively. There is some slight discrepancy in the behaviour of the simulated and experimental $Nd_2Fe_{14}B$ systems, however this is likely due to the fact that the experimental measurement was carried out under an external magnetic field of 800 kA/m, while there

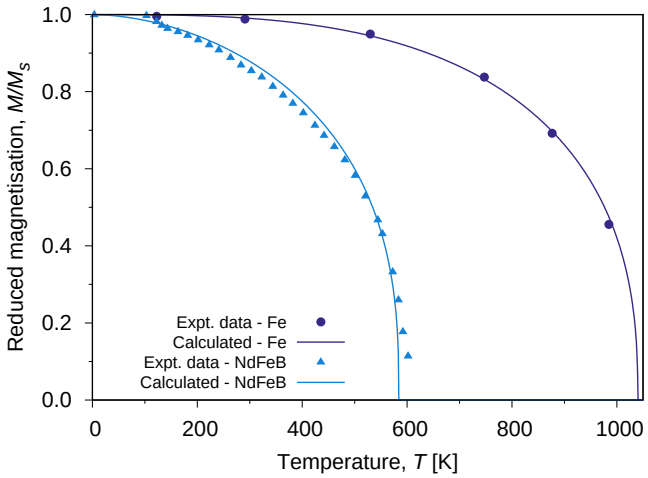

Figure 4.2: Calculated temperature dependent magnetisation for single-phase spherical nanoparticles of diameter 12 nm. The curves are fitted using (5.9) giving values for T_c of 584.3 K and 1040.0 K for $Nd_2Fe_{14}B$ and α-Fe respectively. The experimental data are from Refs. [18] and [113] for the $Nd_2Fe_{14}B$ and α-Fe respectively.

is no field applied to the simulated system. Having parameterised our model to fit the experimental data, we move on to an investigation of the temperature dependence of the composite nanoparticle properties.

Firstly, we investigate the magnetisation of the core/shell system, showing an important proximity effect arising from the polarisation of the hard phase by the α-Fe core. We have calculated the temperature dependence of the magnetisation as a function of the vol% of α-Fe, using the Monte Carlo integration method as outlined in section 3.2. From Fig. 4.3 it can be seen that there is a clear enhancement of the saturation magnetisation across the whole temperature range for increasing vol% of α-Fe. Due to its higher T_c, the gradient of the magnetisation curve for bulk α-Fe is much smaller at low temperatures than that of $Nd_2Fe_{14}B$, which will, in the exchange-coupled case, result in increased magnetisation of the composite phase. The highlighted temperature region in Fig. 4.3 indicates the area of interest when considering electric vehicle motor applications. The enhancement effect is significant towards the high temperature end of this region, where the $Nd_2Fe_{14}B$ begins to de-

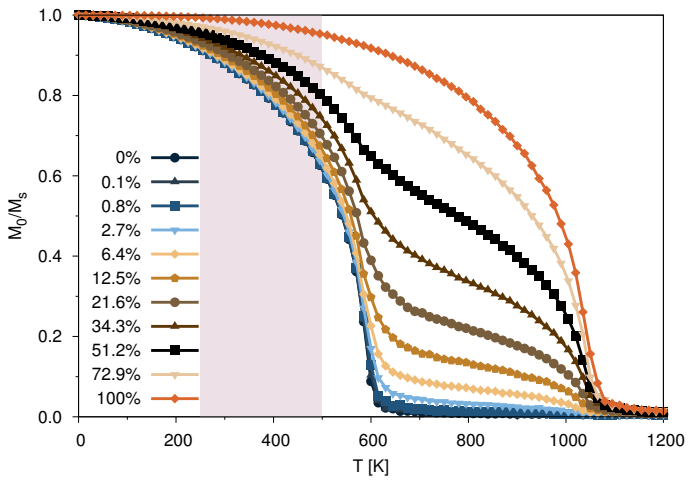

Figure 4.3: The calculated saturation magnetisation as a function of temperature for a 12 nm diameter soft/hard core/shell nanoparticle for varying vol% of α-Fe. Though the curves do not follow the standard Curie-Bloch behaviour, qualitatively it can be said that there is a clear increase in T_c with increasing α-Fe content, as well as improved magnetisation retention across all temperatures considered. The highlighted region indicates the temperature domain generally relevant for automotive applications.

magnetize as T approaches T_c for bulk $Nd_2Fe_{14}B$. The more thermally stable α-Fe phase acts to polarize the shell via the inter-phase exchange coupling.

The extent of the polarisation effect on the hard phase was investigated by calculating the magnetisation of the particle as a function of the radial distance r from the centre of the particle. The particle was discretised into a series of annuli (see Fig. 4.4), and the magnetisation per atom of each annulus calculated.

In the uncoupled case, one would expect a step-function change in the magnetisation at the distance $r = r_c$ where r_c is the radius of the core. In the coupled case considered here, a gradual transition from the soft to the hard phase, with the gradient of $M(\mathbf{r})$ directly proportional to the coupling strength, should be expected.

Fig. 4.5 shows the results of the $M(\mathbf{r})$ calculation. The data show that there is a gradual transition between the higher magnetisation of the soft core and the reduced magnetisation of the hard shell. The polarisation effect of the soft α-Fe core can be seen to penetrate the shell to a depth of $\sim$0.5 nm, or 17% the thickness

of the shell, providing an explanation for the enhancement effect seen in Fig. 4.3. This is an interesting effect, accessible experimentally and with direct implications for applications in systems based on nanoscale materials design.

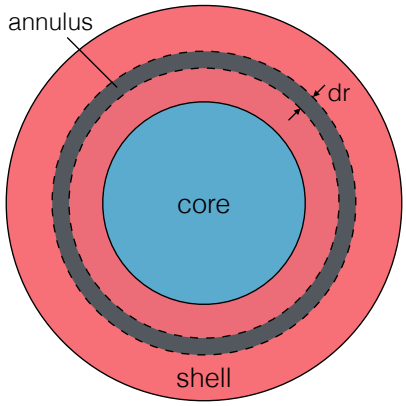

Figure 4.4: Discretisation of core/shell particle into series of annuli of constant width dr, with radius ranging from zero to radius of particle.

We now proceed to investigate the coercivity and energy product of the core/shell structure. While the composite system reduces the temperature dependence of the saturation magnetisation, a high energy product is dependent upon retaining a high coercivity. Since the Fe has a very low anisotropy, its addition will also lead to a reduction in the coercivity of the composite system. We proceed by investigating the coercivity as a function of temperature, followed by a study of the temperature dependence of the energy product as a function of the α-Fe vol%.

Figure 4.6 shows the calculated de-magnetisation curves for the composite system at temperatures of 0 K and 300 K. The calculations were performed using a field sweep rate of 6.0×10^8 Ts^{-1} (real time), which equates to $\sim$ 24,000 steps per field point sweeping between 18.5T and -18.5T, and a field increment of 3×10^{-3} T. The squareness of the loops is evidence of coherent rotation, independent of the Fe vol%, as expected due to the small particle size. It is shown that particles with increased Fe core size show reduced coercivity, however the increased moment (Fig. 4.3) should

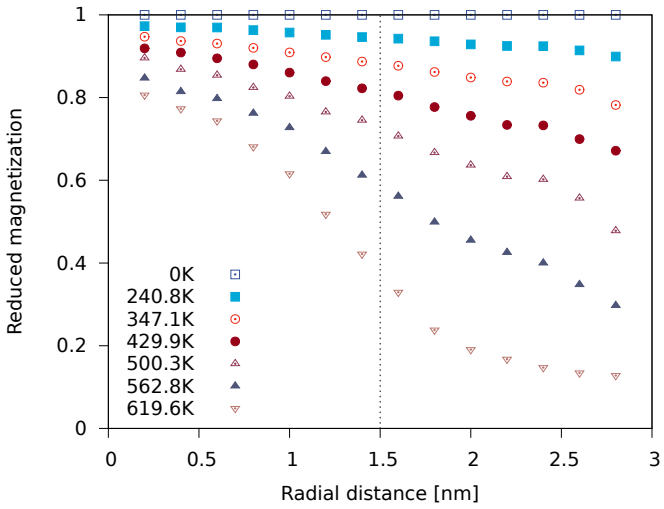

Figure 4.5: The calculated magnetisation as a function of radial distance from the particle centre for soft/hard core/shell nanoparticles for varying volume percentage of α-Fe. The particle considered here is a 6 nm diameter sphere with 3 nm core, so the core/shell interface is 1.5 nm from the centre, indicated in the figure by the dotted line. The drop in magnetisation between the core and the shell is predicted by figure 4.3, where, due to the lower Curie temperature and smaller α, for a given temperature the magnetisation is lower for smaller core volumes.

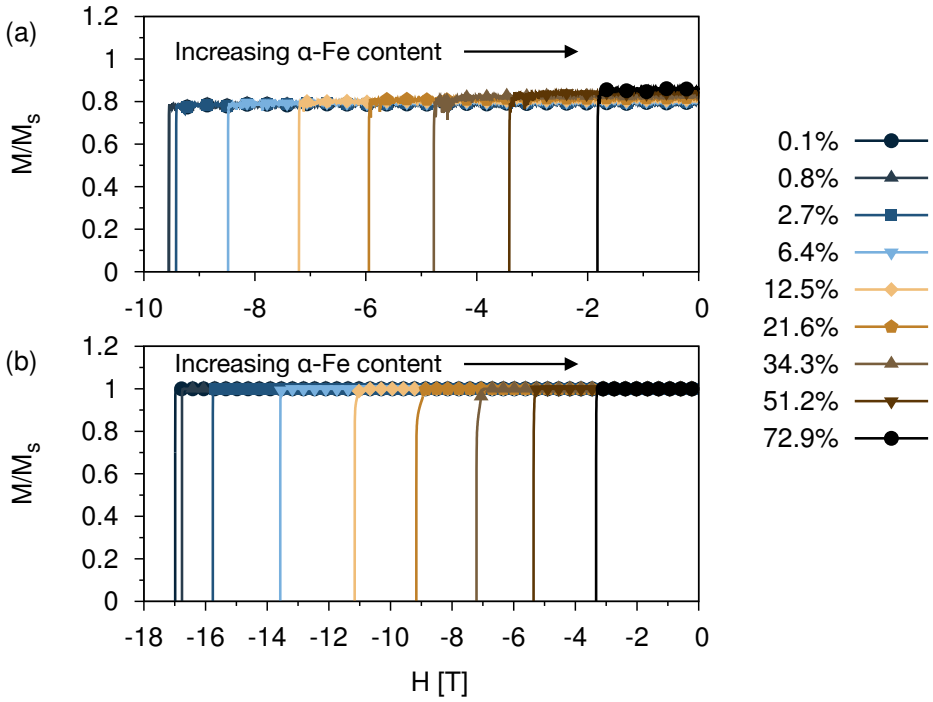

Figure 4.6: Calculated de-magnetisation curves for 12 nm diameter core/shell particles with varying vol% of α-Fe. (a) shows the variation of H_c for a system at 300 K and (b) at 0 K.

offset this reduction in terms of the maximum energy product. The addition of temperature to the system reduces the coercivity by virtue of increased spin fluctuations, which decrease the magnetocrystalline anisotropy. In both the zero temperature and finite temperature calculations the curves are normalised to the saturation magnetisation, however it can be seen that the spin fluctuations at finite temperature reduce the magnetisation to ~ 0.8 of the saturation.

The dependence of the coercive field of the nanoparticle on the fraction of α-Fe at zero temperature and room temperature is shown in Fig. 4.7. It can be seen that the coercive field decreases with increasing α-Fe fraction, with the most significant decrease seen at zero temperature.

The loss of performance of $Nd_2Fe_{14}B$ in automotive applications is due in part to the loss of saturation magnetisation at elevated operating temperatures. The polarisation effect means that the advantages of adding α-Fe, in addition to the reduction of the Nd requirement, are twofold. Firstly, the α-Fe enhances the overall magnetisation, giving rise to a potential increase in energy product (albeit offset by a reduction in coercivity). Secondly, the polarisation of the $Nd_2Fe_{14}B$ by the α-Fe stabilises the hard phase at elevated temperatures and thereby reduces the rate of reduction of the anisotropy.

An important indicator of the effectiveness of a permanent magnet in high-performance motor applications is the quantity $(BH)_{\max}$, or the maximum energy product, where BH is a scalar product between the induced magnetic flux density B and the internal magnetic field H. B is given by

$$B = \mu_0(M + H_{\text{int}}) \tag{4.2}$$

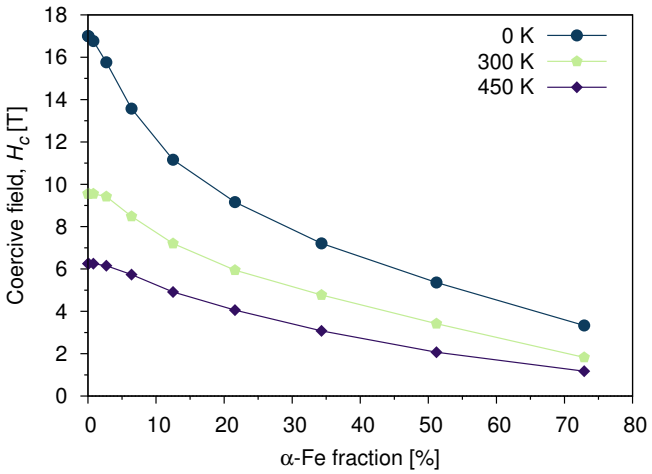

Figure 4.7: Calculated coercive field as a function of vol% of α-Fe at zero temperature, room temperature and the operating temperature of a permanent magnet motor.

where M is the magnetisation of the particle, and H_{int} the internal field which is given by

$$H_{\text{int}} = \mu_0 H_{\text{ext}} - \frac{\gamma}{4\pi} M \tag{4.3}$$

where $\mu_0 H_{\text{ext}}$ is the externally applied magnetic field, and γ is the demagnetising factor, taken to be $4\pi/3$ for a sphere [114]. In the calculation of the BH product we have assigned a composite magnetic moment to the particle, weighted according to the relative volumes of the two phases. In general, a larger magnitude of $(BH)_{\text{max}}$ is desirable.

The quantitative effects on the maximum energy product are shown in Figure 4.8. It is seen that, at finite temperatures, there is an optimal system composition at which the maximum energy product reaches a maximum. This is found to be $\sim$70%. After this point, a sharp drop in the maximum energy product is observed - a result of the decreasing thickness of the hard $Nd_2Fe_{14}B$ shell, which is the source of the high coercive field necessary to achieve a large energy product.

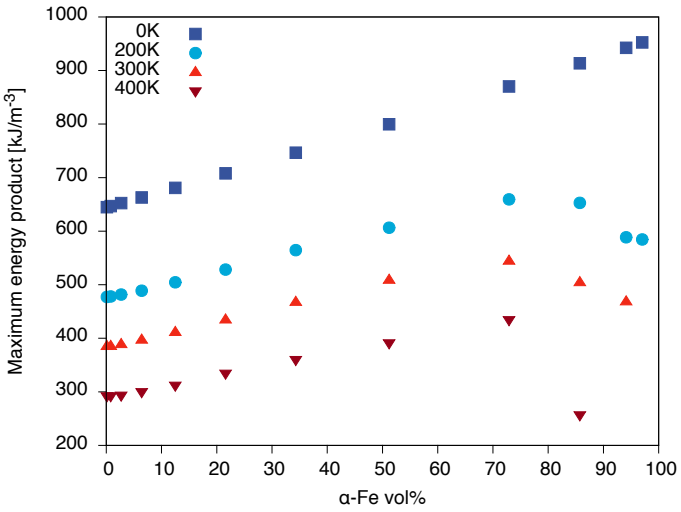

Figure 4.8: Calculated maximum energy product of composite 6 nm nanoparticle for a range of temperatures. The temperature labels here refer to the simulation temperature. At finite temperatures a steady increase is seen as a function of Fe core volume, which continues up to a threshold value of $\sim 70\%$, after which a rapid decline is seen. This suggests that for composite nanoparticles in general there is an ideal core size at which the maximum energy product may be optimised. At zero temperature there does not appear to be a threshold value.

4.4 Conclusion

Using a generic atomistic spin model, the hysteretic and thermodynamic properties of $Nd_2Fe_{14}B$ hard shell/α-Fe soft core nanostructures were investigated, with the aim of finding a structure with improved properties, namely improved magnetisation retention at elevated temperatures and larger maximum energy product BH_{max}.

We found an improvement in the total magnetisation of the composite system with increased α-Fe content. It was shown that this was a result of a deep-penetrating polarisation effect by the soft ferrite core on the hard shell. This enhancement however, was shown to be offset by a drop in coercivity with increasing Fe content, which reduced much more rapidly for larger particle sizes. Subsequently it was shown that the combination of these two effects resulted in an overall increase in the maximum energy product of the particle with increasing α-Fe content, up to a threshold value of $\sim$70%, after which it was found to decrease rapidly. Thus it has been shown that

in the future the performance of $Nd_2Fe_{14}B$ permanent magnets could potentially be optimised by the addition of α-Fe, up to a certain volume fraction, in the form of core/shell nanoparticles, provided the particle size is sufficiently small that polarisation across the interface between the core and the shell plays a significant role.

Chapter 5

Parameterisation of the full atomistic spin model

As our understanding of rare-earth intermetallics has progressed over the course of the last half-century, the evidence has become increasingly clear that their remarkable properties are largely a result of their intricate microstructure. This poses a problem when it comes to creating computational models that accurately describe their microscopic and macroscopic magnetic properties as the primary computational method used for probing these properties historically has been the so-called *micromagnetics* formalism, which works on length scales significantly larger than is required to probe microstructural phenomena.

The micromagnetics formalism relies on a continuum approximation, whereby the magnetisation of a material is assumed to be a continuous function of position [49]. Finding the minimum free energy with respect to the magnetisation then yields the equilibrium magnetic states of the structure. Using finite difference or finite element integration methods, these models are able to probe magnetic materials at length scales of several nanometres [49].

Particularly with materials such as $Nd_2Fe_{14}B$ and $NdFe_{12}$, it is known that many of their properties are a direct result of local crystal structure, i.e. structural effects on the scale of their respective unit cells which have dimensions on the scale of a few angstroms. Thus from this perspective, we are better served by an atomistic spin model. In this chapter we will investigate how we can go about parameterising these materials within the context of a classical atomistic spin model. For full details on the methods used in the model, please refer to section 2.1.

Models such as these are most often parameterised using a combination of *ab initio* methods, from which one can obtain atomistic parameters using knowledge of the electronic structure of the elements in question, and experimental measurement. An important point to make is that reliable first-principles calculations of rare-earth compounds are difficult to come by. The fact that many of the physical effects in which we are interested in rare-earth metallic compounds arise from the unpaired electrons in the $4f$ shell, which are notoriously difficult to treat from first-principles, requiring relativistic corrections. This is a difficult and specialised area. Thus the majority of the parameterisation of our spin model comes from experimental data.

5.1 $Nd_2Fe_{14}B$

5.1.1 Crystal structure

Figure 5.1 shows a visualisation of the complex $Nd_2Fe_{14}B$ crystal structure. The exact configuration of the unit cell was first established by Herbst et al. (1984) [115] using neutron powder-diffraction analysis, and later confirmed by a number of other groups using a combination of neutron powder-diffraction and x-ray-diffraction [25,116]. The atomic positions are well established, generally differing by less than 2 thousandths of an angstrom between works.

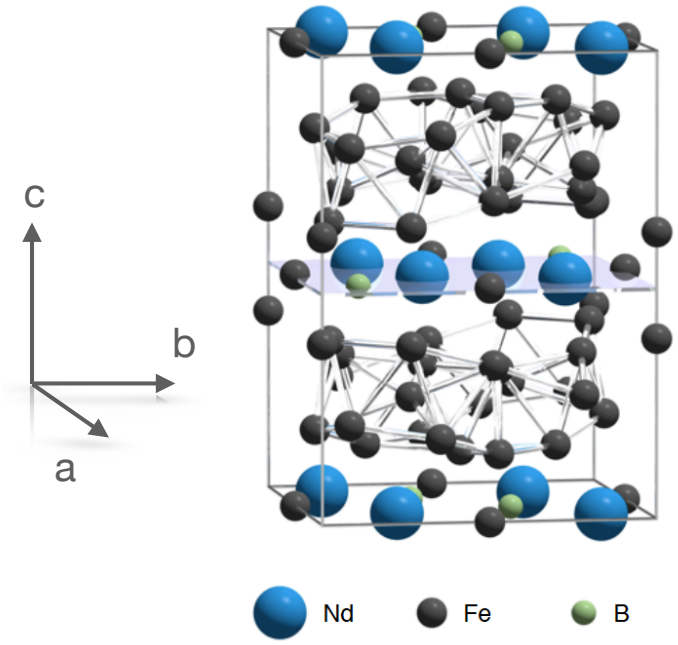

Figure 5.1: Schematic of the $Nd_2Fe_{14}B$ unit cell. The lattice symmetry is tetragonal and each unit cell contains 4 formula units.

The lattice constants of the unit cell at room-temperature were measured by Herbst et al. using neutron diffraction to be $a = 8.80$ Å (dimensions of basal plane) and $c = 12.19$ Å [115]. The unit cell lattice has tetragonal symmetry and the space group is $P4_2/mnm$. The Nd atoms occupy two crystallographically distinct symmetry sites, normally denoted by $4f$ and $4g$, while the Fe atoms occupy six cystallographically distinct symmetry sites, denoted by $16k_1$, $16k_2$, $8j_1$, $8j_2$, $4e$, and $4c$.

Taking the Wyckoff positions [117] of each atomic site from the literature, we apply the appropriate symmetry operations (determined using the Bilbao crystal server [118–120]) to obtain a full set of coordinates for the unit cell (see table 5.1).

All of the Nd and B atoms in the unit cell reside in the $z = 0$ and $z = 0.5$ planes, while all but 4 of the 56 Fe atoms sit in between these planes, forming two 'puckered nets' [22] symmetric about the $z = 0.5$ plane and rotated $\sim 30°$ with respect to one another.

Atom	x	y	z	Atom	x	y	z
Nd $4f$	0.268	0.268	0.000	Fe $16k_2$	0.860	0.463	0.324
Nd $4f$	0.732	0.732	0.000	Fe $16k_2$	0.140	0.537	0.324
Nd $4f$	0.232	0.768	0.500	Fe $16k_2$	0.537	0.140	0.676
Nd $4f$	0.768	0.232	0.500	Fe $16k_2$	0.463	0.860	0.676
Nd $4g$	0.140	0.860	0.000	Fe $16k_2$	0.640	0.963	0.176
Nd $4g$	0.860	0.140	0.000	Fe $16k_2$	0.360	0.037	0.176
Nd $4g$	0.640	0.640	0.500	Fe $8j_1$	0.098	0.098	0.204
Nd $4g$	0.360	0.360	0.500	Fe $8j_1$	0.902	0.902	0.204
Fe $16k_1$	0.223	0.567	0.127	Fe $8j_1$	0.402	0.598	0.704
Fe $16k_1$	0.777	0.433	0.127	Fe $8j_1$	0.598	0.402	0.704
Fe $16k_1$	0.933	0.723	0.627	Fe $8j_1$	0.402	0.598	0.296
Fe $16k_1$	0.277	0.067	0.627	Fe $8j_1$	0.598	0.402	0.296
Fe $16k_1$	0.277	0.067	0.373	Fe $8j_1$	0.098	0.098	0.796
Fe $16k_1$	0.723	0.933	0.373	Fe $8j_1$	0.902	0.902	0.796
Fe $16k_1$	0.567	0.223	0.873	Fe $8j_2$	0.317	0.317	0.246
Fe $16k_1$	0.433	0.777	0.873	Fe $8j_2$	0.683	0.683	0.246
Fe $16k_1$	0.777	0.433	0.873	Fe $8j_2$	0.183	0.817	0.746
Fe $16k_1$	0.223	0.567	0.873	Fe $8j_2$	0.817	0.183	0.746
Fe $16k_1$	0.067	0.277	0.373	Fe $8j_2$	0.183	0.817	0.254
Fe $16k_1$	0.933	0.723	0.373	Fe $8j_2$	0.817	0.183	0.254
Fe $16k_1$	0.723	0.933	0.627	Fe $8j_2$	0.317	0.317	0.754
Fe $16k_1$	0.277	0.067	0.627	Fe $8j_2$	0.683	0.683	0.754
Fe $16k_1$	0.433	0.777	0.127	Fe $4e$	0.500	0.500	0.114
Fe $16k_1$	0.567	0.223	0.127	Fe $4e$	0.000	0.000	0.614
Fe $16k_2$	0.037	0.360	0.176	Fe $4e$	0.000	0.000	0.386
Fe $16k_2$	0.963	0.640	0.176	Fe $4e$	0.500	0.500	0.886
Fe $16k_2$	0.140	0.537	0.676	Fe $4c$	0.000	0.500	0.000
Fe $16k_2$	0.860	0.463	0.676	Fe $4c$	0.000	0.500	0.500
Fe $16k_2$	0.463	0.860	0.324	Fe $4c$	0.500	0.000	0.500
Fe $16k_2$	0.537	0.140	0.324	Fe $4c$	0.500	0.000	0.000
Fe $16k_2$	0.360	0.037	0.824	B $4g$	0.371	0.629	0.000
Fe $16k_2$	0.640	0.963	0.824	B $4g$	0.629	0.371	0.000
Fe $16k_2$	0.963	0.640	0.824	B $4g$	0.871	0.871	0.500
Fe $16k_2$	0.037	0.360	0.824	B $4g$	0.129	0.129	0.500

Table 5.1: Fractional coordinates of atomic sites of $Nd_2Fe_{14}B$ unit cell.

As discussed in section 2.1, a zero-temperature magnetic moment is assigned to each atomic spin in the system. These vary between elements as well as between symmetry sites [22], with B atoms assumed to have zero magnetic moment. The estimated magnetic moment per Fe atom is estimated from the measured zero-temperature magnetisations of $R_2Fe_{14}B$ compounds where R is some non-magnetic rare-earth element. In these compounds the sole contribution to the total magnetic moment is assumed to come from the Fe sublattice. All experiments indicate that the Fe sublattice is ferromagnetically coupled and collinear [22], thus the moment per atom can simply be calculated by dividing the total moment of a $R_2Fe_{14}B$ crystal with non-magnetic R by the number of Fe atoms. Taking, for example, $Y_2Fe_{14}B$ which at 4 K has magnetisation $\sim 31.1\ \mu_B$ per formula unit [18, 121], we can estimate that the average moment per Fe atom is $\sim 2.2\ \mu_B$. While there will be some variation between each of the Fe symmetry groups, we assume the variation to be small, and so assign the same moment to all Fe atoms.

Similarly, one can determine the magnetic moment per Nd atom by simply subtracting the total magnetisation per unit volume of a $Y_2Fe_{14}B$ crystal from that of a $Nd_2Fe_{14}B$ crystal, leaving only the contribution of the Nd sublattice to the total magnetisation. The magnetisation of a $Nd_2Fe_{14}B$ single crystal has been measured at 4.2 K to be $\sim 37.2\ \mu_B$, from which we deduce that the average moment per Nd atom is $3.2\ \mu_B$.

5.1.2 Exchange interactions

From the atomistic spin Hamiltonian $\mathcal{H}$ discussed in section 2.1, the terms that appear due to contributions from the exchange interaction are $-\sum_{i,\delta} J_{\mathrm{NdFe}} \boldsymbol{S}_i \cdot \boldsymbol{S}_\delta$ and $-\sum_{\nu,j} J_{\mathrm{FeNd}} \boldsymbol{S}_\nu \cdot \boldsymbol{S}_j$, which are the inter-sublattice exchange interaction energy contributions, and $-\sum_{\nu,\delta} J_{\mathrm{Fe}}(\boldsymbol{r}) \boldsymbol{S}_\nu \cdot \boldsymbol{S}_\delta$, the intra-sublattice exchange interaction energy contribution of the Fe sublattice. Here $\boldsymbol{S}$ are the unit vectors giving the direction

of the magnetic moments at each site, the indices i, j label Nd sites, and ν, δ label Fe . The terms that need be parameterised are the quantities J_{NdFe} (this is equal to J_{FeNd}) and $J_{\mathrm{Fe}}(r)$. Note that exchange between rare-earth atoms is assumed to be sufficiently small that we may neglect it.

As mentioned previously, without detailed *ab-initio* information about the exchange interactions in $Nd_2Fe_{14}B$ it is difficult to speak definitively as to the form these should take. It is known however that they are relatively long ranged and depend strongly on inter-atomic separation [22]. As a starting point we can use information about the exchange interaction between Fe sites in BCC Fe. These were calculated from first principles by Pajda et al. [122] using density functional theory (DFT). To these data we fit a function of the form

$$J_{\mathrm{Fe}}(r) = J_0 + J_r \exp(-r/r_0) \tag{5.1}$$

where r is the separation between ions, r_0 is a characteristic separation, and J_0 and J_r are fitting constants. For interatomic separations greater than 5.0 Å the exchange energy is truncated to zero. The function is shown in Fig. 5.2. Implementing the fitted function into the model as-is gives a simulated Curie temperature (T_{c}) of approximately 800 K, which is higher than the experimentally found T_{c} for $Nd_2Fe_{14}B$ of 585 K. Taking into account the lower density of $Nd_2Fe_{14}B$ in comparison with BCC Fe, it is reasonable to expect that there will be reduced overlap of Fe orbitals, and a corresponding reduction in the exchange interaction energies. Therefore to account for this we scale the function via the pre-factor J_r until the T_{c} aligns with the experimental value. The scaled function is shown in Fig. 5.2. While this scaling is not as physically sound as we might like, it has the advantage of preserving the long-range and distance dependent characteristics of the *ab-initio* data.

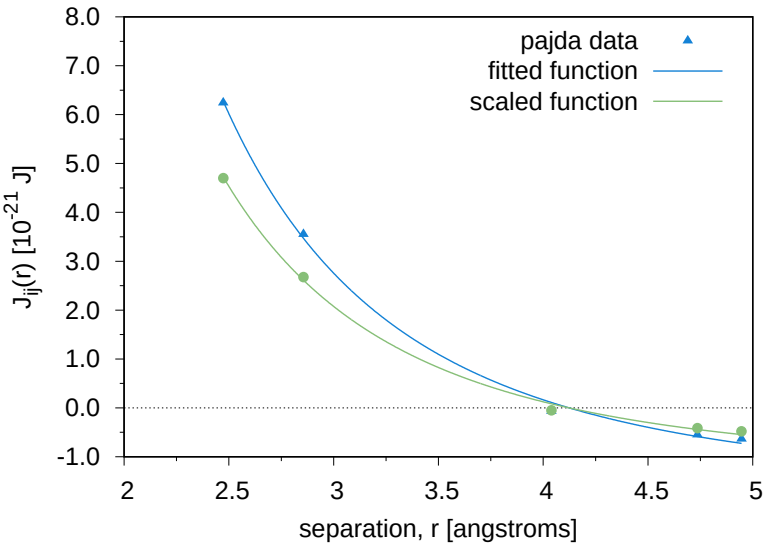

Figure 5.2: The exchange energy as a function of inter-atomic separation for interactions between Fe moments in the $Nd_2Fe_{14}B$ spin model. The triangular points (taken from Ref. 5.2) are the exchange interaction energies in α-Fe calculated from first principles. Using these in the $Nd_2Fe_{14}B$ model results in a too-high T_c, thus the points are scaled by a pre-factor of 0.753, shown by the green curve with circular points.

The interactions between Nd and Fe ions in $Nd_2Fe_{14}B$ are rather complex. The vast majority of previous theoretical investigations of $Nd_2Fe_{14}B$ are based on the so-called *mean-field* approximation, wherein the effect of all of the other spins on the rare-earth moment is approximated to a single average effect, greatly reducing the complexity of the problem. In our model we seek to break this approximation down into pairwise interactions.

Simplistically, from the positive sign of the Nd moment we can infer that the coupling between Nd and Fe moments is ferromagnetic. In our model, for simplicity, we assume a direct ferromagnetic coupling between these moments, though it has been suggested [123–125] that the $4f$ electrons of the Nd ion induce a local $5d$ moment, and it is the $5d$ moment which interacts with the neighbouring $3d$ moments, aligning with the picture that the $4f$ moments are strongly shielded from the environment and do not interact directly with it. From experiment, a high degree of ordering is observed between Nd and Fe moments at room temperature - a significant fraction

of T_c, suggesting a relatively strong exchange interaction. We treat J_{NdFe} as a free parameter for fitting to experiment. For Nd-Fe interactions in $Nd_2Fe_{14}B$ the nearest neighbour distance is, compared to the Fe-Fe interactions, reasonably well-defined, with each Nd atom having a coordination number of 16, thus we choose a cut-off radius of 4 Å, and assign all interactions within this radius the same interaction strength.

5.1.3 Magnetocrystalline anisotropy

A defining quality of $Nd_2Fe_{14}B$ is its large anisotropy field H_a - at zero-temperature the coercivity is estimated to be ~ 17 T [22]. Macroscopically the magnetocrystalline anisotropy energy can be expressed by [126]

$$E_K = K_1 \sin^2\theta + K_2 \sin^4\theta \tag{5.2}$$

where K_1 and K_2 are effective anisotropy constants which can be determined by experiment. This relation is the preferential expression for interpreting experimental data as the straightforward link between anisotropy constants and angular dependence makes it easy to find the constants from measurements of the torque.

Nd sublattice anisotropy

In the case of a material with a single sublattice, the on-site anisotropy could be extracted from the anisotropy field H_a in a straightforward manner via the relation $H_a = 2k_u/\mu_s$ [48]. This expression does not apply to $Nd_2Fe_{14}B$, in which the sublattice contributions to the magnetocrystalline anisotropy are unevenly distributed, thus a new expression must be derived. Using a Stoner-Wohlfarth-like approach, a single domain Nd particle is considered with second and fourth order uniaxial anisotropy

constants k_2 and k_4, and energy E given by the expression

$$E = -k_2 m_z^2 - k_4 m_z^4 + m_z \mu H \tag{5.3}$$

where m_z is the z-component of the reduced magnetisation, μ is the magnetic moment, and H is the applied field strength. Expansion of the Legendre polynomials gives the anisotropy energy E of a Nd atom at 0 K thus:

$$E = -\frac{k_2^{\mathrm{Nd}}}{3}(3S_z^2 - 1) - \frac{k_4^{\mathrm{Nd}}}{12}(35S_z^4 - 30S_z^2 + 3) \tag{5.4}$$

where the S_z are the z-components of the unit spin vector at each Nd site (as usual the z-direction is defined as lying parallel to the c-axis). There are two experimental observations that can help elucidate the ratio of k_2 to k_4:

1. $Nd_2Fe_{14}B$ undergoes a spin-reorientation transition (SRT) at T_s ($T_\mathrm{s} = 135$ K). For $T < T_\mathrm{s}$, the rare-earth moment cants 30° from the c-axis, taking on an easy-cone rather than uniaxial anisotropy, while above T_s the Nd sublattice takes on a uniaxial c-axis anisotropy.

2. $Nd_2Fe_{14}B$ possesses a significantly larger anisotropy than $Y_2Fe_{14}B$, in which the R sublattice carries no moment.

Thus it can be asserted that the Nd sublattice has uniaxial anisotropy above T_s, and that the anisotropy term giving rise to the low temperature moment canting has a stronger temperature dependence than the term responsible for the perpendicular component of the anisotropy. From Callen and Callen [127] we expect that the effective anisotropies should go as $k_2^{\mathrm{eff}}(T) \sim m_{\mathrm{Nd}}(T)^3$ and $k_4^{\mathrm{eff}}(T) \sim m_{\mathrm{Nd}}(T)^{10}$, where $m_{\mathrm{Nd}}(T)$ is the Nd sublattice reduced temperature-dependent magnetisation normalised to $m_{\mathrm{Nd}}(0)$. Given that the temperature dependence of the fourth order term is so much stronger than that of the second order term, it can be educed that

it is the fourth order term that is responsible for the low temperature spin canting, or the *in-plane* contribution (corresponding to a negative value for the effective anisotropy), and the second order term responsible for the less temperature dependent out-of-plane anisotropy. The second observation tells us that the Nd sublattice contributes strongly to the anisotropy at $T > T_{\mathrm{s}}$, and therefore should be non-zero and positive [128].

To calculate the ratio of the k_2 constant to k_4 given a canting angle, we must differentiate with respect to S_z, giving

$$\frac{dE}{dS_z} = -2k_2^{\mathrm{Nd}} S_z - \frac{140k_4^{\mathrm{Nd}}}{12} S_z^3 + \frac{60k_4^{\mathrm{Nd}}}{12} S_z. \tag{5.5}$$

Letting $dE/dS_z = 0$ gives the saddle point in the energy surface which is determined by the canting angle θ. Rearranging, the canting angle is then given by

$$z \equiv \cos\theta = \sqrt{\frac{3}{7} - \frac{6}{35}\frac{k_2^{\mathrm{Nd}}}{k_4^{\mathrm{Nd}}}}. \tag{5.6}$$

Solving for the ratio $k_2^{\mathrm{Nd}}/k_4^{\mathrm{Nd}}$, we have

$$\frac{k_2^{\mathrm{Nd}}}{k_4^{\mathrm{Nd}}} = -\frac{35}{6}\left(\cos^2\theta - \frac{3}{7}\right) \tag{5.7}$$

Substituting in the canting angle for θ we get that

$$\frac{k_2^{\mathrm{Nd}}}{k_4^{\mathrm{Nd}}} = -\frac{15}{8} \tag{5.8}$$

Thus, for a given anisotropy field, the Nd anisotropy constant is higher than one would expect and cannot be determined by a simple averaging of the anisotropy between the Fe and Nd sublattices. The final value of k_2^{Nd} is determined graphically by solving the angle dependent energy with effective k_2^{Nd} including the effect of the

Fe sublattice, yielding final constants $k_2^{\mathrm{Nd}} = 4.359 \times 10^{-21}$ J/atom and $k_4^{\mathrm{Nd}} = -2.32 \times 10^{-21}$ J/atom. These anisotropy constants are approximately one tenth the magnitude of the exchange interaction energy, which allows for the possibility of non-collinear magnetisation states induced by the anisotropy. We note that the determined values are similar to those determined from crystal field theory [22, 129].

Fe sublattice anisotropy

It is known that the Fe sublattice contributes to the magnetocrystalline anisotropy, as $R_2Fe_{14}B$ compounds with non-magnetic R (e.g. R=La, Ce, Lu, Y, Th), in which the anisotropy is generated by the Fe sublattice alone, have appreciable anisotropy energies (e.g. $K_1 = 1.2$ MJ/m^3 for $Lu_2Fe_{14}B$), likely due to the complex arrangement of atoms in the Fe sublattice. Using the Stoner-Wohlfarth relation $k_2 = H_k \mu_s / 2$ [130] the zero temperature second order uniaxial anisotropy constant is calculated to be $k_2 = 1.836 \times 10^{-23}$ J/atom.

5.1.4 Hysteresis behaviour

Having obtained a full set of parameters for $Nd_2Fe_{14}B$, a series of simulations were run to confirm that the calculated macroscopic properties align with experimentally found macroscopic values. We begin with the hysteresis behaviour of the material. The simulation is set up as follows. An 8 x 8 x 8 nm system with periodic boundary conditions was chosen, large enough to mitigate any finite size effects and to accurately simulate a bulk system. An external field is applied along the *c*-axis, with the system set to equilibrate at each field step for 10,000 time steps, and the magnetisation averaged at that field step for a further 50,000 time steps, at a time step of 1 fs. The field strength increment was set to 0.05 T. This equates to a field sweep rate of 1e9 Ts^{-1}.

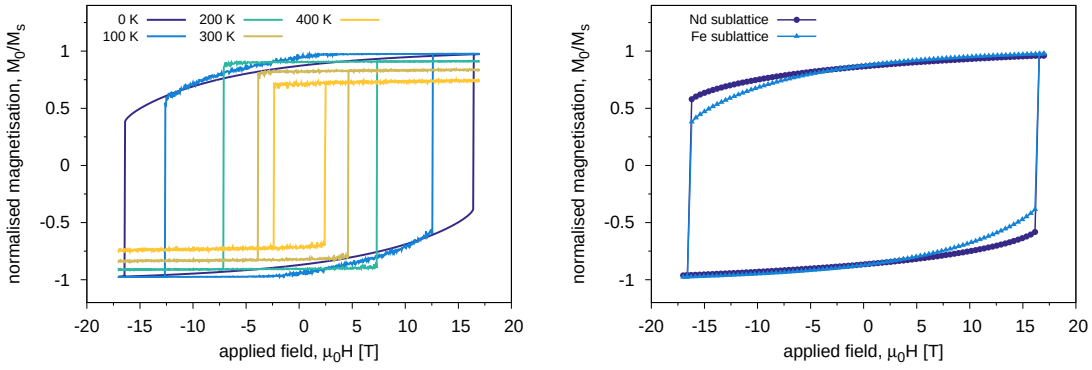

(a) (b)

Figure 5.3: (a) shows calculated hysteresis loops for temperatures between 0 and 400 K. Previous theoretical predictions for the zero temperature coercivity predict 17 T, in good agreement with our calculation. Below 200 K there is a distinct non-square shape, indicating non-collinear spin states which arise due to competition between second and fourth order anisotropy terms. (b) shows the simulated hysteresis at 0 K resolved by sublattice. It can be seen that the sublattices deviate as the higher Fe moment interacts more strongly with the external field, and so begins to demagnetise at lower field.

As mentioned previously, the zero temperature coercive field of $Nd_2Fe_{14}B$ is is estimated to be very high, approximately 17 T [22]. In Fig. 5.3a it can be seen that the zero temperature calculated switching field matches very closely the estimated value for the coercivity. The non-square shape of the loop at low temperatures comes about as a result of the canting of the Nd sublattice away from the *c*-axis. It is interesting to note that unlike previous theoretical approaches, the non-collinear alignment of the sublattices comes about purely as a result of competing magnetocrystalline anisotropy energy terms rather than any kind of alignment being imposed by the model. The distinct behaviours of the individual sublattices can be seen clearly in Fig. 5.3b, which shows the magnetisation of the Nd and Fe sublattices separately. It can be seen that the higher moment of the Fe sublattice results in a stronger coupling to the external field, and thus the Fe loses its magnetisation sooner than the Nd sublattice, resulting in a non-collinear equilibrium state at high fields.

The strong temperature dependence of the fourth order uniaxial anisotropy term, responsible for the canting at low temperatures, means that as the temperature is increased past T_{s}, the shape of the hysteresis curve becomes square. This is a result of the fact that the Nd sublattice anisotropy is now dominated by the k_2 term, acquiring out-of-plane anisotropy. For $T > T_{\mathrm{s}}$ the large anisotropy of the Nd sublattice holds the Fe sublattice in place, hence the flatness of the magnetisation up to H_{c}, before the system succumbs and undergoes a coherent switch.

5.1.5 Temperature dependence of M_{s}

Here we investigate the finite temperature behaviour of the magnetisation in our $Nd_2Fe_{14}B$ spin model. To mitigate finite size effects, we again choose a system with dimensions 8 x 8 x 8 nm. To get closer to simulating a bulk system we utilise periodic boundary conditions, nullifying any surface effects. Because we are simulating an equilibrium property of the system, the system is integrated using a Monte Carlo algorithm for efficiency. At each temperature step the system is equilibrated for 10,000 steps, before being integrated for a further 50,000 steps to obtain an average magnetisation.

The magnetisation of the entire system as well as of each sublattice are shown in Fig. 5.4. For comparison, the total magnetisation as a function of temperature is shown, as measured by Hirosawa et al. [18] using a vibrating sample magnetometer (VSM). Qualitatively the calculated magnetisation matches experiment reasonably well, though it is a little lower across the whole temperature range. It should be noted however that the calculated curve actually matches values for T_{c} ($\sim$ 585 K) better than the experimental data seems to. This may be due to the fact that the magnetisation measurements using the VSM were made in the presence of a small applied magnetic field, sustaining the magnetisation to higher temperatures.

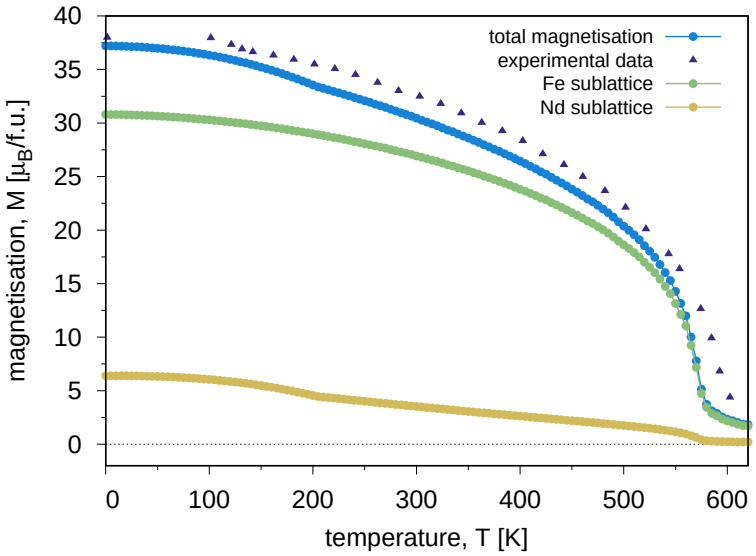

Figure 5.4: Calculated temperature dependence of the individual sublattices as well as the total magnetisation are shown for a $Nd_2Fe_{14}B$ single crystal. Experimental data taken from Ref. [18] is shown for comparison. The calculated T_c matches the expected T_c of 585 K reasonably well. The bulk of the magnetisation originates from the Fe sublattice due to the stoichiometric abundance of Fe in the crystal.

It can be seen that the bulk of the magnetisation originates from the Fe sublattice as expected, with the contribution of the Nd sublattice only 17% of the total magnetisation at zero temperature, a result of the stoichiometric abundance of Fe in the crystal. Above approximately 200 K the Nd sublattice magnetisation approaches a near linear dependence with temperature, important due to the fact that the Nd provides the bulk of the magnetocrystalline anisotropy. This may offer an explanation as to why there is a significant reduction in the coercivity of $Nd_2Fe_{14}B$ at elevated temperatures.

5.2 $NdFe_{12}$

As discussed previously, the hard magnetic phase $Nd_2Fe_{14}B$ currently holds the position of the world's strongest permanent magnet, with a $\mu_0 M_s$ of 1.6 T and a $\mu_0 H_A$ of 7.5 T at room temperature [131, 132]. One of the primary weaknesses however is

its relatively low T_c of 585 K and a strong temperature dependence of the coercivity. This is where the RFe_{12} family of compounds comes in. Historically this group have been thought to be stable only in ternary forms, that is, with some Fe atoms substituted by a third, phase-stabilising element M (e.g. Ti, V, Cr, Mn, Mo, W, Al or Si) [133, 134], leading to a reduction in the overall magnetisation.

Using first-principles calculations, Miyake et al. [46] showed that if the compound could be stabilised without a third element M, with nitriding, $NdFe_{12}N_x$ would have large magnetisation as well as strong magnetocrystalline anisotropy. Very recently, Hirayama et al. [36,37] claimed to have synthesised, for the first time, an $NdFe_{12}$ film via heteroepitaxial growth on top of a tungsten under-layer which has similar lattice parameters. Upon nitriding, the film was measured to have $\mu_0 M_s \approx 1.66$ T, $\mu_0 H_A \approx 8$ T, and a T_c of ~ 823 K, all of which are superior to $Nd_2Fe_{14}B$. DFT calculations by Miyake et al. [46] suggest that the primary effect of the N, which sits interstitially between Nd atoms in the c-direction, is to redistribute the charge around the Nd atom such that the Nd-5d electrons are pulled to the c-axis, resulting in the crystal field parameter $A_{20}\langle r^2 \rangle$ changing from negative to positive, and the anisotropy changing from in-plane to out-of-plane.

5.2.1 Crystal structure

Fig. 5.5 shows the crystal atomic structure of $NdFe_{12}$. The crystal lattice is body-centred tetragonal (BCT) and the space group is $I4/mmm$. The phase belongs to a family of compounds that have a so-called $ThMn_{12}$ structure, the atomic arrangement of which is well documented. The lattice parameters of the unit cell were calculated using molecular dynamics by our collaborators in Hrkac's group at the University of Exeter, to be $a = 8.512$, and $c = 4.842$, using molecular dynamics simulation with parameterised forced fields. These compare well with values given by Miyake

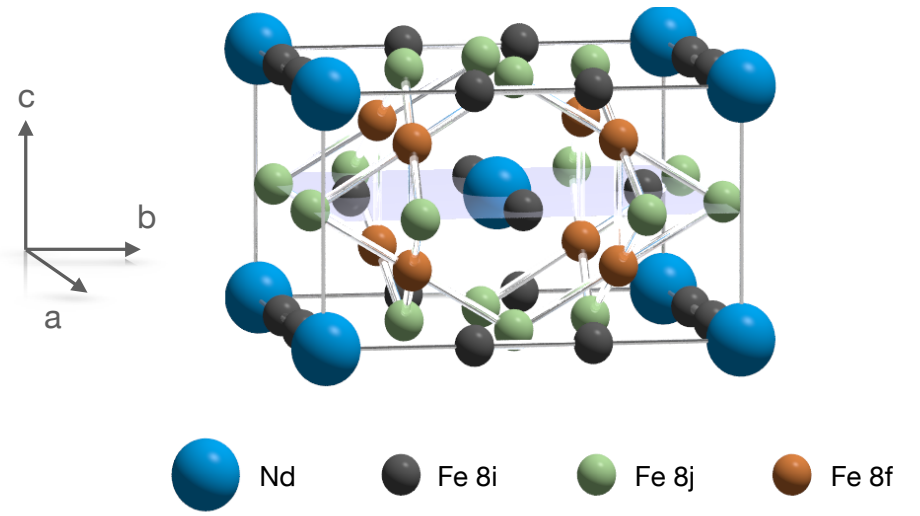

Figure 5.5: Visualisation of the $NdFe_{12}$ unit cell. The unit cell contains 26 atoms (2 formula units): 2 Nd atoms and 3 groups of 4 Fe atoms belonging to symmetry groups $8i$, $8j$, and $8f$.

et al. [46], which differ by 0.7% and 1.3% for a and c respectively. The fractional coordinates of each atom in the unit cell are given in table 5.2.

The $NdFe_{12}$ unit cell contains 26 atoms, or two formula units. The Fe sites are split into three crystallographically distinct symmetry groups, denoted by: $8i$, $8j$, and $8f$, each of which contains four atoms. The atoms of each symmetry group possess a different moment. These were calculated by Miyake et al. [46] from first-principles using DFT within the generalised gradient approximation. The $8f$ moments have a magnetic moment of 2.14 μ_B, the $8i$ 2.67 μ_B and the $8j$ 2.51 μ_B. These are ferromagnetically aligned and give a total Fe sublattice magnetisation of 29.28 μ_B per formula unit. The large positive moment of the Fe sublattice compensates the contribution of the Nd f electrons which contribute a negative moment in the absence of nitrogen of -3 μ_B [46].

Atom	x	y	z	Atom	x	y	z
Nd	0.000	0.000	0.000	Nd	0.500	0.500	0.500
Fe 8i	0.357	0.000	0.000	Fe 8i	0.857	0.500	0.500
Fe 8i	0.000	0.357	0.000	Fe 8i	0.500	0.857	0.500
Fe 8i	0.643	0.000	0.000	Fe 8i	0.143	0.500	0.500
Fe 8i	0.000	0.643	0.000	Fe 8i	0.500	0.143	0.500
Fe 8j	0.273	0.500	0.000	Fe 8j	0.773	0.000	0.500
Fe 8j	0.500	0.273	0.000	Fe 8j	0.000	0.773	0.500
Fe 8j	0.250	0.750	0.250	Fe 8j	0.250	0.750	0.750
Fe 8j	0.727	0.500	0.000	Fe 8j	0.227	0.000	0.500
Fe 8f	0.500	0.727	0.000	Fe 8f	0.000	0.227	0.500
Fe 8f	0.250	0.250	0.250	Fe 8f	0.250	0.250	0.750
Fe 8f	0.750	0.250	0.250	Fe 8f	0.750	0.250	0.750
Fe 8f	0.750	0.750	0.250	Fe 8f	0.750	0.750	0.750

Table 5.2: Fractional coordinates of atomic sites of $NdFe_{12}$ unit cell.

5.2.2 Exchange interactions

The exchange interactions, as before, can be divided into two types: the Fe-Fe exchange, and the Nd-Fe inter-sublattice coupling. The latter is of particular importance as it gives some insight into the reversal mechanisms of the material. A strong inter-sublattice coupling is desirable as in this scenario the strong magnetocrystalline anisotropy of the Nd sublattice will help to stabilise the Fe sublattice.

Given that the exchange interaction is the key parameter in determining the Curie temperature, we use the T_c as a fixing parameter of sorts, and fit the exchange values until the T_c matches the expected value. As $NdFe_{12}$ is a relatively recent and unstudied material, experimental measurements of the macroscopic parameters are few. $Nd(Fe,M)_{12}$ compounds however, have been extensively investigated in the literature, thus we may extrapolate from these data to determine the T_c of $NdFe_{12}$. Extrapolating linearly using data for $NdFe_{1-x}Mo_x$ measured by Buschow and de Mooij [135] gives a Curie temperature of 598 K for $x = 0$, while a similar extrapolation for $M =$

Ti [135–137] gives $T_c = 595.5$ for zero Ti content, thus we proceed using an average value of $T_c = 597$ K for $NdFe_{12}$.

Regarding the form of the exchange, the situation is similar to the case for $Nd_2Fe_{14}B$. For the Fe-Fe exchange interaction we assume a separation dependent and long-range form similar to that observed in bulk BCC Fe, following (5.1). As before we use *ab-initio* data from Ref. [122] as a primary point of contact and scale as required. For simplicity, the same form and magnitude of the exchange is assumed between the sites of each of the Fe symmetry groups. In reality these may differ slightly due to the variation in moments of each symmetry group, however the variation is assumed to be negligible here.

For the inter-sublattice exchange between Nd and Fe sites, the neighbour configuration was calculated to analyse the relative proximities. As there is only one Nd sublattice symmetry group, the neighbour configuration for both Nd atoms in the unit cell will be identical. From Fig. 5.6 it can be seen that there is a cluster of neighbours within 3.25 Å of the Nd atom, and that the first two shells are particularly close together. The first shell consists of $8i$ sites exclusively, while the second shell contains $8j$ sites, with 0.06 Å between the two shells. The shortest distance between two neighbouring rare-earth atoms in the crystal is 6.49 Å. Given the prior assumption that the separation between rare-earth atoms is sufficiently great that R-R interactions may be neglected, we can infer that the influence of a rare-earth atom can extend no more than half of 6.49 Å (at least not in a significant way). That is not to say anything about the range of influence of the Fe atoms, which are assumed to be long-ranged in our model (based on the calculations by Pajda et al. [122]), however considering the Fe atomic distribution about the Nd sites, it seems sensible to truncate the inter-sublattice exchange interaction to somewhere in between the first two clusters of neighbours, e.g. 3.5 Å.

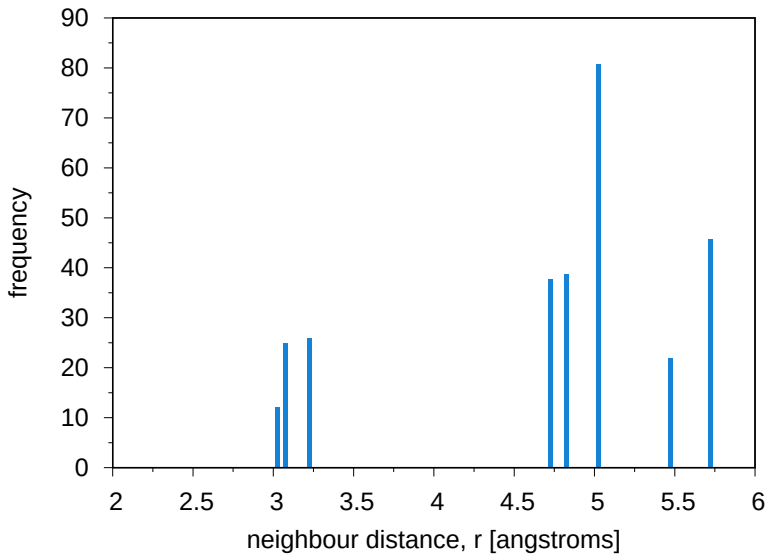

Figure 5.6: Frequency of transition-metal neighbours as a function of distance from rare-earth atoms in $NdFe_{12}$.

We proceed by running a parameter scan across these two degrees of freedom, treating both the R-Fe and Fe-Fe exchange parameters as free parameters. For each pair of parameters a Curie temperature simulation was carried out using the Monte Carlo integration scheme discussed in section 2.1. The parameter scans were run for three systems, one with nearest-neighbour R-Fe interactions, another with next-nearest-neighbour R-Fe interactions and a third with three shells of Fe neighbours around the rare-earth atom. The value of T_c for each simulation is found by fitting the expression

$$m(T) = \left[1 - \left(\frac{T}{T_c}\right)\right]^{\beta} \tag{5.9}$$

for the temperature dependence of the reduced magnetisation of a system m. The expression is derived from an empirical interpolation between critical behaviour and the Bloch law, which describes low temperature behaviour [138]. Here β is known as the critical exponent.

The results of the parameter scans are shown in Fig. 5.7. It can be seen that in the first scan, for which only nearest-neighbour exchange is considered in the case of R-Fe

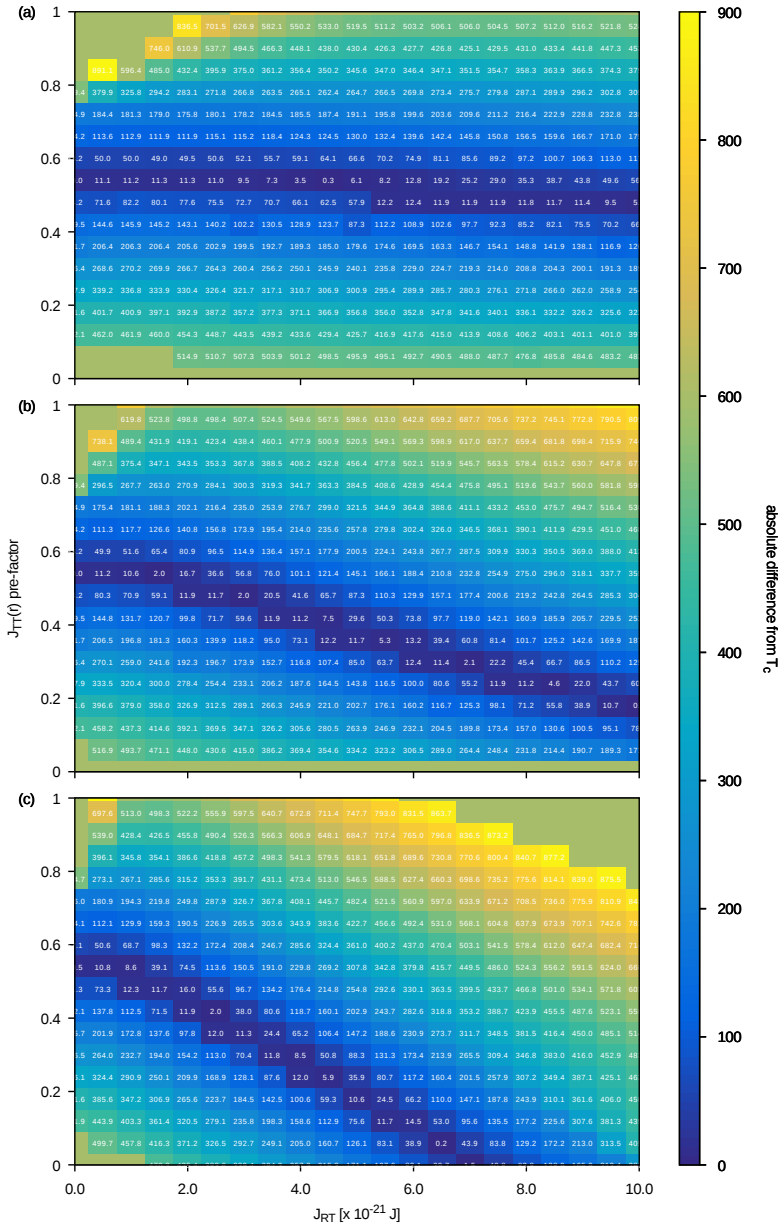

Figure 5.7: Parameter scans for $NdFe_{12}$ exchange interaction energies. The vertical axis represents the J_{TT} pre-factor which multiplies the *ab-initio* calculated function for the exchange energy between Fe atoms, while the horizontal axis represents an exchange interaction constant for interactions between Nd and Fe atoms. The colour bar indicates the absolute difference between the T_c calculated using each given pair of parameters and the expected T_c for $NdFe_{12}$ of 597 K. (a) shows the results of simulations carried out using nearest-neighbours only for rare-earth-Fe interactions, (b) interactions between rare-earth atoms and 2 shells of neighbours, and (c) 3 shells.

interactions (Fig. 5.7a) there is very little dependence of the Curie temperature on the magnitude of the R-Fe exchange, and that the band of viable exchange parameters exists at around $y = 0.55$, that is to say, where the pre-factor that multiplies the BCC Fe *ab initio* exchange function is ~ 0.55. Here, two important points can be distilled:

1. for the case where only nearest-neighbours are considered for R-Fe interactions, the coordination number of the rare-earth atoms is sufficiently low that the ordering of the system is dominated by the Fe-Fe exchange;

2. and that even when the system order is reliant solely upon the Fe-Fe exchange, a weaker Fe-Fe exchange interaction energy than that calculated for BCC Fe and that used for $Nd_2Fe_{14}B$ in section 5.1 is required to attain the experimentally observed T_c in $NdFe_{12}$, despite the fact that the T_c for $NdFe_{12}$ is greater than that for $Nd_2Fe_{14}B$, if only marginally.

The second fact is significant because, as there is negligible contribution from the R-Fe exchange in this case, this band of viable exchange parameters can be considered an upper bound on the Fe-Fe exchange strength. One explanation for why the exchange interaction strength is lower despite there being a higher T_c in $NdFe_{12}$, is the greater density of Fe atoms in $NdFe_{12}$ (0.068 $Å^{-3}$) compared with $Nd_2Fe_{14}B$ (0.059 $Å^{-3}$). In general we can assume that this behaviour is not physical as it is understood that the rare-earth-Fe exchange does indeed play role, and in fact changes the temperature dependence substantially

In the second case, where two neighbour shells are considered (Fig. 5.7b), it can be seen that there is a substantial shift in the system behaviour. There is in this case a strong dependence on the parameter J_{RT} that emerges. With the introduction of an extra shell, the number of R-Fe interactions increases by 200%, thus the role played by J_{RT} becomes much more significant. Here it becomes clear that it is the total exchange energy in the system that is important, and that as one increases the exchange energy

between rare-earth and Fe atoms, the amount of exchange energy between Fe atoms required to attain the experimental T_c is reduced. For the case where the $8f$ shell of neighbours is considered (Fig. 5.7c), an even stronger dependence of the Curie temperature on J_{RT} is seen. In this instance, for $J_{RT} \approx 7.0$, the inter-sublattice coupling becomes sufficiently large that zero intra-sublattice coupling in the Fe is required for the system to exhibit the correct Curie temperature.

2 shells				3 shells			
J_{RT} (e-21 J)	J_{TT} pre-factor	T_c (K)	β	J_{RT} (e-21 J)	J_{TT} pre-factor	T_c	β
1.50	0.54	599.0	0.348	1.00	0.54	605.6	0.346
3.00	0.48	595.0	0.337	2.50	0.42	595.0	0.353
4.50	0.42	604.5	0.358	4.00	0.30	605.5	0.414
5.50	0.36	591.7	0.383	4.50	0.24	591.1	0.450
7.00	0.30	599.1	0.424	6.50	0.06	597.2	0.641
8.50	0.24	601.6	0.478	7.00	0.00	598.5	0.766
10.0	0.18	597.2	0.547				

Table 5.3: Parameter pairs extracted from Figs. 5.7b and 5.7c for which the calculated T_c is within 1.5% of the expected T_c. The J_{TT} pre-factor denotes the factor that multiplies the range dependent exchange interaction function discussed in section 5.1.2. The T_c and β values are determined via fitting of (5.9).

Given the bands of seemingly allowed parameters shown in Fig. 5.7, the challenge is to pinpoint where along these bands the correct pair of parameters lies. To this end we utilise as an additional constraint the critical exponent β in (5.9), which can tell us something about the form of the temperature dependence.

In table 5.3 are shown the points in the parameter space shown in Fig. 5.7 for the next-nearest-neighbour and next-next-nearest-neighbour cases (the nearest-neighbour case is assumed to negligible due to the independence of J_{RT}) which give a value for T_c within 1.5% of the experimental T_c. It can be seen that there is significant variation in β, particularly in the 3 shell case. For the parameterisation of $Nd_2Fe_{14}B$ in section 5.1 it was found that the β which gave best agreement with experiment was $\beta = 0.301$. In the absence of experimental data for $M(T)$ for $NdFe_{12}$ we assume the value of β to be

similar to that for $Nd_2Fe_{14}B$. Thus the parameters that fit best are J_{RT} = 3.00e-21 J and J_{TT} pre-factor = 0.48, which give a T_c of 595.0 and a critical exponent $\beta = 0.337$. Simulated using these parameters, the temperature dependence of M_s is shown in Fig. 5.8. The experimental data for $NdFe_{12}N_x$ is shown as well for comparison. It can be seen that the addition of N has a significant effect in increasing the T_c. Nitriding is also known to have the effect of increasing the total moment of RFe_{12} compounds. In Fig. 5.8 both curves are normalised to the zero temperature saturation magnetisation. It can be seen that the two curves have a very similar form at low temperature. At higher temperatures the $NdFe_{12}$ de-magnetises while the nitrided compound is more stable, exhibiting a T_c of $\sim$ 823 K.

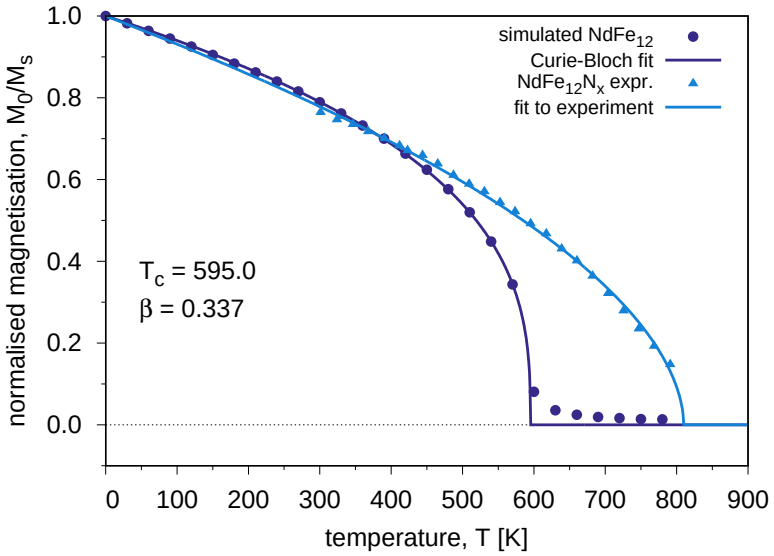

Figure 5.8: Calculated temperature dependence of M_s for $NdFe_{12}$ using parameters $J_{RT} = 3.00 \times 10^{21}$ for the inter-sublattice coupling, and J_{TT} pre-factor = 0.48, giving a T_c of 595.0 K with critical exponent $\beta = 0.337$. For comparison, the measured temperature dependence of $NdFe_{12}N_x$ is shown (Ref. [36]). It can be seen that the T_c for the latter compound is much higher, though both curves share the same form at lower temperatures.

5.2.3 Magnetocrystalline anisotropy

Nd sublattice

The magnetocrystalline anisotropy in the $NdFe_{12}$ crystal arises primarily from the rare-earth sites. The anisotropy of the Nd emerges as a result of a combination between interaction of the $4f$ shell with the crystal electric field (CEF) and strong spin-orbit coupling in the following manner. The CEF breaks the local spatial symmetry for the $4f$ shell, thus orienting the orbital moment of the rare-earth. This in turn gives the spin moment a preferential orientation via strong spin-orbit coupling, aligning the spin moment *anti-parallel* to the orbital moment in the case of Nd based compounds. Given this mechanism, one way of obtaining a measure of the magnetocrystalline anisotropy is by looking at the CEF parameters.

In the case of large anisotropy energies, i.e. in hard materials, the second order uniaxial anisotropy energy per rare-earth atom is given by the expression

$$k_2^R = -3J(J-1)\alpha_J A_{20}\langle r^2\rangle \tag{5.10}$$

where J is the total angular momentum quantum number, α_J is the Stevens factor [139] and $A_{20}\langle r^2\rangle$ is the CEF parameter. Each of these is element specific. In Nd, $J = 9/2$ and $\alpha_J = -7/1089$. $A_{20}\langle r^2\rangle$ is generally calculated from first principles using either the local density approximation or the generalised gradient approximation to obtain an effective potential around the rare-earth nucleus. It is known however that both of these approximations are inadequate for describing strongly localised $4f$ electron states [46]. To the author's knowledge, the only work in which the CEF parameter has been calculated for $NdFe_{12}$ is that of Miyake et al. [46], in which values of -1.145e−21 J and 5.699e−21 J are calculated for $NdFe_{12}$ and $NdFe_{12}N_x$ respectively. The sign of the CEF parameter indicates easy-axis orientation along the c-axis (positive) or easy-plane anisotropy in the xy-plane (negative). Hence, the values given

above suggest that the Nd atoms in $NdFe_{12}$ have easy-plane anisotropy, and upon nitriding the anisotropy changes to out-of-plane, as is seen in $Nd_2Fe_{14}B$.

Substituting the calculated value of $A_{20}\langle r^2\rangle = -1.145\text{e}-21$ J for $NdFe_{12}$ into (5.10) gives $k_2^R = -3.976\text{e}-22$ J/atom. This rises to $k_2^R = 1.978\text{e}-21$ J/atom for $NdFe_{12}N_x$, which is both positive and significantly greater in magnitude, and in fact comparable to the second order constant of $Nd_2Fe_{14}B$.

Fe sublattice

The anisotropy of the 3d sublattice is a result of the magnetic moment coupling to the crystallographic axes via spin-orbit coupling [140]. In order to determine the magnetocrystalline anisotropy of the Fe sublattice, we can once again look to the non-magnetic rare-earth analogue compounds in which the sole contributor to the magnetocrystalline anisotropy is the Fe sublattice. Unfortunately, there exist no exact analogues to the binary compound $NdFe_{12}$, thus we must make do with ternary compounds. From these it is known that the Fe sublattice has its preferential axis along the c-axis [141], and the angular dependence of the sublattice anisotropy energy can be described by the simple uniaxial term $E_K = K_2 \sin^2\theta$. At 0 K, K_1 for $YFe_{11}Ti$ was measured to be 1.93 MJm^{-3} [142]. This equates to an average of $\sim$ 3.05e$-$23 J per Fe atom.

5.2.4 Hysteresis behaviour

We now simulate hysteresis loops in order to gain an insight into how the inter-sublattice coupling as well as the easy-plane anisotropy of the rare-earth sites manifest on the macroscopic scale. The easy-plane anisotropy of the rare-earth sublattice suggest that the calculated coercive field will be relatively small in comparison with that of $Nd_2Fe_{14}B$, in which the strong out-of-plane preference on the Nd sites serves to stabilise the magnetic ordering up to high fields. The hysteresis loops are simulated

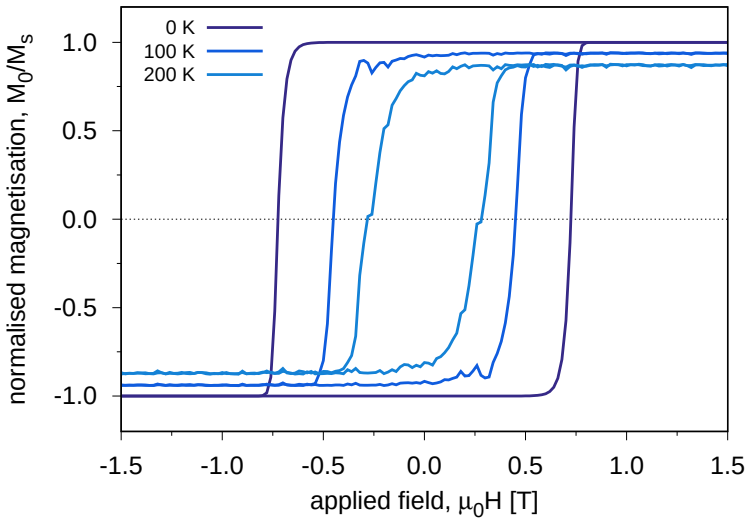

Figure 5.9: Calculated hysteresis loops for $NdFe_{12}$ at zero K, 100 K, and 200 K. The calculated coercivity is significantly lower than that for $Nd_2Fe_{14}B$, owing to the fact that the Nd, which serves to stabilise the system in $Nd_2Fe_{14}B$, here has an easy-plane anisotropy and thus reverses easily. The loops are relatively square, indicating a coherent reversal mechanism.

via integration of the LLG equation using the Heun method. Each loop was run with an applied field strength increment of 5 mT, with 30,000 equilibration time steps at each field point, followed by a further 10,000 time steps for averaging. The time step dt was 1 ps.

From Fig. 5.9 the calculated zero temperature coercive field is 0.73 T. This is significantly smaller than the zero temperature coercive field calculated for $Nd_2Fe_{14}B$ in section 5.1, and is certainly due to the easy-plane anisotropy on the rare-earth sites. As the field approaches the coercive field, both the Fe and Nd sublattices reverse easily, the Fe because of high sublattice moment and consequent high coupling to the external field, and the Nd sublattice because of its in-plane anisotropy. The squareness of the loops suggest a coherent reversal mechanism. In other words, the sublattices remain virtually collinear for the duration of the loop.

5.3 Cell size scaling of magnetic properties

In this section we investigate the cell size dependence of the saturation magnetisation and the magnetocrystalline anisotropy, using the method outlined in chapter 3.

5.3.1 Scaling of saturation magnetisation M_s

The results of the temperature dependence of the saturation magnetisation as a function of averaging cell size for $Nd_2Fe_{14}B$ and the generic BCC system with nearest-neighbour Heisenberg exchange are shown in Fig. 5.10. The results for the Heisenberg exchange are consistent with the previous work of Kirschner et al. [143]. Interestingly, cell size scaling in the case of $Nd_2Fe_{14}B$ is slightly weaker than that of the generic BCC system. This is perhaps surprising given the large unit cell size of the $Nd_2Fe_{14}B$. In this case, one might suppose that the discretisation of the system would suppress the spin fluctuations to a greater extent, resulting in a more severe scaling. The weaker scaling however is likely to be associated with the larger anisotropy of $Nd_2Fe_{14}B$, which results in an overall reduction in the spin fluctuations, thus making the averaged value in the cell a better approximation than in the generic BCC case.

5.3.2 Scaling of the magnetocrystalline anisotropy K

To extract the cell size dependence as well as the T dependence, we follow the same method as for the saturation magnetisation (Fig. 3.4), with one critical alteration. When the simulation is run at this stage, the comparison of the cell anisotropy with the total system anisotropy yields incorrect results. Because the two locales are exchange coupled to one another, the restoring torque on each affects the restoring torque of the other. That is, when one experiences a torque in one direction, the other experiences a torque an approximately equal and opposite torque. Thus it is necessary in this instance to remove the exchange interactions entirely for the torque

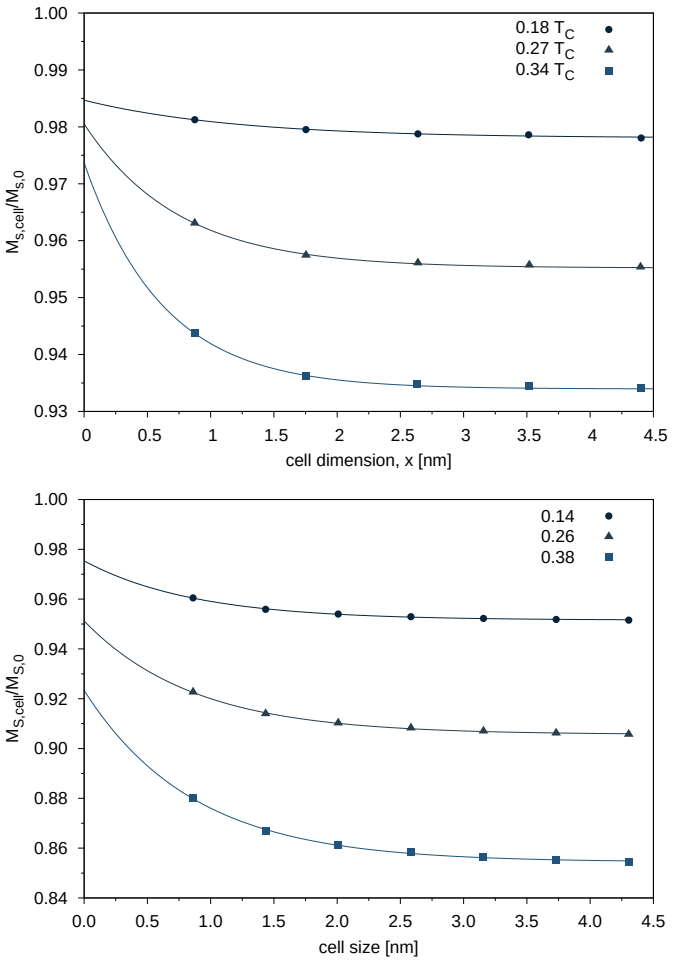

Figure 5.10: Scaling of the temperature dependence of the magnetisation with cell size for $Nd_2Fe_{14}B$ (top panel) and a generic bcc system with nearest-neighbour Heisenberg exchange (lower panel).

calculation. In this way, the spins within each region are free to move relative to each other but remain coupled to the anisotropy axis, allowing their relative torques to be compared.

In Fig. 5.11 is shown the scaling of the effective anisotropy as a function of averaging cell size at zero temperature. The constrained Monte Carlo was run with 50,000 equilibration steps and 50,000 averaging steps at each angle. The anisotropy of the averaging cell is divided by the total atomistic anisotropy of the system to give a ratio, where both values have been normalised to the volume. The effective anisotropy constant of the cell and the total system are extracted from the torques of

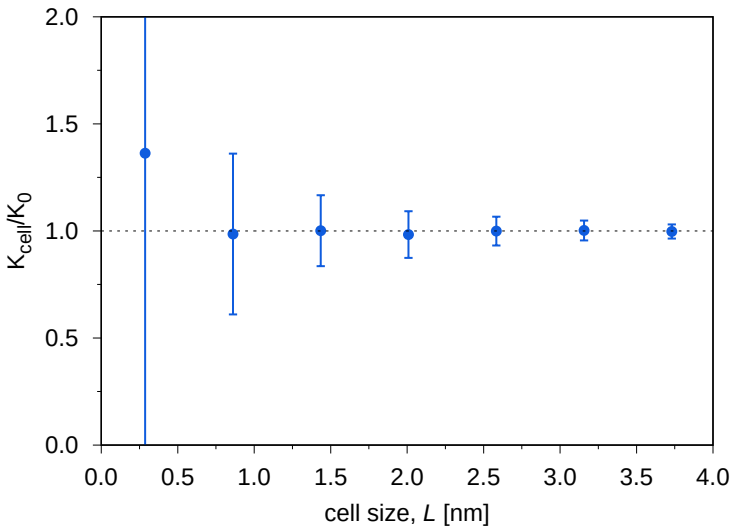

Figure 5.11: The ratio between the calculated macrocell K, K_{cell}, and the atomistic K_0 with averaging cell size at zero K. The error bars show the standard deviation across a sample of 100 simulations with varied random number seeds. It is seen that for increasing cell size there is a reduction in σ and a convergence of the mean value towards unity.

each part of the system by way of fitting to (3.11). The simulations were run using a series of 100 random seeds in order to find a mean ratio between K_{cell} and K_0 for each cell size. The error bars indicate the standard deviation from the mean value across the series of random seeds. In terms of the mean values, it can be seen that there is a convergence towards unity for larger cell size. The large deviations around unity at small cell size occur as a result of a statistical effect related to the fact that there are very few atoms being sampled. In fact, at the smallest cell size, there are only two atoms in the considered cell. Thus over the course of the simulation, if either of these two atoms becomes misaligned with respect to the other, this will skew the torque calculation. In the absence of the exchange interaction the energy cost of these atoms becoming misaligned is reduced considerably, further increasing the likelihood of a misalignment, though of course they are both coupled to the anisotropy axis. The deviation from the mean decreases with increasing cell size as the statistical sampling improves.

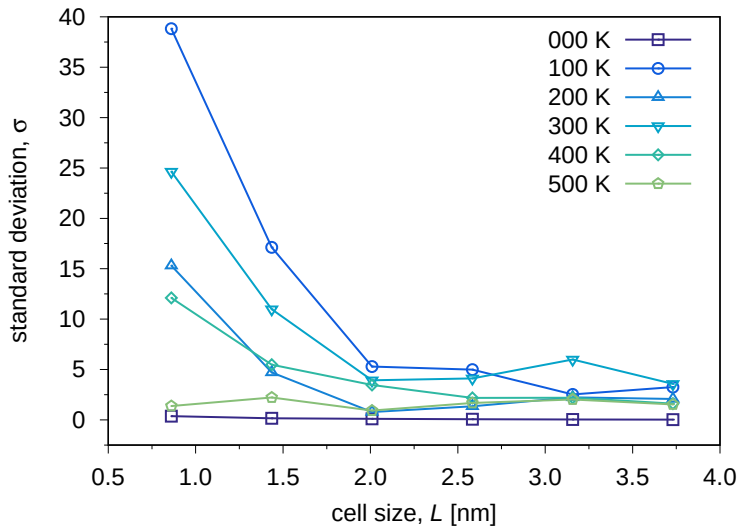

Figure 5.12: The standard deviation of K_{cell}/K_0 from the mean value, calculated from a sample of simulations with $N = 100$. For zero temperature it can be seen that there is relatively little deviation from the mean. For small L at finite temperatures a large deviation is seen due to statistical sampling of a small numbers of atoms within the cell. The standard deviation does not depend monotonically on the temperature, as stochastic effects dominate the system behaviour at these small system sizes.

In general, with increasing temperature fluctuations comes increased deviation from the mean. It can be seen in Fig. 5.12 that for zero temperature K_{cell}/K_0 lies very close to zero across the whole range of L, while the presence of spin fluctuations at finite temperatures causes a deviation from zero. The discrepancy from unity does not increase monotonically with increasing temperature as one would expect, however this can be attributed to the fact that at these small system sizes, stochastic effects dominate, particularly in the absence of the exchange field. Thus to generate an improved picture, we would need to go to larger system sizes.

From Fig. 5.12 it can be seen that the scaling of K for the averaging cell tends towards the atomistic value for larger cell sizes across the whole range of simulated temperatures. Thus we can say, at least for uniaxially anisotropic systems, that K does not scale with cell size, nor does it scale differently with temperature from the atomistic K. This might be surprising given that there is a scaling of M_{s} with L, and considering the Callen-Callen scaling relation that states that $K \propto M^3$ for a uniaxial

system [127]. From these results however it would appear that the lengthening of spin waves in the system through averaging of the magnetisation over a cell does not affect the macroscopic anisotropy.

5.4 Conclusion

In this chapter we have systematically parameterised the full atomistic model for the rare-earth transition-metal compounds $Nd_2Fe_{14}B$ and $NdFe_{12}$ using a combination of parameters derived from experimental measurements and some from *ab-initio* calculations. In the case of $Nd_2Fe_{14}B$ the crystal structure was derived from the Wyckoff sites given by Herbst et al. [22]. The magnetic moments were derived via comparison between experimental measurements of $Nd_2Fe_{14}B$ and one of its non-magnetic-rare-earth analogue compounds, $Y_2Fe_{14}B$. The exchange interactions were categorised into two species; the Fe-Fe interactions, and the Nd-Fe interactions. In the case of Fe-Fe, the exchange was treated as range dependent, with the functional form fit using the experimental Curie temperature. To parameterise the Nd sublattice anisotropy, the ratio of second and fourth order uniaxial constants was derived using *a priori* knowledge of the canting angle, and then fixed by solving the angular dependence of the anisotropy energy.

Having obtained a full set of parameters, we looked next at the hysteresis behaviour of the system. The two sublattices were seen to exhibit distinct behaviour, a result of the sublattices coupling to the external field with different coupling strengths. The effect of the spin-reorientation temperature was seen in the finite temperature hysteresis loops, resulting in a change in the shape of the loop from square to rounded as the temperature exceeded T_s.

Next we investigated the temperature dependence of M_s for both sublattices. The calculated total magnetisation was found to match closely the experimentally mea-

sured dependence, with the bulk of the magnetisation coming from the Fe sublattice due to the large moment.

Overall the procedure for parameterising of the spin model for $Nd_2Fe_{14}B$ worked well and successfully reproduced the expected results. The subtleties of the magnetic behaviour, for example the changing of the shape of the hysteresis curves between $T < T_s$ and $T > T_s$ came out of the model in a natural way, forming a solid basis for further investigations of more complicated structures.

From here we moved onto the parameterisation of the spin model for $NdFe_{12}$. The procedure was largely similar to that used for $Nd_2Fe_{14}B$, though complicated by the comparatively scarce availability of experimental data with which to compare our calculations. The crystal structure is one aspect that is well known as the compound crystallises in the well documented $ThMn_{12}$ structure. The exchange interaction strengths were fit by to the experimentally measured T_c as before, and it was determined that the appropriate exchange interaction range for the Nd-Fe interactions in this case was 2 nearest-neighbour shells. The anisotropy values were derived from crystal field parameters calculated by Miyake et al. [46]. The Nd sites were found to have an easy-plane anisotropy in the base compound $NdFe_{12}$, and an easy axis out-of-plane anisotropy in the nitrided compound $NdFe_{12}N_x$.

With the parameterisation completed, the hysteresis and temperature dependence of the magnetisation were calculated. The calculated hysteresis curves for $NdFe_{12}$ were found to give a very low zero temperature coercivity, certainly in comparison with $Nd_2Fe_{14}B$. While to the author's knowledge there are no experimental hysteresis loops with which to compare, the low value for H_c can be explained by the easy-plane anisotropy of the Nd. By comparison, it is the strong, out-of-plane anisotropy of the Nd sublattice in $Nd_2Fe_{14}B$ that gives it such a high coercivity.

Finally, we investigated the cell size scaling of the saturation magnetisation and the magnetocrystalline anisotropy for two systems: $Nd_2Fe_{14}B$, and a generic uniaxial

BCC Fe system. The results of the calculations showed that there was a weaker dependence on cell size for the saturation magnetisation of $Nd_2Fe_{14}B$ than for the generic Fe system, most likely due to the larger anisotropy in $Nd_2Fe_{14}B$.

Chapter 6

Effect of grain-boundary interfaces on $Nd_2Fe_{14}B$ coercivity

6.1 Introduction

Despite the remarkable magnetic properties of $Nd_2Fe_{14}B$ that have made it the permanent magnet of choice in high-performance motor applications since its discovery almost 40 years ago, one of the primary problems that still persists is that the coercive field measured in sintered $Nd_2Fe_{14}B$-based magnets is often much lower than expected from theoretical predictions.

According to the seminal Stoner-Wohlfarth theory of magnetism [130], an ideal magnetic material with high magnetocrystalline anisotropy should reverse its magnetism via coherent rotation and H_c should be equivalent to the value of the anisotropy field, H_a. In this scenario, a perfectly rectangular hysteresis loop is observed, and the theoretical maximum energy product is given by

$$(BH)_{\max} \leq \mu_0 M_s^2/4, \tag{6.1}$$

where M_s is the saturation magnetisation and μ_0 is the magnetic moment. However, in the best commercially produced magnets, currently H_c does not exceed $\sim 40\%$ of H_a. This misalignment with the theoretical maximum is known as Brown's paradox [35].

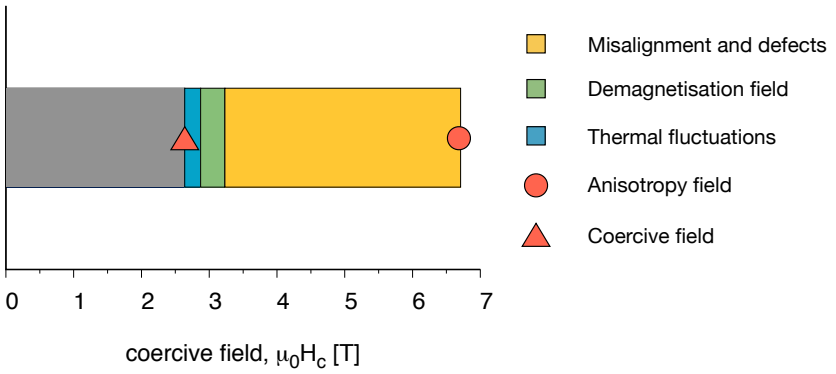

Figure 6.1: The figure shows the different contributions which cause the measured difference between the anisotropy and coercive fields in $Nd_2Fe_{14}B$. Adapted from Ref. [144]

There are a number of factors which cause this measurable difference between H_a and H_c [145] (these are shown in Fig. 6.1). Generally the most significant is the effect of grain misalignment and defects. The resulting reduction in coercivity is approximately 50% of the anisotropy field [144]. Examples of defects could be antiphase boundaries, where a dislocation in the crystal matrix shifts one region out of phase with an adjacent region, observed in $Nd_2Fe_{14}B$ by Li et al. in 1991 via HRTEM [146]; or inter-granular boundaries which separate adjacent grains. In $Nd_2Fe_{14}B$, a number of different types of inter-granular boundary are observed. Some of the most common are NdO phases, sometimes called Nd-rich phases; and α-Fe phases, which generally consist of BCC-ordered Fe. Defects such as these are believed to result in a reduction in anisotropy in the local region around the defect [145]. These in turn act as nucleation points for reversal of the magnetic domain, leading to an overall reduction in H_c of the system.

The second most significant factor is the dipolar field, sometimes called a demagnetisation field, which reduces the total energy of a system by inducing a domain structure on length-scales above the so-called critical single-domain limit (measured at $\sim$ 300 nm) in $Nd_2Fe_{14}B$ [147]. This particular factor will not play a role in the investigations that follow in this chapter as all of the simulated systems are smaller than this critical limit.

In this chapter are presented an analysis of the local environment around intergranular boundary phases, specifically α-Fe type phases, how they affect the local anisotropy and how this affects the propagation of domain walls through the system.

6.2 Domain wall characterisation

Typically domain wall width (δ_w) is a material-dependent quantity, described by the relation

$$\delta_w \approx \pi \sqrt{\frac{A}{K_u}} \tag{6.2}$$

where A is the exchange-stiffness and K_u the unaxial anisotropy constant, thus narrow domain walls are costly with respect to the exchange energy but are favoured in high anisotropy materials, of which $Nd_2Fe_{14}B$ is one, hence δ_w in $Nd_2Fe_{14}B$ is very small.

In order to calculate the domain wall width in $Nd_2Fe_{14}B$ it necessary to create a system which forces the presence of a domain wall. Thus we generate a system that is long along one dimension with respect to the other two. This system is then split into two halves, one in which all atomic spins point along the $+z$-direction, and one has spins which all point along $-z$. In order to prevent the domain wall from being forced out of the system, which would ordinarily occur naturally to minimise the overall system energy, we impose *anti-ferromagnetic* periodic boundary conditions in the 'long' dimension of the system, i.e. along the system axis. A schematic of the system setup is shown in Figure 6.2.

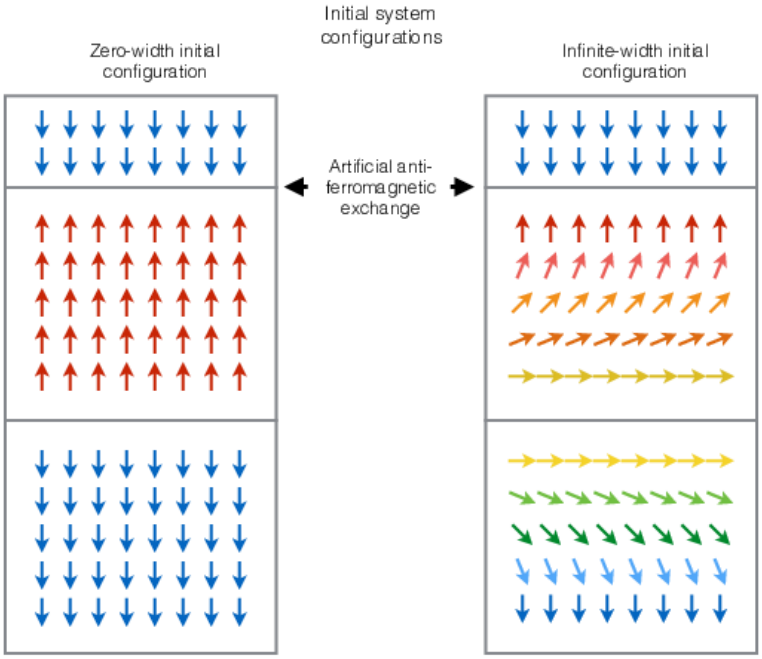

Figure 6.2: Schematic of initial configurations for domain wall width calculations. Artificial anti-ferromagnetic exchange is imposed between the top two layers to stabilise the movement of the domain wall. Periodic boundary conditions are used to link the top and bottom layers, as well as in the x and y directions to avoid finite size effects.

Because of the crystallographically anisotropic nature of the $Nd_2Fe_{14}B$ unit cell, δ_w will vary depending on the direction along which it is measured. Specifically, the distribution of anisotropy throughout the system is non-uniform. Regions of high anisotropy are concentrated in the planes of Nd, with areas of lower anisotropy occupying the area between the planes. One therefore would expect that in a system where the domain wall is forced to orient itself parallel to the Nd planes, δ_w should be smaller than in systems where the domain wall is oriented parallel to the c axis. Another way of picturing this would be to say the Nd and Fe sublattices are arranged such that there is high coupling within the plane, and weak coupling out of plane. In view of this we have investigated two systems; one in which the system extends along

the x axis, and one in which the system is extended along the z axis. The results of the zero-temperature calculation are shown in Figure 6.3.

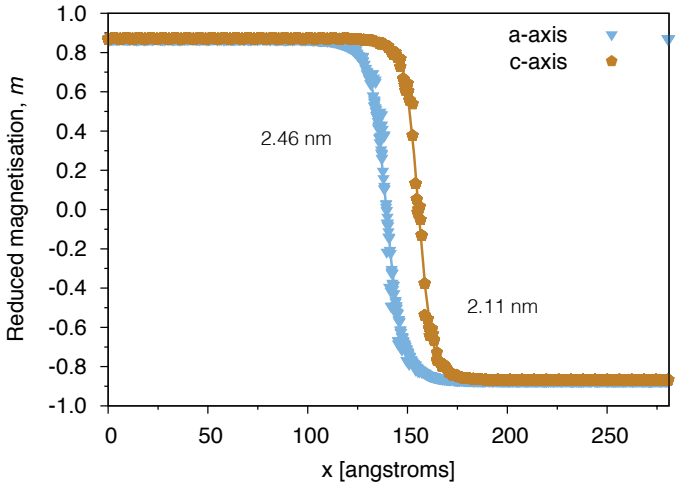

Figure 6.3: Calculated zero-temperature domain wall widths in $Nd_2Fe_{14}B$ along the [001] and [100] directions.

The value of δ_w is extracted by fitting the data with the function $m(x) = \tanh(\pi x/\delta_w)$, where x is the position along the axis of the system. δ_w in the system with unit cells stacked along the c axis was calculated to be 2.11 nm, while in the other system δ_w was found to be wider, at 2.46 nm.

Substituting this result into (6.2), for which we already know the value of K_u, we are able then to extract a value for A, which is an important quantity in micromagnetics calculations. Moreover, calculation of $\delta_w(T)$ allows extraction of $A(T)$, which is necessary as input for finite temperature micromagnetics calculations.

6.3 Site-resolved magneto-elastic anisotropy energy

Using the Néel model described in section 3.3, we have calculated the magneto-elastic anisotropy (MAE) at each site of the Fe sublattice as a function of height in the

unit cell (distance along c axis). The values were generated by taking the difference between the anisotropy calculated for a hard axis [100] spin-polarised system and for an easy axis [001] spin-polarised system. It can be seen that the energies appear at specific 'levels', of which there are approximately six. This is consistent with the picture that groups of atoms that are a part of the same symmetry group, of which there are six for the Fe atoms in the $Nd_2Fe_{14}B$ unit cell, should have an identical local environment, and hence the same energy. The results are shown in Fig 6.4.

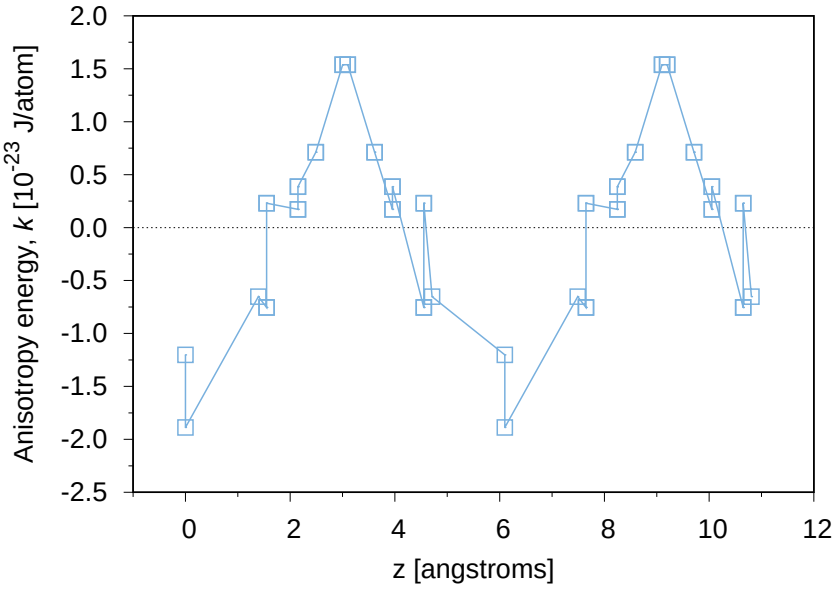

Figure 6.4: Néel pair anisotropy energy calculated at each Fe site in the $Nd_2Fe_{14}B$ unit cell as a function of position along the z axis.

Positive anisotropy energy indicates a preference for the magnetic moment to lie out-of-plane, while a negative energy corresponds to an in-plane preference. Although the distribution in Fig. 6.4 appears to sum to something close to zero, there is in fact a higher density of points in the positive regime, though the points overlap as points with the same z-coordinate will often occupy identical energy levels. Integrating over all sites results in a positive total energy.

Having shown that using Néel model for calculating the MAE gives reasonable results, we proceed to a much more complicated system, a grain-boundary interface.

In order to get as realistic a picture as possible of the interface, we collaborated with Gino Hrkac's group at the University of Exeter, who specialise in molecular dynamics simulation, with which they were able to relax an interface system between $Nd_2Fe_{14}B$ and α-Fe. The full details of the method used are described in Ref. [93]. The interface is shown in figure 6.5.

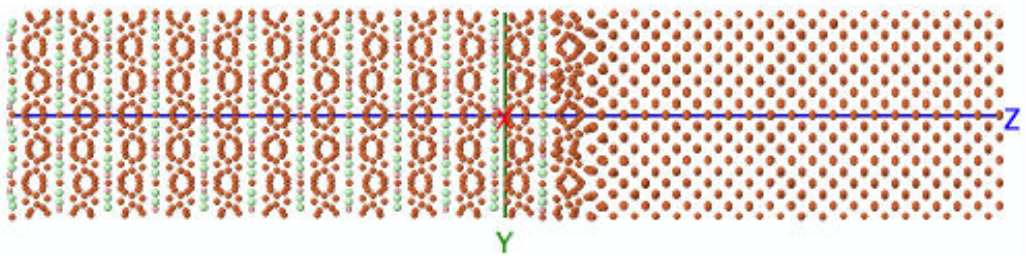

Figure 6.5: Interface between $Nd_2Fe_{14}B$ and α-Fe phases, relaxed using MD. The system has dimensions $12.8 \times 2.64 \times 2.64$ nm and contains 6912 atoms.

As before, the anisotropy energy was calculated as a function of the position along the z axis, which is parallel to the crystallographic c axis. To eliminate edge effects in the x and y directions, periodic boundaries were implemented along these axes.

Fig. 6.6 shows the calculated site-resolved MAE along the axis of the system. The magneto-elastic contribution in the bulk Fe phase fluctuates about zero energy as is expected inside a BCC structure, as the contributions from neighbours in all directions cancel to zero. The fluctuations because of the strain induced by the MD relaxation. The sharp increase at the vacuum interface of the α-Fe phase is an edge effect that results from the absence of periodic boundaries in the z-direction. Similar to the single unit cell case, fluctuations in the energy of the Fe sublattice of the $Nd_2Fe_{14}B$ phase are observed due to the presence of distinct symmetry groups.

At the interface we find a highly localised transition region $\sim$0.5 nm wide where the anisotropy energy becomes negative. This suggests that at the interface there is indeed a small region where weak anisotropy due to local disruption of crystal symmetry may behave as a kind of chink in the $Nd_2Fe_{14}B$ grain armour where domain walls can pass through more easily than they otherwise could. To investigate this idea

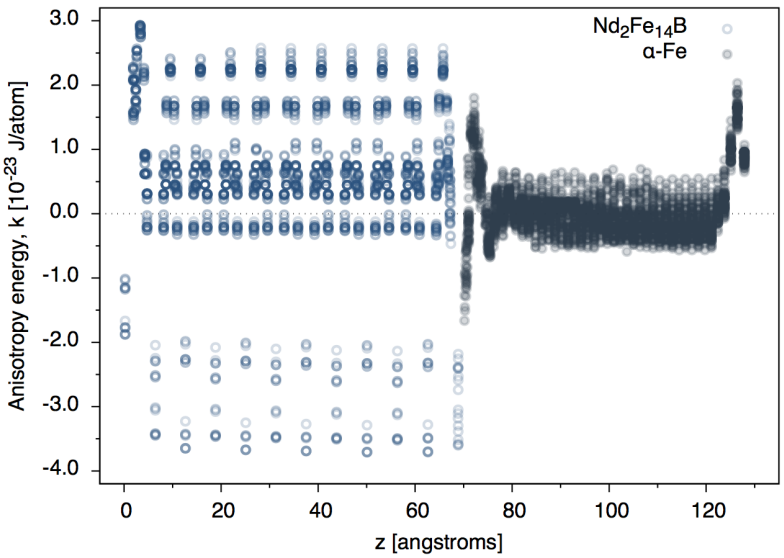

Figure 6.6: Calculated magnetic anisotropy profile through a relaxed $Nd_2Fe_{14}B/\alpha$-Fe interface, showing atomistic scale variation of the MAE.

further, we have carried out atomistic spin dynamics calculations to simulate domain wall dynamics across this interface.

We first begin by setting up our system in a way that mimics two $Nd_2Fe_{14}B$ grains separated by an α-Fe inter-granular phase. As shown in the schematic (Fig. 6.7), the interface between the two phases provided to us by the University of Exeter was duplicated, mirrored, and then aligned in order to simulate what one would expect to find in the region between two grains in a real $Nd_2Fe_{14}B$-based magnetic material.

With our system prepared, we parameterise each atomic site in the manner discussed in section 5.1. Again as in section 6.2, anti-ferromagnetic periodic boundary conditions are imposed between the two termini of the system to ensure that the domain wall is not immediately forced out of the system, allowing the entire system to polarise itself in the same direction to minimise energy. We then initialise our system such that each $Nd_2Fe_{14}B$ grain is spin polarised in opposite directions; one along the $+z$-direction and the other along the $-z$-direction (axes as defined in Fig. 6.5). The inter-granular phase is oriented in-plane to better facilitate nucleation of a domain wall. An external magnetic field was then applied to the system along the z axis.

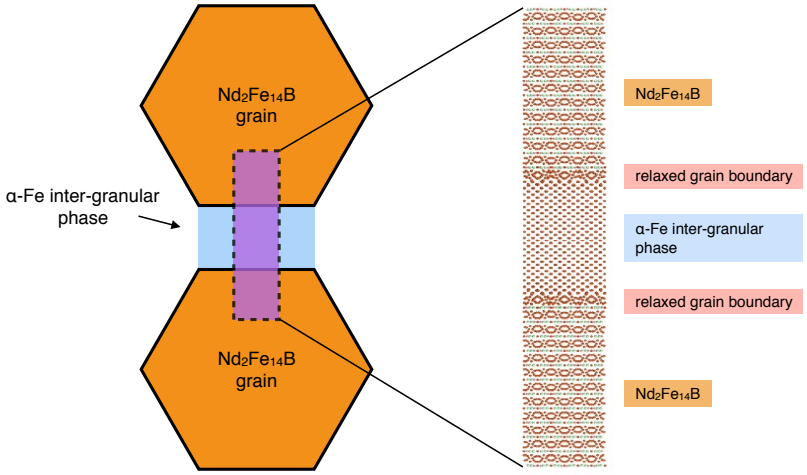

Figure 6.7: The left side shows a schematic of a typical pair of $Nd_2Fe_{14}B$ grains separated by an inter-granular phase of α-Fe. The purple highlighted area shows the area we are to simulate. The relaxed interface between $Nd_2Fe_{14}B$ and α-Fe provided to us by the University of Exeter was mirrored and aligned in order to reproduce what one would expect to find between two adjacent grains in a $Nd_2Fe_{14}B$-based material.

The externally applied field, H_{app}, acts to push the domain wall in the same direction as the field. The magnitude of H_{app} required to push the domain wall through into the grain should then shed some light on the effect of the weakened anisotropy at the interface on the coercivity.

6.4 Spin dynamics

Figure 6.8 shows a depiction of the interface system where each point in the image is an atomic spin. The colour of the point represents the direction along which the spin points, with white corresponding to in-plane, and red and blue corresponding to $-z$ and $+z$ respectively. It can be seen that under the influence of a magnetic field pointing along the axis of the system, the domain wall traverses the length of the system. Upon closer inspection it becomes apparent that the domain wall does not

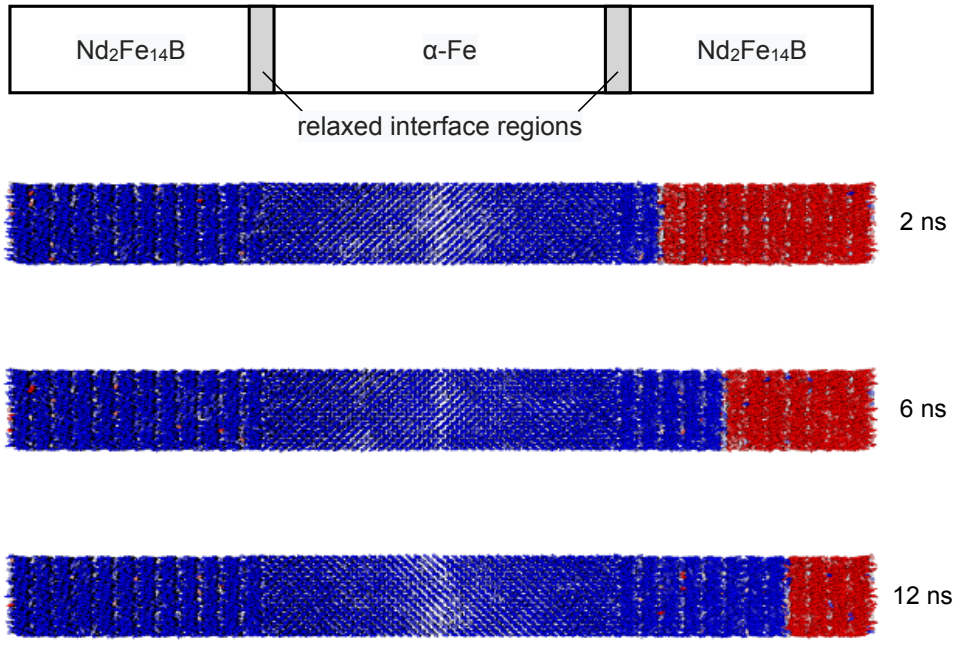

Figure 6.8: The three panels show the mirrored interface system at three different time steps: $t = 2$, 6, and 12 ns. Each point represents an atomic spin, with red indicating a spin pointing in the $-z$-direction, blue a spin pointing in the $+z$-direction and white a spin oriented in the plane. It can be seen that after the domain wall has passed through the α-Fe phase into the hard $Nd_2Fe_{14}B$ phase it is stopped or pinned at successive Nd layers.

propagate at a constant rate, but rather in a stuttering fashion. We find that the domain wall is in fact being pinned at each layer of Nd in the hard phase, i.e. the parts of the system which contribute most to the magnetocrystalline anisotropy of the material.

This stuttering motion can be more easily seen in Figure 6.9 where the distance of the domain wall from the interface between the soft and hard phases is shown as a function of time. It can clearly be seen that the domain wall spends some length of time at certain points along the length of the system before 'hopping' to the next pinning site. Looking closely at the positions where the domain wall becomes

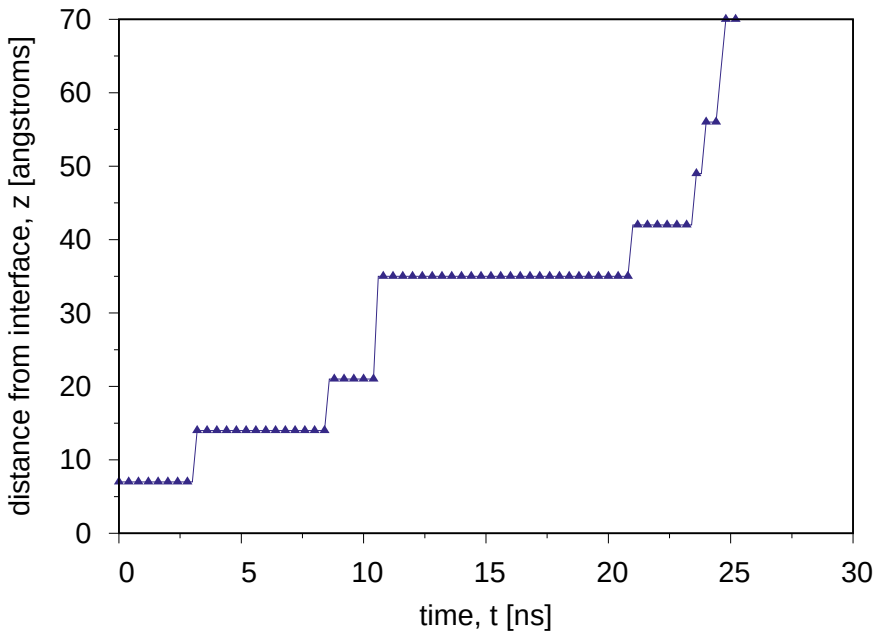

Figure 6.9: Position of the domain wall as a function of time. Here the numbers on the y-axis represent the distance between the domain wall and the interface between the α-Fe and $Nd_2Fe_{14}B$ phases. The domain wall appears to exhibit a kind of 'hopping' behaviour, spending some finite amount of time at certain points within the system before travelling rapidly to the next pinning site.

pinned we can see that these corresponds to the positions of the Nd layers which lie perpendicular to the axis of the system. These occur at regular intervals of 6.1 Å.

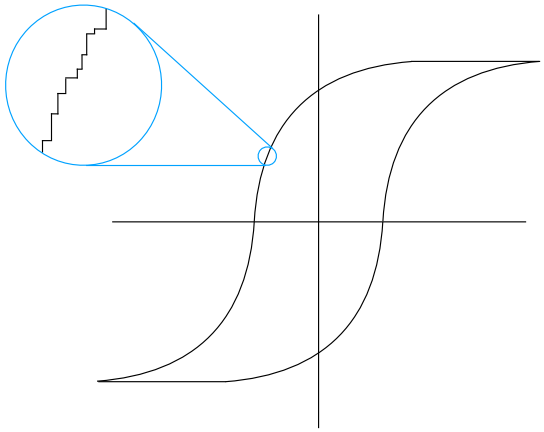

Figure 6.10: Schematic diagram of a hysteresis loop showing the effect of the Barkhausen type jumps seen in the domain wall propagation in Figs. 6.8 and 6.9 on the switching behaviour in $Nd_2Fe_{14}B$.

The behaviour described above is known as *Barkhausen* noise, or Barkhausen jumps, and corresponds to a kind of magnetic domain reversal similar to what is depicted schematically in Figure 6.10. This phenomenon was observed in works as early as 1989 by Otani et al. [148], described as 'large, discontinuous changes in the magnetisation near the coercive field'. The jumps observed by Otani et al. were on a larger length scale than those observed here, with each jump corresponding to a 5% change in the total magnetisation of the system, however it is reasonable to believe the mechanism at play behind both is the same, i.e. that layers of high magnetocrystalline anisotropy originating from the 4f Nd atoms act as pinning sites for domain walls acting to reverse the system in the presence of an external magnetic field.

The applied field required to push the domain wall into the hard $Nd_2Fe_{14}B$ phase was calculated to be ~ 9 T. This is much larger than the stray fields one would expect in a real system. One suggestion is that the important factor is the crystallographic orientation of the $Nd_2Fe_{14}B$ phase. In our calculations, only one type of interface was investigated; that where the orientation of the high anisotropy Nd planes are oriented perpendicular to the direction of propagation of the domain wall. Thus we suggest that this is not an ideal orientation for domain walls to pass through, and that if one were to repeat the calculation for a system in which the domain wall propagation direction was parallel to the a-axis, a much smaller field would be required to push the domain wall into the hard phase. Thus the $Nd_2Fe_{14}B$ grain is seemingly topologically protected in certain crystallographic directions. This could be one of the main reasons why the coercive field of $Nd_2Fe_{14}B$ is measured to be much smaller than theoretically predicted.

6.5 Conclusion

In this chapter we have investigated the idea that in granular $Nd_2Fe_{14}B$, one of the reasons that the measured coercivity is much smaller than theoretical calculations predict is that there is weakened anisotropy at the boundaries between the $Nd_2Fe_{14}B$ grains and the inter-granular boundary phases, which allow domain walls to pass easily into the grains. We investigated the anisotropy as a function of position across one such interface using the Néel anisotropy model. The results showed no conclusive evidence that the anisotropy is weakened at the interface. Using the anisotropy profile as input into the atomistic spin dynamics model, we modelled the propagation of a domain wall across the interface, using an externally applied field as a driving force for the domain wall motion.

From the spin dynamics simulations we draw two conclusions. First the atomistic resolution shows that the domain wall does not propagate smoothly through the $Nd_2Fe_{14}B$ phase as one might expect. Instead the domain wall becomes pinned at successive Nd planes due to the high anisotropy, resulting in propagation via a series of Barkhausen jumps.

The second conclusion is that the crystallographic orientation of the grain with respect to the interface is important. It was found in our system that a very large field was required to force the domain wall into the $Nd_2Fe_{14}B$ grain. We propose that the reason for this is that the $Nd_2Fe_{14}B$ is oriented so that the Nd planes are parallel to the interface, and perpendicular to the direction of propagation of the domain walls. We conjecture that this creates a strong barrier against switching, and that rotating the $Nd_2Fe_{14}B$ grain by 90° with respect to the interface would result in switching at much lower fields.

It is clear, then, that the next thing to investigate is the dependence of the field strength required to force a domain wall into a $Nd_2Fe_{14}B$ grain on the crystallographic orientation of the grain with respect to the interface. If the results of this showed

strong dependence, this could potentially guide future $Nd_2Fe_{14}B$ based magnet designs to be engineered on the nano scale in such a way that the grains make use of this conjectured topological grain protection to increase the coercivity as much as possible.

Chapter 7

Effects of Ti and Zr substitution in RFe_{12}

In this chapter we investigate the effects of substituting atoms in the RT_{12} phase with either Zr or Ti. The ultimate goal of this section is to be able to understand to some extent the effects of Zr and Ti when they are inserted into the crystal, as they are two of the more common substitutes used in industrial manufacturing of rare-earth permanent magnets for use in high-performance motor applications. Both are used primarily as sources of phase stability, as RT_{12} in its binary form is meta-stable. So far $NdFe_{12}$ has only been synthesised once [36], as a thin film and with nitrogenation. We first look at the effects of transition-metal site Ti substitution on inter-sublattice coupling between the Fe and rare-earth sublattices in $NdFe_{12}$; followed by the effects of rare-earth site substitution of Zr and its effects on the magnetic properties in $SmFe_{12}$.

7.1 Ti substitution on transition metal sites in RT_{12}

As discussed in section 5.2, $ThMn_{12}$-type rare-earth intermetallics are generally considered intrinsically unstable as binary compounds, i.e. as RT_{12} (R = rare earth, T =

transition metal) [133]. The most common way of stabilising the phase, first investigated by De Mooij and Buschow [133], is to use a third element M, which is usually one of Ti, V, Cr, Mn, Mo, W, Al or Si. In each of these cases, the stabilising element substitutes one or more of the transition metal sites in the unit cell, forming the ternary compound $RT_{12-x}M_x$. In general it is found that the most promising choice for the element T is Fe, which gives high magnetic moment and anisotropy [133].

In the recent computational work of Miyake et al. [46], it was calculated that substitution of Ti changed the crystal electric field parameter A_{20} on the rare-earth site from -83 K in $NdFe_{12}$ to 54 K in $NdFe_{11}Ti$, indicating that the preferential alignment had switched from in-plane to out-of-plane. Thus the Ti acts both as a method of stabilising the phase and providing out-of-plane anisotropy, which is essential in high-performance motor applications. It was also found however that Ti substitution (with $x = 1$) has the drawback of causing a reduction in the magnetic moment of 4.9 μ_B per formula unit. This is due to a small spin magnetic moment on the Ti sites which couples anti-parallel to the Fe sublattice. This however does not explain all of the lost moment. The secondary effect of the Ti is to reduce the moments on all Fe sites in the unit cell via a narrowing of the $3d$ band [46]. From this point of view it is necessary to understand how the Ti behaves inside the unit cell in terms of site preference as well as how the substitution affects the macroscopic magnetic behaviour.

7.1.1 Ti distribution in the unit cell

Work was carried out in collaboration with Hrkac's molecular dynamics group at the University of Exeter as part of an ongoing effort to create a fully multiscale model of rare-earth permanent magnets.

It was found that for the first Ti atom inserted into the RT_{12} unit cell, there is essentially a zero probability of it occupying any sites other than those of the $8i$

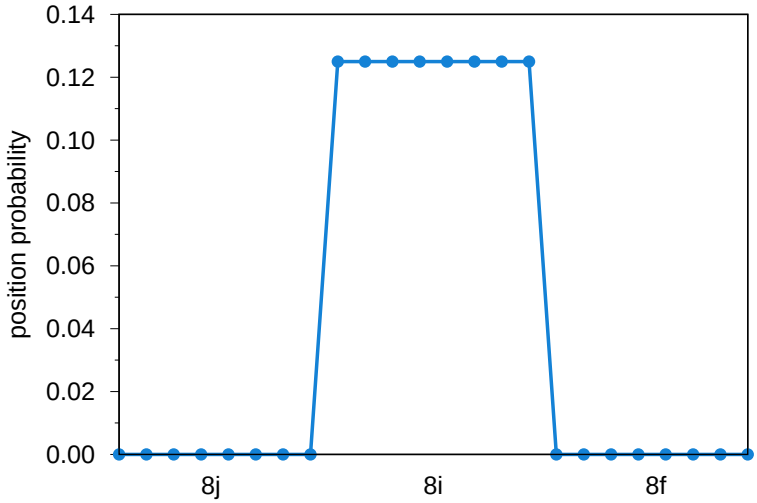

Figure 7.1: Probability distribution of Ti atom occupying different Fe sites in the unit cell at 300 K. $8j$, $8i$ and $8f$ denote the Fe symmetry groups.

symmetry group (Fig. 7.1). This is in agreement with calculations performed by Miyake et al. [46], as well as with experiments carried out on similar compounds by De Mooij and Buschow [133]. Crucially, it is the $8i$ sites which form the shell of nearest-neighbours surrounding the rare-earth atoms. De Mooij and Buschow suggest that the reason the stabilising element prefers to occupy the 8i site may be that there are only four nearest 8i neighbours to each rare-earth atom, while the 8j and 8j sites surround the R site in larger numbers, thus the 8i sites have the smallest area of contact with the R site. Considering that there is a positive enthalpy contribution associated with R and M contact, this may explain why the Ti prefers these sites [133].

This preference of the Ti to sit on the site nearest to the R atom leads to the hypothesis that the Ti may play a screening role around the rare-earth site, cutting it off from interactions with neighbour Fe moments. The question of inter-sublattice coupling strength is extremely important in the determination of whether a material is a viable candidate for high-performance motor applications, as it will play an important role in maintaining a necessarily high maximum energy product.

7.1.2 Parameterisation of $R(Fe_{1-x}Ti_x)_{12}$

As alluded to in section 7.1, the two important effects to consider when substituting Ti into the $ThMn_{12}$ crystal structure are

1. changes to the lattice parameters a and c, which will have an effect on the degree of overlapping of atomic orbitals and in turn the total exchange interaction energy

2. and the replacement of one or more ferromagnetically coupled, large moment Fe spins with an antiferromagnetically coupled, low moment Ti spin.

To take account of the first effect, in our model we have as input the dependence of the lattice parameters on Ti substitution calculated using molecular dynamics simulation by our collaborators at the University of Exeter (Fig. 7.2). Using molecular dynamics with parameterised force fields, $NdFe_{12}$ super-cell structures were simulated. Ti was inserted into the system and the resulting minimum energy structures found to determine the change in the lattice parameters for each concentration of Ti.

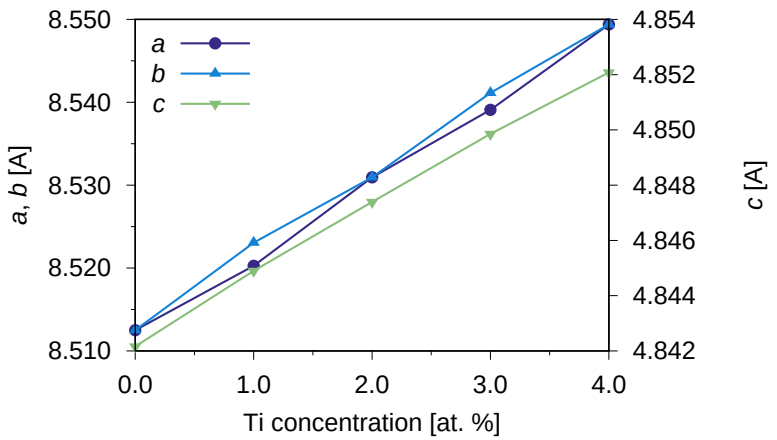

Figure 7.2: Lattice parameters a, b, and c as a function of the Ti concentration in $NdFe_{12}$. Substituting 4 at.% Ti results in an expansion from the base compound of 0.21% in c, and 0.43% in a and b.

It can be seen from Fig. 7.2 that all calculated lattice parameters increased with increasing Ti concentration; going from 0-4 at.% a and b increased by 0.43%, and c by 0.21%. It is interesting to note that the lattice expansion is not isotropic in the basal plane. At 1 and 3 at.% the a parameter differs marginally from the b parameter by 0.002 Å, suggesting some form of anisotropic bonding between the Ti atom and its neighbours. However, the disparity is on a length scale that should be sufficiently small as to have no significant impact on the inter-atomic exchange interaction.

7.1.3 Exchange energy as a function of Ti concentration

Taking into account the points outlined in the beginning of this section, we assert that the strength of the exchange coupling should change as a function of Ti content. Given that we have *a priori* knowledge of how the T_c changes as a function of Ti substitution, we can fit the exchange interaction using the same parameter space scan method discussed in section 5.2.2.

Parameter space scans were carried out for each concentration of Ti. The salient part of each generated heat map, that is, the band of allowed values, was extracted. These are shown in Fig. 7.3. The series of points that characterise each band were extracted by collecting parameter sets for which the calculated T_c was within 10 K of the expected value. As was the case for the heat maps in Fig. 5.7, for the low inter-sublattice coupling regime the bands are flat, as the magnetisation is dominated in this regime by the Fe-Fe exchange coupling. To simplify the picture, lines were fit only to the parameter sets outside of this Fe-Fe dominated regime. The lines of best fit serve only as an interpolation between the parameter pairs that yield the correct T_c.

It can be seen that there is a noticeable reduction in the strength of the exchange interactions required to give the correct T_c for each concentration of Ti. Whilst we are unable to pin down exactly where along each band the correct pair of exchange

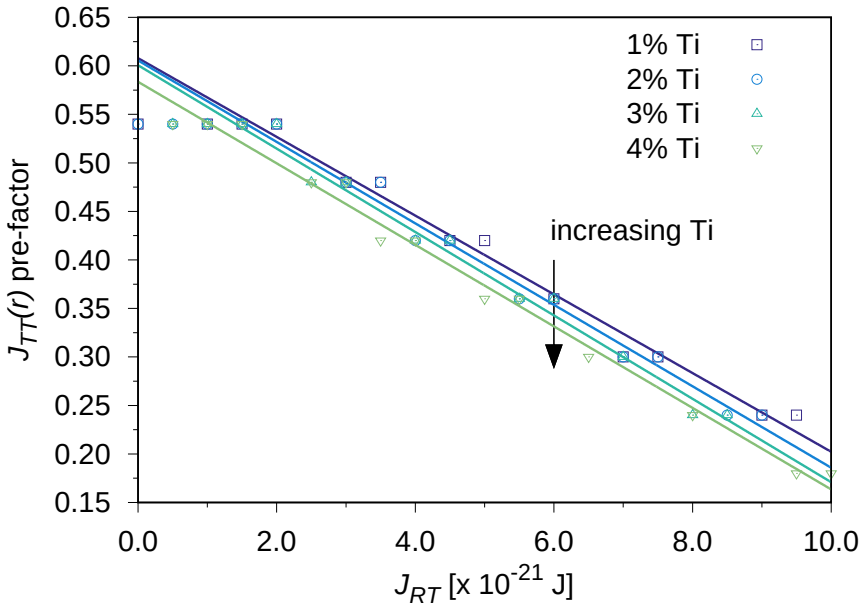

Figure 7.3: Extracted bands of acceptable pairs of exchange parameters as a function of Ti content. There is a marked reduction in the necessary exchange interaction strength to achieve the experimentally measured T_c for each concentration of Ti.

parameters lies, it is clear that the exchange energy is reduced as a result of the presence of the Ti. This rather nicely aligns with the picture that the preference of the Ti atom to occupy the sites adjacent to the rare-earth, has a screening effect which reduces the coupling between the rare-earth and transition metal sublattices.

A reduction in the inter-sublattice coupling will in principle have a dramatic effect on the temperature dependence of the anisotropy. If the rare-earth sublattice is less strongly coupled to the Fe sublattice as a result of the Ti, at finite temperatures there will be larger magnetisation fluctuations resulting in the anisotropy dropping off more rapidly with temperature. This will have an effect not only on the temperature dependence of the magnetisation, which may be one reason that the T_c decreases with increasing Ti concentration, but also on the switching field.

In order to corroborate this picture, we look now at how the presence of the Ti substitute affects the preferential alignment of the Nd site using the Néel anisotropy model presented in section 3.3. The Néel model gives an idea of how the local

magneto-elastic anisotropy will vary as a result of changes in the local crystal symmetry, which is known to be altered as a consequence of Ti substitution.

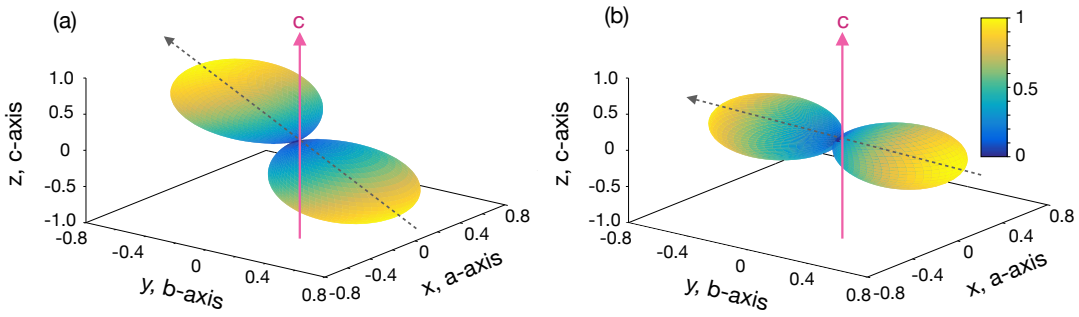

Figure 7.4: (a) shows the calculated Néel anisotropy energy surface of the Nd site for the case where there is 1 at.% Ti substitution. In this case the preferred alignment for the rare-earth spin is $\sim 39^\circ$ from the c-axis. (b) Here is shown the same calculation for the Nd site for the case where the crystal has 3 at.% Ti substitution. In this case the preferential axis lies in the ab plane.

In Fig. 7.4 are shown the calculated Néel anisotropy energy surfaces for the Nd sites in $Nd(Fe_{1-x}Ti_x)_{12}$. The left panel shows the calculation for the case where there is 0% Ti substitution. In this case the preferential axis for the rare-earth site lies at $\sim 39^\circ$ from the c-axis. In the right panel is shown the calculation for the case where there is 3 at.% Ti substitution. In this case the preferred axis for the rare-earth spin is in the ab plane. Interestingly, this result appears to come about primarily as a result of the asymmetric lattice expansion induced by the Ti. The changes in the energy surfaces calculated for between 0 and 2 at.%. are insignificant, and it is only at 3 at.% that a significant change is seen. At 4 at.% the energy surface returns to the same orientation as is seen for 0 to 2 at.%. From Fig. 7.2 we see that the asymmetric expansion in the ab plane occurs only at 1 at.% and 3 at.% substitution.

The Néel contribution to the anisotropy energy is small relative to the on-site anisotropy contribution. Thus a change in orientation of the rare-earth Néel anisotropy energy surface may in reality only cause a slight tilting of the spin rather than a full reorientation in-plane. It is difficult to say what the exact size of the

contribution of the Néel anisotropy is, due to the difficulty in parameterising the weighting function $L_{ij}(r)$, as discussed in section 3.3. Nonetheless it is useful in giving some picture of how local changes in the crystal symmetry affect the anisotropy of the rare-earth sites.

7.2 Zr substitution on rare-earth sites in RT_{12}

$SmFe_{12}$, like $NdFe_{12}$, is considered a meta-stable phase, and is only able to be synthesised in the binary form as a thin film. It does however differ from $NdFe_{12}$ in that $SmFe_{12}$ has been theoretically predicted to show large uniaxial anisotropy in the binary phase. This makes it an attractive prospect for investigation. While $SmFe_{12}$ binary films have been synthesised numerous times [80, 149–151], experimental data on the intrinsic hard magnetic properties of $SmFe_{12}$ remain scarce.

One way to stabilise these phases in the bulk is substitution of a third element, as was explored in section 7.1 with Ti substitution of the Fe sites in $NdFe_{12}$. The problem in general with partial substitution of transition metal sites in the RT_{12} phase is the accompanying loss of magnetic moment. This loss is proportional to the degree of substitution, with the effect of the substitute twofold. Firstly the removal of an Fe atom subtracts from the magnetic moment of the $3d$ sublattice which is the primary source of magnetisation in the rare-earth transition-metal compounds. Secondly there is evidence that the presence of the stabilising element narrows the $3d$ band, reducing the magnetic moments on all transition-metal sites in the unit cell. To circumvent this problem, it has been suggested that partial substitution of rare-earth sites by Zr be used to stabilise the $ThMn_{12}$ structure. This was successfully carried out in Refs. [152–155], in which various compounds of type $(R,Zr)T_{12}$ were synthesised using the strip casting method, where R = Nd or Sm. In this way, the

large magnetic moment is maintained. Here we investigate the effects of substituting Zr into $SmFe_{12}$.

One key observation when Zr is substituted onto the rare-earth sites in a $ThMn_{12}$ crystal structure is that there is an overall reduction in the unit cell volume, which can be attributed to the fact that the Zr atomic radius is $\sim 84\%$ that of a Sm or Nd atom [156] at 1.55 Å. The effect was quantified in the compound $Nd_{1-x}Zr_xFe_{10}Si_2$ by Sakurada et al. [157] using the rapid quench method (Fig. 7.5). Linear decrease of both the a and c lattice parameters as a function of Zr concentration is observed in $Nd_{1-x}Zr_xFe_{10}Si_2$, with the reduction in a contributing more significantly to the unit cell volume reduction.

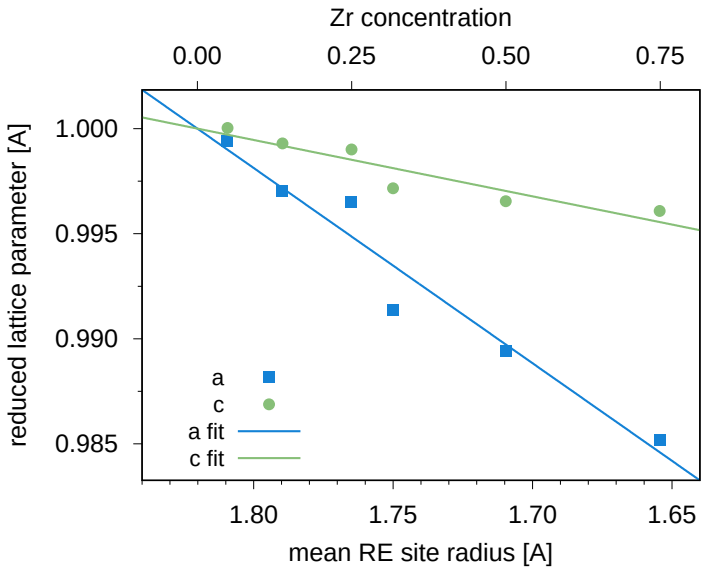

Figure 7.5: Adapted from Ref. [157]. The plot shows the measured change in lattice parameters a and c as a function of Zr substitution in $Nd_{1-x}Zr_xFe_{10}Si_2$. Both a and c can be fit linearly, with the behaviour of a contributing most to the unit cell volume reduction.

The Zr is assumed to have zero magnetic moment. Thus the effect of the Zr is to decrease the total coordination number within the crystal. This would suggest that the magnetic ordering of the remaining magnetic moments is reduced. Increased Zr content will also be accompanied by a loss of magnetocrystalline anisotropy which stems primarily from the rare-earth atoms. In our model the Zr atoms are distributed

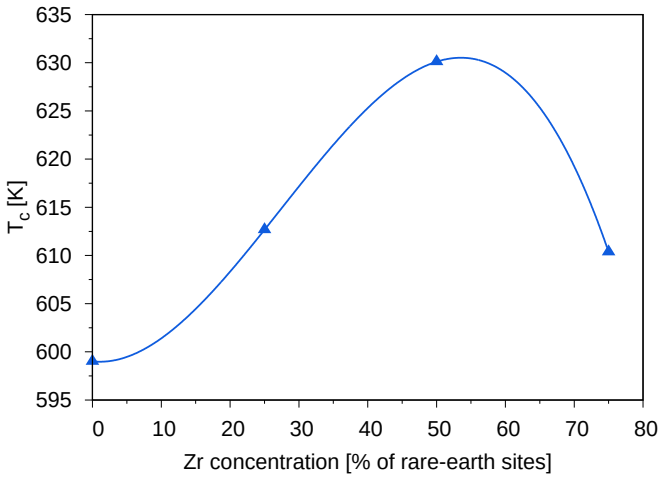

Figure 7.6: Curie temperature, T_c as a function of Zr concentration. The Curie temperature increases with Zr concentration up to a peak value of 630.1 K at 50% Zr, before decreasing at higher concentrations.

randomly across all rare-earth sites in the simulated system using a pseudo random number generator algorithm.

Using the lattice parameters from Fig. 7.5 as input into the spin dynamics model we proceed by calculating the temperature dependence of the saturation magnetisation across a range of concentrations. The simulations are run using a Monte-Carlo algorithm, with 10,000 Monte-Carlo steps for equilibration at each temperature step, and a further 10,000 for averaging of the magnetisation at each step. A temperature step increment of 10 K was used, and the T_c extracted via fitting of (5.9). The results are shown in Fig. 7.6.

It can be seen that there is an increase in the calculated T_c for low concentrations up to a peak of 630.1 K for 50% occupation of rare-earth sites. Further increase of Zr concentration then results in a decrease of the T_c, though still higher than the zero Zr value. There are several factors at play here. First there is the shrinking of the crystal lattice, which results in increased overlap of atomic orbitals throughout the crystal, leading to increased ordering of magnetic spins. In the model the effect is produced by stronger exchange coupling energy between Fe-Fe and Sm-Fe pairs, as shown in

Fig. 5.2. The second effect is the replacement of magnetic Sm atoms by non-magnetic Zr atoms resulting in a local reduction in Sm-Fe exchange interactions. The two effects work against one another, with the first dominating at low Zr concentrations, resulting in the increase in T_c, and the second dominating in the high Zr regime, acting to reduce the T_c.

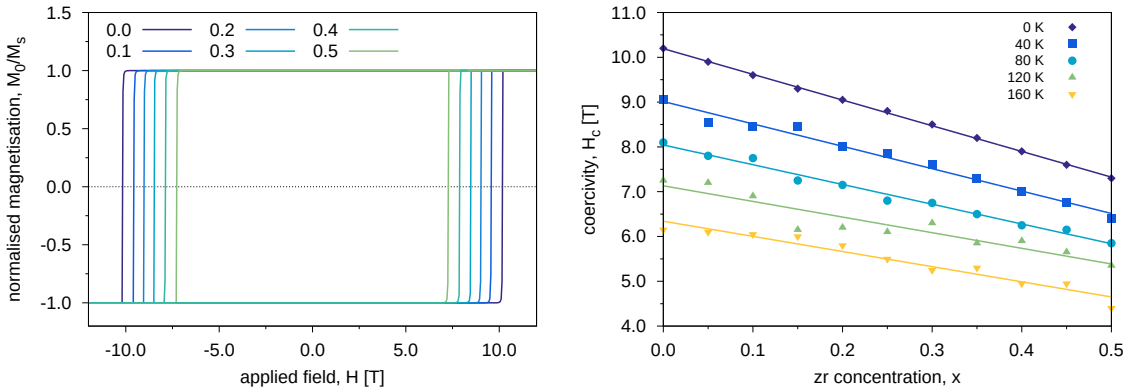

(a) (b)

Figure 7.7: (a) shows simulated hysteresis loops at zero temperature as a function of Zr substitution. At zero percent Zr substitution, the $SmFe_{12}$ has a coercive field of 10.2 T. At 50% Zr substitution the coercive field is reduced by 30%. (b) shows the calculated coercivities for temperatures between 0 and 160 K as a function of Zr substitution. It can be seen that there is a consistent reduction in coercivity with increased Zr substitution as expected, though the Zr content does not affect the temperature dependence of the coercivity.

We continue the investigation by looking at the effects of Zr substitution on the hysteretic properties of $SmFe_{12}$. We run hysteresis loop simulations using the LLG equation integration method in order to get an accurate picture of how the spin dynamics affect the reversal mechanism. A system of volume 10 nm^3 was selected in order to mitigate finite size effects. The field was swept at a real time rate of 10^9 Ts^{-1} with a simulation time step of 1 fs.

We calculate the coercive field of $Sm_{1-x}Zr_xFe_{12}$ as functions of x and of temperature. The simulated zero K hysteresis loops are shown in Fig. 7.7a. For $x = 0$ the coercive field is calculated to be 10.2 T. This is significantly lower than that seen in

$Nd_2Fe_{14}B$, due to the smaller contribution to the anisotropy from the rare-earth sites, however is still large compared with experimental calculations. This disparity can be attributed to the fact that we do not take into account dipolar effects, nor the effect of defects (see Fig. 6.1), thus we are effectively calculating the intrinsic anisotropy field which is expected to be higher. With increasing Zr content the calculated coercivity decreases significantly. At 50% Zr substitution the coercive field is reduced by 30%. This is due to a reduction in the total magnetocrystalline anisotropy in the crystal.

The dependence of the coercivity in $Sm_{1-x}Zr_xFe_{12}$ as a function of temperature is shown in Fig. 7.7b. The coercivity decreases relatively consistently with Zr concentration at each temperature, dropping 28% at $x = 0.5$ at the highest simulation temperature 160 K. Above this temperature the calculated values for the coercive field became much less reliable, with higher concentration systems switching at higher fields than lower concentration systems in some cases, indicating that the stochasticity induced by the temperature fluctuations was dominating the system behaviour.

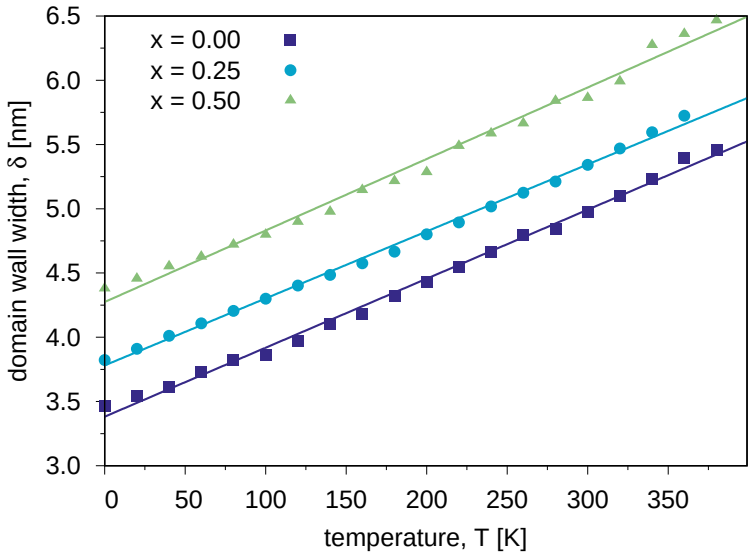

Figure 7.8: Calculated domain wall width δ as function of temperature and Zr substitution. At each concentration δ is well fit as a linear increase with temperature. δ also increases with Zr substitution due to a reduction in the magnetocrystalline anisotropy.

We look now at the effect of Zr substitution on the calculated domain wall width δ in $Sm_{1-x}Zr_xFe_{12}$. δ is calculated using the procedure outlined in chapter 5, wherein a system is initialised such that two halves are aligned anti-parallel relative to one another, and anti-ferromagnetic periodic boundary conditions are imposed in order that the artificially inserted domain wall is stable. From Fig. 7.8 it can be seen that δ increases linearly with temperature. This dependence in the low temperature regime is well known [158]. With increasing Zr substitution δ is seen to increase. This behaviour can be understood by reference to the well-known formula $\delta = \pi\sqrt{A/K}$ describing domain wall width as function of the exchange stiffness and magnetocrystalline anisotropy. The reduction in magnetocrystalline anisotropy arising as a result of substitution of Sm atoms by non-anisotropic Zr atoms results in the system relaxing to an equilibrium state in which more atoms can readily orient in-plane, widening the domain wall width. The increased overlap of atomic orbitals which occurs as a result of the shrinking of the unit cell inducing an effective increase in the total exchange field works in conjunction with the reduction in anisotropy to increase δ.

7.3 Conclusions

In this chapter we have investigated the effects of Ti substitution of the transition-metal sites in $NdFe_{12}$ and the effects on the magnetic properties of Zr site substitution of Sm atoms in $Sm_{1-x}Zr_xFe_{12}$.

$NdFe_{12}$ is considered a meta-stable phase, and in most cases requires partial substitution on one of the sublattices of a stabilising element. A particularly effective stabilising element is Ti. Ti is substituted onto the transition metal sites. Molecular dynamics calculations have shown that the Ti preferentially selects the $8i$ sites to substitute, which are the sites that reside adjacent to the R element. A primary effect of Ti substitution is a loss of magnetisation due to losing some number of transition-

metal atoms, which are the primary source of magnetisation in the compound. It is hypothesised that a second effect is that due to the site preference of the Ti, there will be a screening effect around the rare-earth atom which will in turn have an effect on the inter-sublattice coupling, an important factor in the viability of a compound for use in electric motors as the inter-sublattice coupling is an important indicator of the maximum energy product.

The results presented in this chapter show that there is certainly a reduction in the total exchange energy in the compound as a whole, though it cannot be said conclusively whether the reduction is coming from a reduction in the inter-sublattice exchange or the intra-sublattice exchange of the transition-metal sublattice.

In the second part of the chapter the effects of Zr substitution of Sm atoms in $Sm_{1-x}Zr_xFe_{12}$ was investigated. The two principal effects brought about by Zr substitution are a reduction in the unit cell volume, and a decrease in the magnetocrystalline anisotropy. The first occurs due to the smaller atomic radius of the Zr atom with respect to the Sm atom, and the second due to the removal of Sm atoms, which contribute significantly to the magnetocrystalline anisotropy. It was shown that the T_c calculated as a function of Zr concentration follows a non-monotonic dependence, increasing up to 50% site substitution but decreasing for higher concentrations. The coercivity was shown to drop with increasing Zr content, while the domain wall width increases with increased Zr due to an increase in the exchange field and the accompanying reduction in anisotropy.

Chapter 8

Conclusions

In this thesis, the properties of rare-earth transition-metal permanent magnets were investigated, specifically with regard to how atomic scale features affect the macroscopic properties. $Nd_2Fe_{14}B$ based magnets were investigated, as well as the new family of RFe_{12} compounds. In this chapter the main results and conclusions from the thesis will be summarised, and then the future research will be discussed.

In brief, one of the main problems facing the use of rare-earth permanent magnets, $Nd_2Fe_{14}B$ based magnets in particular, is that they are required to function well at high operating temperatures. $Nd_2Fe_{14}B$ has the drawback of losing coercivity, and therefore maximum energy product, at high temperatures. There are several approaches to solving this problem. Three approaches were looked at in this thesis. The first of which was exchange coupled nanocomposite materials, which was considered in chapter 4. In this approach a magnetically soft phase is exchange coupled to a hard phase in order to improve the overall magnetic properties of the base material. The second was by gaining more understanding of the microstructural features that occur at grain boundary interfaces. This was discussed in chapter 6. It is believed that defects at the grain boundary interface cause a weakening of the anisotropy, which facilitate the propagation of domain walls into the hard phase. By better understand-

ing the mechanisms at work here, we can perhaps guide the manner in which future materials are designed. The third approach was the search for a novel compound. The RFe_{12} family of compounds has recently been put forward as a potential replacement for $Nd_2Fe_{14}B$, however the phase is known to lose magnetisation with the addition of a required stabilising element. Thus is necessary to quantify the affects of these stabilising elements. This we did in chapter 7. The results presented in each of these chapters will be summarised in the following.

Core/shell $Nd_2Fe_{14}B/\alpha$-Fe nanoparticles

We investigated idealised core/shell nanostructures with soft/hard morphology with $Nd_2Fe_{14}B$ forming a magnetically hard shell and α-Fe forming the magnetically soft core. The system was modelled using a generic form of the atomistic spin dynamics model and parameterised by fitting to experimental data.

It was demonstrated that there was an enhancement of the total magnetisation of the composite system with increasing α-Fe content due to the high magnetisation of the soft phase and the coupling of this to the hard phase. The soft phase was able to stabilise the hard phase at elevated temperatures. The enhancement in the magnetisation was shown to be offset by an accompanying reduction in the coercivity of the composite. The reduction was shown to be more severe for larger particle size due to the increase in inter-phase exchange coupling. The combination of these two effects resulted in an overall increase in the maximum energy product of the nanoparticle with increasing α-Fe content, up to an optimum value of $\sim$ 70% Fe, after which the maximum energy product began to drop off. The results support the idea that the exchange coupling of hard and soft magnetic materials on the nanoscale has the potential to greatly enhance the magnetic properties of rare-earth permanent magnets.

Parameterisation of the full atomistic spin model

In this chapter the aim was to expand upon the previous model used in the core/shell investigation by parameterising the $Nd_2Fe_{14}B$ crystal structure in a fully atomistic way. To do this, a combination of experimental parameters and parameters calculated from first principles was used. One of the major obstacles to successfully parameterising rare-earth permanent magnet spin models is that current *ab initio* methods do not properly describe the effects of the unpaired $4f$ electrons which are the primary source of the singular magnetic properties of these compounds.

First we looked at the parameters for $Nd_2Fe_{14}B$. The first step was to determine the atomic coordinates of all the constituent atoms in the complex $Nd_2Fe_{14}B$ unit cell. Once these were established, the magnetic moments of each site were assigned using values found in the literature. The exchange interactions were categorised into two types: Fe-Fe and Nd-Fe. Nd-Nd interactions were neglected due to their large separation distances in the unit cell, as is usual in atomistic models of rare-earth transition-metal compounds. The Fe-Fe interactions were fit using a range-dependent functional form of the exchange based on first principles calculations of the Fe-Fe interactions in BCC Fe by Pajda et al. [122]. The Nd-Fe interaction strengths were then used as a fine tuning parameter to yield the correct Curie temperature. The anisotropy values were determined from experimental values, with the ratio of the second order anisotropy constant to the fourth order constant on the Nd sites calculated using *a priori* knowledge of the spin canting angle below the spin reorientation temperature.

With the parameters in place, a systematic investigation of the fundamental macroscopic properties was carried out. The calculated hysteresis behaviour was shown to successfully reproduce experimentally measured coercivity values. A change in the shape of the hysteresis curves above and below the spin-reorientation temperature was seen - a result of the correct ratio between the second and fourth order uniaxial anisotropy constants on the Nd sites. The $M_s(T)$ dependence was calculated,

resolved by sublattice, giving the correct Curie temperature, and showing that the majority of the magnetisation in the compound originates from the 3*d* Fe sublattice. With this full parameterisation, we have shown a working model of $Nd_2Fe_{14}B$ that will serve as a solid grounding for future investigations into more complex structures based on the $Nd_2Fe_{14}B$ crystal structure.

In the second half of the chapter, the novel $NdFe_{12}$ base compound was parameterised. This presented more of a challenge than the $Nd_2Fe_{14}B$ due to the relative scarcity of experimental data on the material. The crystal structure was straightforward to reproduce, given that the compound crystallises in the $ThMn_{12}$ crystal structure which is well documented. The exchange interactions Nd-Fe and Fe-Fe were treated as free parameters and scanned until the correct Curie temperature was found. First principles calculations by Miyake et al. [46] of the crystal field parameters were used to parameterise the on-site magnetocrystalline anisotropy constants. In contrast with $Nd_2Fe_{14}B$, the Nd sites in $NdFe_{12}$ have an in-plane anisotropy. This had a significant effect on the hysteresis behaviour, resulting in coercivities lower than 1 T at zero temperature.

Having parameterised fully both $Nd_2Fe_{14}B$ and $NdFe_{12}$, these models were used in chapters 6 and 7 to explore more complicated crystal structures.

The cell size scaling of the saturation magnetisation and magnetocrystalline anisotropy were also investigated. The coarse grained micromagnetics method has a tendency to overestimate quantities such as the T_c, which can be corrected by taking the aforementioned parameters as dependent on L and T, i.e. $K = K(L,T)$, $M_s = M_s(L,T)$, and $A = A(L,T)$.

$M_s = M_s(L,T)$ was calculated for two systems; $Nd_2Fe_{14}B$ and a generic uniaxial BCC Fe system. It was found that for the $Nd_2Fe_{14}B$ system there was a weaker dependence on cell size and temperature than for the BCC Fe system. This is a surprising result given the larger unit cell size of $Nd_2Fe_{14}B$, but is likely an effect of

the larger anisotropy of the rare-earth material, which suppresses the spin fluctuations in the atomistic model.

Given the complexity of modern magnetic materials it is clear that there is a need for a multiscale approach to permanent magnet modelling. Such an approach would involve a link up between first principles calculations, atomistic spin models and coarse grained micromagnetics models. The process might look something like the following: lattice parameters and anisotropy values calculated in the *ab-initio* regime, effects of structural defects on the local spin dynamics calculated using atomistic spin models, and calculations of large-scale complex designs such as the 'Battenburg' structure [51] using as input information gleaned from the smaller scale models. Thus it would in principle be possible to solve large magnetic systems essentially from first principles.

Effects of grain boundary interfaces on $Nd_2Fe_{14}B$ coercivity

In this investigation the aim was to probe the interfaces in $Nd_2Fe_{14}B$ between the $Nd_2Fe_{14}B$ grains and the inter-granular phases at an atomic resolution. It is theorised that defects at the interfaces induce weak local anisotropy which in turn allow for easier switching of the grains by allowing domain walls to penetrate more easily.

The local anisotropy was profiled using the Néel anisotropy model across an interface between $Nd_2Fe_{14}B$ and α-Fe relaxed using molecular dynamics simulation. There was no conclusive evidence of any local weakening of the anisotropy at the interface. Using the relaxed interface and calculated anisotropy profile as input into the spin dynamics, the propagation of a domain wall across the interface driven by an external magnetic field was modelled.

Two main conclusions were drawn from the simulated domain wall propagation. First that the domain wall did not propagate through the $Nd_2Fe_{14}B$ phase with a smooth motion. Rather the motion was stuttered as a result of the orientation of the high anisotropy Nd planes, which were oriented in this case perpendicular to the

direction of propagation of the domain wall. The result was a Barkhausen type noise in the magnetisation switching. Second, it was found that a very large field (~ 9 T) was required to force the domain wall into the $Nd_2Fe_{14}B$ phase. Extending this idea of the orientation of the Nd planes being a key factor in the switching mechanism, it was conjectured that the Nd planes being oriented parallel to the interface acts as a topological barrier against the switching of the magnetisation of the $Nd_2Fe_{14}B$ grain. We predict that in cases where the $Nd_2Fe_{14}B$ grain is oriented such that the Nd planes lie parallel to the direction of domain wall propagation, that is, with the interface parallel to the c axis, a much smaller external field would be required to force the domain wall into the $Nd_2Fe_{14}B$ grain.

Effects of Ti and Zr substitution in RT_{12}

In chapter 7, the effects of the substitution of a stabilising element into the RT_{12} compound were studied. The RT_{12} family of compounds, include $NdFe_{12}$, are considered a meta-stable phase in the binary, and in general require a ternary stabilising element to be used in any application. A commonly used stabilising element is Ti, which substitutes a transition-metal site upon entering the unit cell. Work was carried out by our collaborators in Hrkac's molecular dynamics simulation group at the University of Exeter to determine the preferential substitution sites for Ti. It was found that the preferred site for the Ti atom is the $8i$ transition-metal site, which sits adjacent to the rare-earth site. Thus it was hypothesised that this might have a screening effect around the R atom, resulting in a reduction in the inter-sublattice exchange coupling, a parameter important in determining the maximum energy product in electric motor applications.

Inserting the Ti atom into our spin model, with lattice parameter variation calculated by molecular dynamics simulation used as input information, we calculated the exchange energy as a function of Ti content. It was found that there was an overall

decrease in the total exchange energy in the system, however there was no conclusive evidence to say that the reduction was in the inter-sublattice coupling specifically.

In the second part, the effects of Zr substitution in $Sm_{1-x}Zr_xFe_{12}$ was investigated. The two principal effects brought about by Zr substitution are a reduction in the unit cell volume, and a decrease in the magnetocrystalline anisotropy brought about by the removal of rare-earth atoms. The first effect comes about as a result of the smaller atomic radius of the Zr atom with respect to the Sm atom. The Zr was substituted into our spin model using a random site selection algorithm. The T_c was then calculated as a function of Zr concentration. It was found that the T_c follows a non-monotonic dependence, increasing up to 50% site substitution but decreasing at higher concentrations. The coercivity was shown to drop with increasing Zr content, while the domain wall width increases with increased Zr due to an increase in the exchange field and the accompanying reduction in anisotropy.

As with the $NdFe_{12}$ parameterisation in chapter 5, there is unfortunately little experimental data with which to compare our results. The Ti substitution effect on the inter-sublattice coupling will require deeper investigation to answer the question as to whether or not the Ti is in fact screening the rare-earth site.

In this thesis we have taken strides towards a multiscale paradigm, for example a number of calculations made use of *ab initio* parameters from the literature. Other investigations, into Ti substitution for example, involved direct collaboration with molecular dynamics research groups to try to establish a direct chain between the models.

Going back to the initial aim posed in chapter 1, we have successfully parameterised a full working atomistic spin model of $Nd_2Fe_{14}B$ and $NdFe_{12}$, both of which, as has been discussed, are exceptionally complex materials. Applying the model to a $Nd_2Fe_{14}B/\alpha$-Fe grain boundary interface, the finding was made that there appears to be a kind of topological protection of the grain along certain crystallographic di-

rections. More work must be done to quantify this effect, however we suggest that nano-scale design of the grain boundaries to protect the grains from domain wall nucleation and domain reversal may be an avenue for future permanent magnet design. The investigation into elemental substitution in the RFe_{12} phase showed that, particularly in the case of Zr substitution on the rare-earth sites, that an improvement in some of the macroscopic properties can be made, namely in the Curie temperature.

Further work

There are a number of questions that have arisen as a result of the investigations carried out in this thesis. As a follow up to the core/shell study, it would be a useful experiment to apply what was learnt in the parameterisation of the full $Nd_2Fe_{14}B$ spin model to nanocomposite particles. To reveal the effects of exchange coupling hard and soft magnetic phases using a fully atomistic approach would be a natural extension to the generic model that was used as a first approximation in this instance.

Work remains following on from the investigation into the full parameterisation of the $Nd_2Fe_{14}B$ and $NdFe_{12}$ models. The inter-sublattice coupling in the RFe_{12} compounds remains an open question and warrants a thorough investigation in the future. One way this could be probed would be to atomistically calculate the magnon dispersion relations for the RFe_{12} phases as materials with weak and strong inter-sublattice coupling are known to show very distinct spin wave dispersion. However the complexity and low symmetry of these types of materials make the calculations non-trivial to set up as well as computationally expensive.

Following on from the grain boundary interface investigation, there is yet work to be done in confirming or disproving the hypothesis that the granular orientation with respect to the interfaces will play a large role in determining the coercivity of $Nd_2Fe_{14}B$ based magnets.

In regards to the full implementation of a multiscale approach to the modelling of permanent magnets, an urgently required continuation is the cell size and temperature dependence of the exchange stiffness constant A. One way to go about calculating the temperature dependence is to use the relation between domain wall width, exchange stiffness and anisotropy (given by (6.2)). The calculation of the cell size dependence will require a more subtle approach.

Bibliography

[1] J D Livingston. The history of permanent-magnet materials. *JOM*, 42(2):30–34, February 1990.

[2] H C Oersted. *Experiments on the Effect of a Current of Electricityon the Magnetic Needle*. C. Baldwin, 1820.

[3] P Weiss. L'hypothèse du champ moléculaire et la propriété ferromagnétique. *J. Phys. Theor. Appl.*, 6(1):661–690, 1907.

[4] D C Mattis. *The Theory of Magnetism I: Statics and Dynamics*. Springer Science & Business Media, December 2012.

[5] S A Wolf, D D Awschalom, R A Buhrman, J M Daughton, S von Molnár, M L Roukes, A Y Chtchelkanova, and D M Treger. Spintronics: a spin-based electronics vision for the future. *Science*, 294(5546):1488–1495, November 2001.

[6] I Žutić, J Fabian, and S Das Sarma. Spintronics: Fundamentals and applications. *Rev. Mod. Phys.*, 76(2):323–410, April 2004.

[7] E Saitoh, M Ueda, H Miyajima, and G Tatara. Conversion of spin current into charge current at room temperature: Inverse spin-hall effect. *Appl. Phys. Lett.*, 88(18):182509, May 2006.

[8] K Uchida, S Takahashi, K Harii, J Ieda, W Koshibae, K Ando, S Maekawa, and E Saitoh. Observation of the spin seebeck effect. *Nature*, 455(7214):778–781, October 2008.

[9] N Liebing, S Serrano-Guisan, K Rott, G Reiss, J Langer, B Ocker, and H W Schumacher. Tunneling magnetothermopower in magnetic tunnel junction nanopillars. *Phys. Rev. Lett.*, 107(17):177201, October 2011.

[10] H Yu, S D Brechet, and J Ansermet. Spin caloritronics, origin and outlook. *Phys. Lett. A*, 381(9):825–837, March 2017.

[11] M H Kryder, E C Gage, T W McDaniel, W A Challener, R E Rottmayer, G Ju, Y Hsia, and M F Erden. Heat assisted magnetic recording. *Proc. IEEE*, 96(11):1810–1835, November 2008.

[12] B C Stipe, T C Strand, C C Poon, H Balamane, T D Boone, J A Katine, J L Li, V Rawat, H Nemoto, A Hirotsune, O Hellwig, R Ruiz, E Dobisz, D S Kercher, N Robertson, T R Albrecht, and B D Terris. Magnetic recording at 1.5 Pb m^{-2} using an integrated plasmonic antenna. *Nat. Photonics*, 4:484, May 2010.

[13] D Weller, O Mosendz, G Parker, S Pisana, and T S Santos. $L1_0$ FePtX-Y media for heat-assisted magnetic recording. *Phys. Status Solidi*, 210(7):1245–1260, July 2013.

[14] J Fortin, C Wilhelm, J Servais, C Ménager, J Bacri, and F Gazeau. Size-sorted anionic iron oxide nanomagnets as colloidal mediators for magnetic hyperthermia. *J. Am. Chem. Soc.*, 129(9):2628–2635, March 2007.

[15] R Hergt, S Dutz, R Müller, and M Zeisberger. Magnetic particle hyperthermia: nanoparticle magnetism and materials development for cancer therapy. *J. Phys. Condens. Matter*, 18(38):S2919, September 2006.

[16] A E Deatsch and B A Evans. Heating efficiency in magnetic nanoparticle hyperthermia. *J. Magn. Magn. Mater.*, 354:163–172, March 2014.

[17] M Sagawa, S Fujimura, N Togawa, H Yamamoto, and Y Matsuura. New material for permanent magnets on a base of Nd and Fe (invited). *Journal of Applied Physics*, 55(6):2083–2087, 1984.

[18] S Hirosawa, Y Matsuura, H Yamamoto, S Fujimura, M Sagawa, and H Yamauchi. Magnetization and magnetic anisotropy of $R_2Fe_{14}B$ measured on single crystals. *J. Appl. Phys.*, 59(3):873–879, February 1986.

[19] G C Hadjipanayis, R C Hazelton, and K R Lawless. Cobalt-free permanent magnet materials based on iron-rare-earth alloys. *J. Appl. Phys.*, 55(6):2073–2077, 1984.

[20] N C Koon and B N Das. Crystallization of FeB alloys with rare earths to produce hard magnetic materials (invited). *J. Appl. Phys.*, 55(6):2063–2066, March 1984.

[21] I R Harris and G W Jewell. Rare-earth magnets: properties, processing and applications. In John A Kilner, Stephen J Skinner, Stuart J C Irvine, and Peter P Edwards, editors, *Functional Materials for Sustainable Energy Applications*, chapter 19, pages 600–639. Woodhead Publishing, January 2012.

[22] J F Herbst. $R_2Fe_{14}B$ materials: Intrinsic properties and technological aspects. *Rev. Mod. Phys.*, 63(4):819, 1991.

[23] M Sagawa, S Fujimura, H Yamamoto, Y Matsuura, and K Hiraga. Permanent magnet materials based on the rare earth-iron-boron tetragonal compounds. *IEEE Trans. Magn.*, 20(5):1584–1589, 1984.

[24] J J Croat, J F Herbst, R W Lee, and F E Pinkerton. Pr-Fe and Nd-Fe-based materials: A new class of high-performance permanent magnets. *J. Appl. Phys.*, 55(6):2078–2082, 1984.

[25] D Givord, H S Li, and J M Moreau. Magnetic properties and crystal structure of $Nd_2Fe_{14}B$. *Solid State Commun.*, 50(6):497–499, May 1984.

[26] D J Sellmyer, A Ahmed, G Muench, and G Hadjipanayis. Magnetic hardening in rapidly quenched FeâĂŘPr and FeâĂŘNd alloys. *J. Appl. Phys.*, 55(6):2088–2090, March 1984.

[27] O Gutfleisch, M A Willard, E Brück, C H Chen, S G Sankar, and J P Liu. Magnetic materials and devices for the 21st century: Stronger, lighter, and more energy efficient. *Adv. Mater.*, 23(7):821–842, 2011.

[28] R L Stamps, S Breitkreutz, J Å kerman, A V Chumak, Y Otani, Gerrit E W Bauer, J U Thiele, M Bowen, S A Majetich, M Kläui, I L Prejbeanu, B Dieny, N M Dempsey, and B Hillebrands. The 2014 magnetism roadmap. *J. Phys. D Appl. Phys.*, 47(33):333001, 2014.

[29] S A Vargas, G R T Esteves, P M Maçaira, B Q Bastos, F L Cyrino Oliveira, and R C Souza. Wind power generation: A review and a research agenda. *J. Clean. Prod.*, 218:850–870, May 2019.

[30] S Liu, A Higgins, E Shin, S Bauser, C Chen, D Lee, Y Shen, Y He, and M Q Huang. Enhancing magnetic properties of bulk anisotropic NdFeB-Fe composite magnets by applying powder coating technologies. *IEEE Trans. Magn.*, 42(10):2912–2914, October 2006.

[31] E F Kneller and R Hawig. The exchange-spring magnet: a new material principle for permanent magnets. *IEEE Trans. Magn.*, 27(4):3588–3560, July 1991.

[32] Y P Wang, Y Li, C B Rong, and J Ping Liu. Sm–Co hard magnetic nanoparticles prepared by surfactant-assisted ball milling. *Nanotechnology*, 18(46):465701, October 2007.

[33] C B Rong, Y Zhang, N Poudyal, X Y Xiong, M J Kramer, and J Ping Liu. Fabrication of bulk nanocomposite magnets via severe plastic deformation and warm compaction. *Appl. Phys. Lett.*, 96(10):102513, March 2010.

[34] G Hrkac, T G Woodcock, C Freeman, A Goncharov, J Dean, T Schrefl, and O Gutfleisch. The role of local anisotropy profiles at grain boundaries on the coercivity of $Nd_2Fe_{14}B$ magnets. *Appl. Phys. Lett.*, 97(23):98–101, 2010.

[35] W F Brown. Virtues and weaknesses of the domain concept. *Rev. Mod. Phys.*, 17(1):15–19, January 1945.

[36] Y Hirayama, T Miyake, and K Hono. Rare-earth lean hard magnet compound $NdFe_{12}N$. *JOM*, pages 1–6, 2015.

[37] Y Hirayama, Y K Takahashi, S Hirosawa, and K Hono. $NdFe_{12}N_x$ hard-magnetic compound with high magnetization and anisotropy field. *Scr. Mater.*, 95:70–72, 2015.

[38] C J Cramer. *Essentials of Computational Chemistry: Theories and Models*. Wiley, April 2002.

[39] K Capelle. A bird's-eye view of density-functional theory. *Braz. J. Phys.*, 36:1318–1343, December 2006.

[40] K Lejaeghere, G Bihlmayer, T Björkman, P Blaha, S Blügel, V Blum, D Caliste, I E Castelli, S J Clark, A Dal Corso, S de Gironcoli, T Deutsch, J K Dewhurst, I Di Marco, C Draxl, M Dułak, O Eriksson, J A Flores-Livas, K F Garrity, L Genovese, P Giannozzi, M Giantomassi, S Goedecker, X Gonze, O Grånäs, E K U Gross, A Gulans, F Gygi, D R Hamann, P J Hasnip, N A W Holzwarth, D Iuşan, D B Jochym, F Jollet, D Jones, G Kresse, K Koepernik, E Küçükbenli, Y O Kvashnin, I L M Locht, S Lubeck, M Marsman, N Marzari, U Nitzsche, L Nordström, T Ozaki, L Paulatto, C J Pickard, w Poelmans, M I J Probert, K Refson, M Richter, G Rignanese, S Saha, M Scheffler, M Schlipf, K Schwarz, S Sharma, F Tavazza, P Thunström, A Tkatchenko, M Torrent, D Vanderbilt, M J van Setten, V Van Speybroeck, J M Wills, J R Yates, G X Zhang, and S Cottenier. Reproducibility in density functional theory calculations of solids. *Science*, 351(6280):aad3000, March 2016.

[41] P Hohenberg and W Kohn. Inhomogeneous electron gas. *Phys. Rev.*, 136(3B):B864–B871, November 1964.

[42] J Simoni, M Stamenova, and S Sanvito. Ultrafast demagnetizing fields from first principles. *Phys. Rev. B Condens. Matter*, 95(2):024412, January 2017.

[43] A Lunghi, F Totti, R Sessoli, and S Sanvito. The role of anharmonic phonons in under-barrier spin relaxation of single molecule magnets. *Nat. Commun.*, 8:14620, March 2017.

[44] L Escalera-Moreno, N Suaud, A Gaita-Ariño, and E Coronado. Determining key local vibrations in the relaxation of molecular spin qubits and single-molecule magnets. *J. Phys. Chem. Lett.*, 8(7):1695–1700, April 2017.

[45] S C Westmoreland, R F L Evans, G Hrkac, T Schrefl, G T Zimanyi, M Winklhofer, N Sakuma, M Yano, A Kato, T Shoji, A Manabe, M Ito, and R W Chantrell. Multiscale model approaches to the design of advanced permanent magnets. *Scr. Mater.*, 148:56–62, April 2018.

[46] T Miyake, K Terakura, Y Harashima, H Kino, and S Ishibashi. First-principles study of magnetocrystalline anisotropy and magnetization in $NdFe_{12}$, $NdFe_{11}Ti$, and $NdFe_{11}TiN$. *J. Phys. Soc. Jpn.*, 83(4):043702, March 2014.

[47] W F Brown. Thermal fluctuations of a single-domain particle. *Phys. Rev.*, 130(5):1677–1686, June 1963.

[48] R F L Evans, W J Fan, P Chureemart, T A Ostler, M O A Ellis, R W Chantrell, and Chureemart P. Atomistic spin model simulations of magnetic nanomaterials. *J. Phys. Condens. Matter*, 26(10):103202, 2014.

[49] J Fidler and T Schrefl. Micromagnetic modelling—the current state of the art. *J. Ph ys. D: Appl. Phys.*, 33:R135–R156, 2000.

[50] M Kruzík and A Prohl. Recent developments in the modeling, analysis, and numerics of ferromagnetism. *SIAM Rev.*, 48(3):439–483, January 2006.

[51] S Bance, H Oezelt, T Schrefl, M Winklhofer, G Hrkac, G Zimanyi, O Gutfleisch, R F L Evans, R W Chantrell, T Shoji, M Yano, N Sakuma, A Kato, and A Manabe. High energy product in battenberg structured magnets. *Appl. Phys. Lett.*, 105(19):192401, November 2014.

[52] R F L Evans. Atomistic spin dynamics. In Wanda Andreoni and Sidney Yip, editors, *Handbook of Materials Modeling: Applications: Current and Emerging Materials*, pages 1–23. Springer International Publishing, Cham, 2018.

[53] V V Dobrovitski, M I Katsnelson, and B N Harmon. Mechanisms of decoherence in weakly anisotropic molecular magnets. *Phys. Rev. Lett.*, 84(15):3458–3461, April 2000.

[54] G Grinstein and R H Koch. Coarse graining in micromagnetics. *Phys. Rev. Lett.*, 90(20):207201, May 2003.

[55] D C Jiles. *Introduction to Magnetism and Magnetic Materials*. Springer, 1990.

[56] T Moriya and Y Takahashi. Itinerant electron magnetism. *Annu. Rev. Mater. Sci.*, 14(1):1–25, August 1984.

[57] K Schwarz, P Mohnt, P Blahat, and J Kiibler S. Electronic and magnetic structure of BCC Fe-Co alloys from band theory. *J. Phys. F: Met. Phys.*, 14:2659–2671, 1984.

[58] O N Mryasov, U Nowak, K Y Guslienko, and R W Chantrell. Temperature-dependent magnetic properties of FePt: Effective spin hamiltonian model. *EPL*, 69(5):805, 2005.

[59] J Barker and R W Chantrell. Higher-order exchange interactions leading to metamagnetism in FeRh. *Phys. Rev. B Condens. Matter*, 92(9):094402, September 2015.

[60] L Szunyogh, B Lazarovits, L Udvardi, J Jackson, and U Nowak. Giant magnetic anisotropy of the bulk antiferromagnets IrMn and $IrMn_3$ from first principles. *Phys. Rev. B Condens. Matter*, 79(2):020403, January 2009.

[61] E Ising. Beitrag zur theorie des ferromagnetismus. *Zeitschrift für Physik*, 31(1):253–258, February 1925.

[62] R E Watson, M Blume, and G H Vineyard. Spin motions in a classical ferromagnet. *Physical Review*, 181(2):811, 1969.

[63] R H Kodama and A E Berkowitz. Atomic-scale magnetic modeling of oxide nanoparticles. *Phys. Rev. B: Condens. Matter Mater. Phys.*, 59(9):6321, 1999.

[64] E D Boerner, O Chubykalo-Fesenko, O N Mryasov, R W Chantrell, and O Heinonen. Moving toward an atomistic reader model. *IEEE Trans. Magn.*, 41(2):936–940, February 2005.

[65] P Langevin. Sur la théorie du mouvement brownien. *Compt. Rendus*, 146:530–533, 1908.

[66] R J D Tilley. *Understanding Solids: The Science of Materials*. John Wiley & Sons, September 2005.

[67] B N Figgis and J Lewis. The magnetic properties of transition metal complexes: Cotton/Progress. In F Albert Cotton, editor, *Progress in Inorganic Chemistry*, volume 13 of *Progress in Inorganic Chemistry*, pages 37–239. John Wiley & Sons, Inc., Hoboken, NJ, USA, January 1964.

[68] R M White. *Quantum Theory of Magnetism: Magnetic Properties of Materials*. Springer, Berlin, Heidelberg, 2007.

[69] Allan H Morrish. *The Physical Principles of Magnetism*. Wiley-IEEE Press, 2001.

[70] S Blundell. *Magnetism in Condensed Matter (Oxford Master Series in Physics)*. Oxford University Press, U.S.A., new ed edition edition, November 2000.

[71] W Heitler and F London. Wechselwirkung neutraler atome und homöopolare bindung nach der quantenmechanik. *Z. Physik*, 44(6-7):455–472, June 1927.

[72] O Eriksson, A Bergman, L Bergqvist, and J Hellsvik. *Atomistic Spin Dynamics: Foundations and Applications*. Oxford University Press, Oxford, 2017.

[73] Lev D Landau and E Lifshitz. On the theory of the dispersion of magnetic permeability in ferromagnetic bodies. *Phys. Z. Sowjetunion*, 8(153):101–114, 1935.

[74] T L Gilbert. A lagrangian formulation of the gyromagnetic equation of the magnetization field. *Phys. Rev.*, 100:1243, 1955.

[75] C Gardiner. *Stochastic methods*, volume 4. Springer Berlin, 2009.

[76] Y Z Wang, G C Hadjipanayis, Z X Tang, W B Yelon, V Papaefthymiou, A Moukarika, and D J Sellmyer. Crystallographic and magnetic properties of $NdFe_{10}Mo_2N_{0.5}$. *J. Magn. Magn. Mater.*, 119(1):41–48, February 1993.

[77] S D Oberdick, A Abdelgawad, C Moya, S Mesbahi-Vasey, D Kepaptsoglou, V K Lazarov, R F L Evans, D Meilak, E Skoropata, J van Lierop, I Hunt-Isaak, H J Pan, Y Ijiri, K L Krycka, J A Borchers, and S A Majetich. Spin canting across core/shell $Fe_3O_4/Mn_xFe_{3-x}O_4$ nanoparticles. *Sci. Rep.*, 8(1):3425, February 2018.

[78] O Moze, L Pareti, M Solzi, and W I F David. Neutron diffraction and magnetic anisotropy study of Y-Fe-Ti intermetallic compounds. *Solid State Commun.*, 66(5):465–469, May 1988.

[79] R W James and William Lawrence Bragg. *The optical principles of the diffraction of x-rays*. G. Bell & Sons, London, 1962.

[80] H Sun, T Tomida, and S Hirosawa. Magnetic properties and microstructure studies of Sm–Fe magnetic thin films. *J. Appl. Phys.*, 81(1):328–334, January 1997.

[81] S A Nikitin, I S Tereshina, V N Verbetskii, and A A Salamova. Magnetic anisotropy of $YFe_{11}Ti$ and its hydride. *Phys. Solid State*, 40(2):258–262, February 1998.

[82] H T Kim, Y B Kim, C S Kim, and H Jin. Magnetocrystalline anisotropy of $(Sm_{0.5}RE_{0.5})Fe_{11}Ti$ compounds (RE: Ce, Pr, Nd, Sm, Gd and Tb). *J. Magn. Magn. Mater.*, 152(3):387–390, January 1996.

[83] S Foner. Versatile and sensitive vibratingâĂŘsample magnetometer. *Rev. Sci. Instrum.*, 30(7):548–557, July 1959.

[84] L H Lewis, D O Welch, and V Panchanathan. Curie temperature enhancement of $Nd_2Fe_{14}B$ in nanocomposite exchange-spring alloys. *Journal of magnetism and magnetic materials*, 175(3):275–278, 1997.

[85] M d'Aquino, C Serpico, G Coppola, I D Mayergoyz, and G Bertotti. Midpoint numerical technique for stochastic Landau-Lifshitz-Gilbert dynamics. *J. Appl. Phys.*, 99(8):08B905, 2006.

[86] J H Mentink, M V Tretyakov, A Fasolino, M I Katsnelson, and Th Rasing. Stable and fast semi-implicit integration of the stochastic Landau–Lifshitz equation. *J. Phys. Condens. Matter*, 22(17):176001, April 2010.

[87] A Greiner, W Strittmatter, and J Honerkamp. Numerical integration of stochastic differential equations. *J. Stat. Phys.*, 51(1):95–108, April 1988.

[88] J García-Palacios and F J Lázaro. Langevin-dynamics study of the dynamical properties of small magnetic particles. *Phys. Rev. B Condens. Matter*, 58(22):14937–14958, December 1998.

[89] P E Kloeden and E Platen. *Numerical Solution of Stochastic Differential Equations*. Springer Science & Business Media, April 2013.

[90] N Metropolis, A W Rosenbluth, M N Rosenbluth, A H Teller, and E Teller. Equation of state calculations by fast computing machines. *J. Chem. Phys.*, 21(6):1087–1092, 1953.

[91] K Binder. Applications of monte carlo methods to statistical physics. *Rep. Prog. Phys.*, 60(5):487, 1997.

[92] D Hinzke and U Nowak. Monte Carlo simulation of magnetization switching in a Heisenberg model for small ferromagnetic particles. *Comput. Phys. Commun.*, 121:334–337, 1999.

[93] G Hrkac, K Butler, T G Woodcock, L Saharan, T Schrefl, and O Gutfleisch. Modeling of Nd-Oxide grain boundary phases in Nd-Fe-B sintered magnets. *JOM*, 66(7):1138–1143, July 2014.

[94] L Néel, R Chastel, C Besset, J Horowitz, A Messiah, J Winter, G Paquette, M Bayet, M Hoyaux, R Bernas, and Others. Magnetic surface anisotropy and superlattice formation by orientation. anisotropie magnétique superficielle et surstructures d'orientation p. 225. *J. Phys. Radium*, 15(4), 1954.

[95] D A Garanin and H Kachkachi. Surface contribution to the anisotropy of magnetic nanoparticles. *Phys. Rev. Lett.*, 90(6):065504, 2003.

[96] P Bruno. Magnetic surface anisotropy of cobalt and surface roughness effects within Néel's model. *J. Phys. F: Met. Phys.*, 18(6):1291, 1988.

[97] P Asselin, R F L Evans, J Barker, R W Chantrell, R Yanes, O Chubykalo-Fesenko, D Hinzke, and U Nowak. Constrained monte carlo method and calculation of the temperature dependence of magnetic anisotropy. *Phys. Rev. B: Condens. Matter Mater. Phys.*, 82(5):054415, August 2010.

[98] E E Fullerton, J S Jiang, and S D Bader. Hard/soft magnetic heterostructures: model exchange-spring magnets. *J. Magn. Magn. Mater.*, 200(1–3):392–404, October 1999.

[99] R Skomski. Nanomagnetics. *Journal of Physics: Condensed Matter*, 15(20):R841, 2003.

[100] E F Kneller and R Hawig. The exchange-spring magnet: a new material principle for permanent magnets. *IEEE Trans. Magn.*, 27(4):3588–3560, July 1991.

[101] R Skomski and J M Coey. Giant energy product in nanostructured two-phase magnets. *Phys. Rev. B Condens. Matter*, 48(21):15812–15816, 1 December 1993.

[102] J E Davies, O Hellwig, E E Fullerton, J S Jiang, S D Bader, G T Zimányi, and K Liu. Anisotropy dependence of irreversible switching in Fe/SmCo and FeNi/FePt exchange spring magnet films. *Appl. Phys. Lett.*, 86(26):262503, June 2005.

[103] S A Majetich and M Sachan. Magnetostatic interactions in magnetic nanoparticle assemblies: energy, time and length scales. *J. Phys. D Appl. Phys.*, 39(21):R407, October 2006.

[104] X Batlle and A Labarta. Finite-size effects in fine particles: magnetic and transport properties. *J. Phys. D Appl. Phys.*, 35:R15, 2002.

[105] N A Frey, S Peng, K Cheng, and S Sun. Magnetic nanoparticles: synthesis, functionalization, and applications in bioimaging and magnetic energy storage. *Chem. Soc. Rev.*, 38(9):2532–2542, September 2009.

[106] S Laurent, D Forge, M Port, A Roch, C Robic, L Vander Elst, and R N Muller. Magnetic iron oxide nanoparticles: synthesis, stabilization, vectorization, physicochemical characterizations, and biological applications. *Chem. Rev.*, 108(6):2064–2110, June 2008.

[107] A López-Ortega, A Estrader, G Salazar-Alvarez, A G Roca, and J Nogués. Applications of exchange coupled bi-magnetic hard/soft and soft/hard magnetic core/shell nanoparticles. *Physics Reports*, 2014.

[108] T Schrefl, J Fidler, and H Kronmüller. Remanence and coercivity in isotropic nanocrystalline permanent magnets. *Phys. Rev. B Condens. Matter*, 49(9):6100–6110, 1 March 1994.

[109] J Kuma, N Kitajima, Y Kanai, and H Fukunaga. Maximum energy product of isotropic Nd-Fe-B-based nanocomposite magnets. *J. Appl. Phys.*, 83(11):6623–6625, 1 June 1998.

[110] H Fukunaga and H Nakamura. Computer simulation of magnetic properties of anisotropic nanocomposite magnets. *IEEE Trans. Magn.*, 36(5):3285–3287, September 2000.

[111] H Fukunaga, R Horikawa, M Nakano, T Yanai, T Fukuzaki, and K Abe. Computer simulations of the magnetic properties of nanocomposite magnets with a Core-Shell structure. *IEEE Trans. Magn.*, 49(7):3240–3243, July 2013.

[112] R F L Evans, U Atxitia, and R W Chantrell. Quantitative simulation of temperature-dependent magnetization dynamics and equilibrium properties of elemental ferromagnets. *Phys. Rev. B Condens. Matter*, 91(14):144425, 30 April 2015.

[113] P Weiss and R Forrer. Aimantation et phénomène magnétocalorique du nickel. *Ann. Phys.*, 10(5):153–213, 1926.

[114] D J Griffiths. *Introduction to electrodynamics*, volume 3. Prentice Hall Upper Saddle River, NJ, 1999.

[115] J F Herbst, J J Croat, F E Pinkerton, and W B Yelon. Relationships between crystal structure and magnetic properties in $Nd_2Fe_{14}B$. *Phys. Rev. B: Condens. Matter Mater. Phys.*, 29(7):4176, 1984.

[116] C B Shoemaker, D P Shoemaker, and R Fruchart. The structure of a new magnetic phase related to the sigma phase: iron neodymium boride $Nd_2Fe_{14}B$. *Acta Crystallogr. C*, 40(10):1665–1668, October 1984.

[117] R W G Wyckoff. *The Analytical Expression of the Results of the Theory of Space-groups*. Carnegie institution of Washington, 1922.

[118] M I Aroyo, J M Perez-Mato, C Capillas, E Kroumova, S Ivantchev, G Madariaga, A Kirov, and H Wondratschek. Bilbao crystallographic server: I. databases and crystallographic computing programs. *Zeitschrift für Kristallographie - Crystalline Materials*, 221(1):243, January 2006.

[119] M I Aroyo, A Kirov, C Capillas, J M Perez-Mato, and H Wondratschek. Bilbao crystallographic server. II. representations of crystallographic point groups and space groups. *Acta Crystallogr. A*, 62(Pt 2):115–128, March 2006.

[120] M I Aroyo, J M Perez-Mato, D Orobengoa, E Tasci, G De La Flor, and A Kirov. Crystallography online: Bilbao crystallographic server. *Bulg. Chem. Commun.*, 43(2):183–197, 2011.

[121] K Tokuhara, Y Ohtsu, F Ono, O Yamada, M Sagawa, and Y Matsuura. Magnetization and torque measurements on $Nd_2Fe_{14}B$ single crystals. *Solid State Commun.*, 56(4):333–336, October 1985.

[122] M Pajda, J Kudrnovský, I Turek, V Drchal, and P Bruno. *Ab initio* calculations of exchange interactions, spin-wave stiffness constants, and Curie temperatures of Fe, Co, and Ni. *Phys. Rev. B Condens. Matter*, 64(17):174402, October 2001.

[123] I A Campbell. Indirect exchange for rare earths in metals. *J. Phys. F: Met. Phys.*, 2(3):L47, 1972.

[124] K H J Buschow. Intermetallic compounds of rare-earth and 3d transition metals. *Rep. Prog. Phys.*, 40(10):1179, 1977.

[125] K H J Buschow. Rare earth compounds. In *Handbook of Ferromagnetic Materials*, volume 1, chapter 4, pages 297–414. Elsevier, January 1980.

[126] J M Cadogan, J P Gavigan, D Givord, and Hong-Shuo Li. A new approach to the analysis of magnetisation measurements in rare-earth/transition-metal compounds: application to $Nd_2Fe_{14}B$. *J. Phys. F: Met. Phys.*, 18(4):779, 1988.

[127] H B Callen and E Callen. The present status of the temperature dependence of magnetocrystalline anisotropy, and the l(l+1)/2 power law. *J. Phys. Chem. Solids*, 27(8):1271–1285, August 1966.

[128] R F L Evans, R Cuadrado, M I J Probert, T Shoji, M Yano, A Manabe, D Givord, G Hrkac, T Schrefl and R W Chantrell. Atomistic calculation of temperature dependent properties of $Nd_2Fe_{14}B$. Unpublished manuscript, 2015.

[129] F T Parker. Analysis of crystal field and exchange interactions in $Nd_2Fe_{14}B$. *J. Appl. Phys.*, 61(7):2606–2609, April 1987.

[130] E C Stoner and E P Wohlfarth. A mechanism of magnetic hysteresis in heterogeneous alloys. *Philos. Trans. R. Soc. Lond. A*, 240(826):599–642, May 1948.

[131] M Sagawa, S Fujimura, H Yamamoto, Y Matsuura, and S Hirosawa. Magnetic properties of rareâĂŘearthâĂŘironâĂŘboron permanent magnet materials. *J. Appl. Phys.*, 57(8):4094–4096, April 1985.

[132] M Sagawa, S Hirosawa, H Yamamoto, S Fujimura, and Y Matsuura. Nd–Fe–B permanent magnet materials. *Jpn. J. Appl. Phys.*, 26(6):785, March 1987.

[133] D B De Mooij and K H J Buschow. Some novel ternary $ThMn_{12}$-type compounds. *Journal of the Less Common Metals*, 136(2):207–215, January 1988.

[134] K Ohashi, Y Tawara, R Osugi, and M Shimao. Magnetic properties of FeâĂŘrich rareâĂŘearth intermetallic compounds with a $ThMn_{12}$ structure. *J. Appl. Phys.*, 64(10):5714–5716, November 1988.

[135] K H J Buschow and D B De Mooij. Novel ternary Fe-rich rare earth intermetallics. In I V Mitchell, J M D Coey, D Givord, I R Harris, and R Hanitsch, editors, *Concerted European Action on Magnets (CEAM)*, pages 63–75. Springer Netherlands, Dordrecht, 1989.

[136] B P Hu, H S Li, J P Gavigan, and J M D Coey. Intrinsic magnetic properties of the iron-rich $ThMn_{12}$-structure alloys $RFe_{11}Ti$; R=Y, Nd, Sm, Gd, Tb, Dy, Ho, Er, Tm and Lu. *J. Phys. Condens. Matter*, 1(4):755, January 1989.

[137] T S Chin, W C Chang, H C Ku, C C Weng, H T Lee, and M P Hung. Structure and magnetic properties of the $ThMn_{12}$-type NdFeM alloys (M=Si/Al/B/transition metals). *IEEE Trans. Magn.*, 25(5):3300–3302, 1989.

[138] S Chikazumi and C D Graham. *Physics of Ferromagnetism*. OUP Oxford, 2 edition, April 2009.

[139] K W H Stevens. Matrix elements and operator equivalents connected with the magnetic properties of rare earth ions. *Proceedings of the Physical Society. Section A*, 65(3):209–215, 1952.

[140] J Deportes, D Givord, J Schweizer, and F Tasset. Different contributions of the two cobalt sites to the magnetocrystalline anisotropy of YCo 5 and related compounds. *IEEE Trans. Magn.*, 12(6):1000–1002, 1976.

[141] E P Wohlfarth and K H J Buschow. *Ferromagnetic materials: a handbook on the properties of magnetically ordered substances*. North-Holland Pub. Co., 2008.

[142] H S Li and B P Hu. Determination of the second order anisotropy constant K_1 from the magnetization curves of polycrystalline samples: application to Y-Fe rich compounds. *Le Journal de Physique Colloques*, 49(C8):C8–513, 1988.

[143] M Kirschner, T Schrefl, F Dorfbauer, G Hrkac, D Suess, and J Fidler. Cell size corrections for nonzero-temperature micromagnetics. *J. Appl. Phys.*, 97(10):2004–2006, 2005.

[144] J Fischbacher, A Kovacs, L Exl, J Kühnel, E Mehofer, H Sepehri-Amin, T Ohkubo, K Hono, and T Schrefl. Searching the weakest link: Demagnetizing fields and magnetization reversal in permanent magnets. *Scr. Mater.*, November 2017.

[145] T G Woodcock, Y Zhang, G Hrkac, G Ciuta, N M Dempsey, T Schrefl, O Gutfleisch, and D Givord. Understanding the microstructure and coercivity of high performance NdFeB-based magnets. *Scr. Mater.*, 67(6):536–541, 2012.

[146] L Li, D E Luzzi, and C D Graham. HighâĂŘresolution transmission electron microscopy observations on textured rapidly quenched NdFeB permanent magnets. *J. Appl. Phys.*, 70(10):6459–6461, November 1991.

[147] J D Livingston. Magnetic domains in sintered FeâĂŘNdâĂŘB magnets. *J. Appl. Phys.*, 57(8):4137–4139, April 1985.

[148] Y Otani, H Miyajima, and S Chikazumi. Large barkhausen jumps observed in Nd-Fe-B sintered magnets at very low temperatures. *IEEE Trans. Magn.*, 25(5):3431–3433, 1989.

[149] E E Fullerton, C H Sowers, J P Pearson, X Z Wu, D Lederman, and S D Bader. Structure and magnetism of epitaxial Rare-Earth-Transition-Metal films. In George C Hadjipanayis, editor, *Magnetic Hysteresis in Novel Magnetic Materials*, pages 467–478. Springer Netherlands, Dordrecht, 1997.

[150] H Hegde, R Rani, A Navarathna, K Chen, and F J Cadieu. Film synthesis and magnetic properties of $ThMn_{12}$âĂŘtype $Sm(Fe_{1-x}T_x)_{12}$, x≤0.12. *J. Appl. Phys.*, 70(10):6345–6347, November 1991.

[151] D Wang, S H Liou, P He, D J Sellmyer, G C Hadjipanayis, and Y Zhang. $SmFe_{12}$ and $SmFe_{12}N_x$ films fabricated by sputtering. *J. Magn. Magn. Mater.*, 124(1):62–68, June 1993.

[152] N Sakuma, S Suzuki, T Kuno, K Urushibata, K Kobayashi, M Yano, A Kato, and A Manabe. Influence of Zr substitution on the stabilization of $ThMn_{12}$-type $(Nd_{1-\alpha}Zr_{\alpha})(Fe_{0.75}Co_{0.25})_{11.25}Ti_{0.75}N_{1.2-1.4}$ (α = 0-0.3) compounds. *AIP Adv.*, 6(5):056023, May 2016.

[153] S Suzuki, T Kuno, K Urushibata, K Kobayashi, N Sakuma, K Washio, H Kishimoto, A Kato, and A Manabe. A (Nd, Zr)(Fe, Co)$_{11.5}$Ti$_{0.5}$N$_x$ compound as a permanent magnet material. *AIP Adv.*, 4(11):117131, 2014.

[154] S Suzuki, T Kuno, K Urushibata, K Kobayashi, N Sakuma, K Washio, M Yano, A Kato, and A Manabe. A new magnet material with $ThMn_{12}$ structure: $(Nd_{1-x}Zr_x)(Fe_{1-y}Co_y)_{11+z}Ti_{1-z}N_{\alpha}$ (α=0.6–1.3). *J. Magn. Magn. Mater.*, 401:259–268, March 2016.

[155] T Kuno, S Suzuki, K Urushibata, K Kobayashi, N Sakuma, M Yano, A Kato, and A Manabe. (Sm, Zr)(Fe, Co)$_{11.0-11.5}$Ti$_{1.0-0.5}$ compounds as new permanent magnet materials. *AIP Adv.*, 6(2):025221, 2016.

[156] J C Slater. Atomic radii in crystals. *J. Acoust. Soc. Am.*, 36:2346, 2005.

[157] S Sakurada, A Tsutai, and M Sahashi. A study on the formation of $ThMn_{12}$ and $NaZn_{13}$ structures in $RFe_{10}Si_2$. *J. Alloys Compd.*, 187(1):67–71, August 1992.

[158] R Moreno, R F L Evans, S Khmelevskyi, M C Muñoz, R W Chantrell, and O Chubykalo-Fesenko. Temperature-dependent exchange stiffness and domain wall width in Co. *Phys. Rev. B Condens. Matter*, 94(10):104433, September 2016.